Formation of retinal direction-selective circuitry initiated by starburst amacrine cell homotypic contact

Thomas A. Ray[1,2], Suva Roy[1], Christopher Kozlowski[1,2], Jingjing Wang[1,2], Jon Cafaro[1], Samuel W. Hulbert[1], Christopher V. Wright[3], Greg D. Field[1], and Jeremy N. Kay[1,2]

1) Department of Neurobiology; 2) Department of Ophthalmology, Duke University School of Medicine, Durham, NC 27710 USA

3) Department of Cell and Developmental Biology, Vanderbilt University School of Medicine, Nashville, TN 37232 USA

Correspondence to: Jeremy Kay (jeremy.kay@duke.edu)

Keywords: Neural development; retinal ganglion cell; bipolar cell; mouse; radial migration; Ptf1a; IPL.

Impact statement: Selective synapse formation in a retinal motion-sensitive circuit is orchestrated by starburst amacrine cells, which use homotypic interactions to initiate formation of a dendritic scaffold that recruits projections from circuit partners.

SUMMARY

A common strategy by which developing neurons locate their synaptic partners is through projections to circuit-specific neuropil sublayers. Once established, sublayers serve as a substrate for selective synapse formation, but how sublayers arise during neurodevelopment remains unknown. Here we identify the earliest events that initiate formation of the direction-selective circuit in the inner plexiform layer of mouse retina. We demonstrate that radially-migrating newborn starburst amacrine cells establish homotypic contacts on arrival at the inner retina. These contacts, mediated by the cell-surface protein MEGF10, trigger neuropil innervation resulting in generation of two sublayers comprising starburst-cell dendrites. This dendritic scaffold then recruits projections from circuit partners. Abolishing MEGF10-mediated contacts profoundly delays and ultimately disrupts sublayer formation, leading to broader direction tuning and weaker direction-selectivity in retinal ganglion cells. Our findings reveal a mechanism by which differentiating neurons transition from migratory to mature morphology, and highlight this mechanism's importance in forming circuit-specific sublayers.

INTRODUCTION

In the developing nervous system, neurons form selective synapses to generate circuits comprised of cell-type-specific connections. This selectivity is important for circuit function because it ensures connectivity between neurons specialized for particular information-processing tasks. Despite its importance, basic questions about selective synapse formation remain unanswered. For example, we do not know how cell types fated to form synapses coordinate their growth to establish contact with each other. This is a significant cell biological challenge, because the neurons that comprise a single circuit are often born at disparate times and physical locations.

In many tissues, notably the insect and vertebrate visual systems, synaptic specificity is facilitated by laminar specificity, the phenomenon whereby circuit partners project their axons and dendrites to narrow strata within a laminated neuropil (Sanes and Zipursky, 2010). The inner plexiform layer (IPL) of the vertebrate retina comprises at least 10 distinct sublayers built from the axons and dendrites of different amacrine, bipolar, and retinal ganglion cell (RGC) types (Baier, 2013). By projecting to the same IPL sublayer, circuit partners can be assured of encountering each other. The developmental events that create sublayers and guide circuit partners to converge upon them are therefore essential for establishment of retinal circuitry. At later developmental stages, when rudimentary IPL sublayers have already formed, neurons rely on molecular cues localized to those sublayers for guidance to the appropriate IPL strata (Duan et al., 2014; Matsuoka et al., 2011; Sun et al., 2013; Yamagata and Sanes, 2008; Visser et al., 2015). However, a crucial question remains unresolved: How do sublayers form in the first place? Understanding the mechanisms that initiate creation of sublayers will provide significant insight into the earliest step in circuit formation.

To learn how members of a single circuit create layers and converge upon them to achieve synapse specificity, we studied the direction-selective (DS) circuit of mouse retina (Fig. 1A). This circuit reports the direction of image motion to the brain through the spiking activity of distinct DS ganglion cell (DSGC) types that are tuned to prefer stimuli moving in particular directions (Demb, 2007; Vaney et al., 2012). The DS circuit comprises a limited number of well-described cell types amenable to genetic marking and manipulation (Kay et al., 2011; Huberman et al., 2009; Duan et al., 2014): In addition to DSGCs, circuit members include GABAergic/cholinergic interneurons called starburst amacrine cells (SACs); and four subtypes of glutamatergic bipolar cells (Chen et al., 2014; Duan et al., 2014; Greene et al., 2016; Kim et al., 2014). The circuit occupies two IPL sublayers, ON and OFF, named for the light response profiles of the neurons that project to them. ON-OFF DSGCs (ooDSGCs) send dendrites to both sublayers, while SACs and bipolar cells project to one or the other, depending on their subtype (Fig. 1A). Several molecular perturbations have been described that influence ON vs. OFF laminar targeting in the mouse DS circuit (Sun et al., 2013; Duan et al., 2014), but in these cases IPL sublayers still form in the right place; errors are limited to choosing the wrong DS sublayer. Thus, neither the establishment of the DS circuit sublayers nor their positioning in the appropriate IPL region depends on molecules that have been studied to date.

Here we seek to understand the earliest events leading to formation of the DS circuit IPL sublayers. Two lines of evidence suggest that SACs may take the lead in assembling this circuit. First, SACs are among the first cells to stratify the IPL: Even though other neurons innervate it contemporaneously, SACs are precocious in restricting their arbors into sublayers (Stacy and Wong, 2003; Kay and Sanes, 2013). Second, in mutant mice that entirely lack RGCs or bipolar cells, SAC IPL projections are largely normal, indicating SACs can form sublayers in the

absence of their circuit partners (Moshiri et al., 2008; Green et al., 2003). Thus, we set out to test the hypothesis that SACs orchestrate assembly of the DS circuit sublayers. We find evidence supporting this hypothesis, and we identify a surprising cellular mechanism initiating SAC lamination: Rather than immediately innervating the IPL, newborn SACs first produce a transient homotypic arbor network outside the IPL. These early homotypic contacts serve as a cue promoting SAC dendrite development and circuit integration upon conclusion of their radial migration to the inner retina. When deprived of homotypic contacts, SAC IPL innervation – and consequent sublayer formation – is impaired. We identify the SAC cell-surface protein MEGF10 as the molecular mediator of IPL innervation upon homotypic contact. In the absence of MEGF10, SACs persist in growing arbors outside the IPL, delaying IPL innervation. This in turn delays formation of the DS circuit sublayers and leads to SAC sublaminar targeting errors that persist to adulthood. We further show that impaired SAC sublayer formation has consequences for laminar targeting of their circuit partners: While partnering remains intact, lamination is disrupted, leading to spatial inhomogeneity in the DS circuit network. Finally, we show that these MEGF10-dependent anatomical changes both broaden and weaken direction tuning across the population of ooDSGCs. These results demonstrate that SACs orchestrate DS circuit assembly, first by initiating sublayer formation via homotypic contact, and then by using their laminated dendrites as a scaffold that guides projections of their circuit partners.

RESULTS

Timing of DS circuit IPL sublayer formation

To explore how the DS circuit creates its IPL sublayers, we began by determining when the sublayers first emerge in mouse. This analysis focused on SACs and ooDSGCs because

bipolar cells develop later (Morgan et al., 2006). Previous estimates of layer emergence vary widely (Stacy and Wong, 2003; Sun et al., 2013) due to the lack of adequate markers to study dendrite development in neonatal SACs. We therefore assembled a suite of mouse lines and antibody markers for this purpose, enabling anatomical studies of the full SAC population as well as individual cells (Fig. 1B-C; Fig. 1-Supplement 1; Fig. 2-Supplement 1). These markers revealed that SAC dendrites form two continuous well-defined laminae by P1. Some dendrites were stratified already at P0, even though the P0 IPL neuropil is less than one cell diameter wide (Fig. 1B; Fig. 1-Supplement 1). Further supporting this timeline, individual P1 SACs made lamina-specific projections (Fig. 1C): 96% of OFF SACs in the inner nuclear layer (INL), and 99% of ON SACs in the ganglion cell layer (GCL), stratified within the expected IPL sublayer (n = 49/51 OFF; 78/79 ON; 4 mice). By contrast, ooDSGC dendrites were rudimentary and unstratified at P1 (n = 18 cells, 3 mice; Fig. 1-Supplement 1; also see Peng et al., 2017). Even at P2, only 30% of ooDSGCs co-fasciculated with SAC arbors; the rest projected diffusely within the IPL (n = 23 cells, 2 mice; Fig. 1D; Fig. 1-Supplement 1). These results indicate that SACs form IPL sublayers at P0-P1, and are joined later by their synaptic partners.

Early SAC projections target neighboring SAC somata

To gain insight into how SACs form their sublayers, we next investigated the events immediately preceding SAC stratification. At P0-1, other IPL sublayers do not yet exist (Kay and Sanes, 2013; Stacy and Wong, 2003), so SACs are unlikely to innervate their sublayers by following pre-existing cues. Instead, we hypothesized that SACs create their sublayers by engaging in homotypic interactions. To test this idea, we examined embryonic retina to determine if and when SACs first establish homotypic contact. SACs exit the cell cycle at the apical retinal surface and migrate radially through the outer neuroblast layer (ONBL). They next

arrive at the inner neuroblast layer (INBL), where postmitotic neurons reside (Hinds and Hinds, 1978; Fig. 2A,B). Then they begin to innervate the nascent IPL, which begins to appear in some retinal regions at E16 (Fig. 2A). To reveal SAC morphology throughout these steps, we used mice expressing membrane-targeted GFP (mGFP) under control of the *Isl1* gene (Galli-Resta et al., 1997). In these $Isl1^{mG}$ mice, we found that migrating SACs in the E16 ONBL rarely contacted each other (Fig. 2A-C). However, upon arriving at the INBL, SAC arbors contacted the soma or primary dendrite of neighboring SACs (Fig. 2D,E). The majority of INBL SACs projected these soma-directed neurites, such that a GFP^+ arbor network connected them (Fig. 2E,H).

In retinal regions where IPL neuropil had emerged by E16 (Fig. 2A,B), SACs also sent a distinct set of arbors to innervate the IPL (Fig. 2E), raising the question of whether the soma- or IPL-directed projection establishes the first homotypic contact. We concluded that soma-directed SAC contact precedes IPL innervation, for two reasons. First, soma contacts were found in retinal regions where the IPL had not yet emerged (Fig. 2-Supplement 2). Second, soma contacts were observed among cells that still showed migratory morphological features, such as apical and/or basal processes (Deans et al., 2011; Hinds and Hinds, 1978), and did not yet project into the IPL (Fig. 2D; Fig. 2-Supplement 2). Indeed, rather than projecting to the IPL, SACs oriented their primary dendrites towards their neighbors. This was shown by staining for the intermediate filament protein internexin (Knabe et al., 2007), a selective marker of SAC primary dendrites (Fig. 2–Supplement 1). Unlike P1-2 SACs, which exclusively directed primary dendrites towards the IPL, E16 SACs projected in a variety of directions, including within the INBL (Fig. 2F,G; Fig. 2-Supplement 1). In many cases, SACs projected directly towards each other (Fig. 2F). Thus, INBL SACs appear to transiently seek out soma contact before shifting to target the IPL.

Together, these data indicate that SACs first make homotypic contact by projecting arbors toward neighboring SAC somata, and that this contact occurs at, or perhaps just before, completion of their radial migration (Fig. 2N).

To determine how long these soma-directed SAC contacts persist, we examined SAC anatomy at early postnatal ages using *Isl1*^{mG} and *Chat*^{mG} (Fig. 1-Supplement 1) mice. At P0-1, SAC arbors within the soma layers remained remarkably prominent (Fig. 2H). Most OFF SACs assumed a bi-laminar morphology, with one set of arbors in the IPL and another set in the INL (Fig. 2I-K,M; Fig. 2-Supplement 2). As with E16 contacts, the P1 INL arbors selectively contacted somata or arbors of SAC neighbors (Fig. 2J; 89% of branches terminated on a homotypic neighbor; n = 122 arbor tips from 22 cells). By P2-3, however, this dense INL network was mostly gone (Fig. 2H,M; Fig. 2-Supplement 2). ON SACs also made soma layer projections between P0-P3 that selectively contacted neighboring SAC somata (Fig. 2L,M; Fig. 2-Supplement 2). While the GCL SAC network was not as prominent as the INL network, some ON SACs established soma contact without a separate GCL projection; instead, these cells sent fine soma-directed branches from their IPL arbors (Fig. 2-Supplement 2). Together, these observations demonstrate that both ON and OFF SACs make transient soma-directed homotypic contacts that arise prior to IPL dendrite elaboration, and are disassembled at P2-3 after SAC sublayers have formed (Fig. 2N).

Homotypic contact is required for SAC IPL innervation and dendrite lamination

SAC homotypic contacts arise at a time when they could serve as a cue for IPL innervation and sublayer formation. To test this idea, we developed a genetic strategy to prevent SACs from contacting each other in vivo. *Ptf1a* encodes a transcription factor required for progenitor cells to assume an amacrine fate (Fujitani et al., 2006; Nakhai et al., 2007; Fig. 3-

Supplement 1). We crossed conditional *Ptf1a*^{flox} mutant mice (Krah et al., 2015) to a Cre line (*Six3:Cre*; Furuta et al., 2000), that drives widespread recombination in central retina but spares some progenitors from Cre activity in peripheral retina (Fig. 3A; Fig. 3-Supplement 1). In *Six3:Cre; Ptf1a*$^{flox/flox}$ mice (abbreviated *Ptf1a*^{cKO}), only these spared Cre^{-} progenitors were capable of giving rise to SACs, indicating that any SACs produced in these mutants are wild-type at the *Ptf1a* locus (Fig. 3C). Therefore, the *Ptf1a*^{cKO} mutant creates a situation where otherwise-normal SACs are present at significantly lower density than in wild-type retina (Fig. 3B,C). In P1-2 mutants, some SACs were effectively segregated from their neighbors – these were termed "solitary" SACs – while others had neighbors sufficiently nearby that they touched (Fig. 3B,E,F; Fig. 3-Supplement 1).

Comparing solitary to touching SACs in *Ptf1a*^{cKO} retinas revealed a role for homotypic contacts in promoting IPL innervation and sublayer formation. At P1-2, touching SACs projected normally to the IPL, similar to SACs from *Ptf1a*$^{+}$ littermates (Fig. 3D,E,G). This suggests that any changes in retinal cell type composition caused by loss of *Ptf1a* (Fig. 3-Supplement 1) are not by themselves sufficient to perturb SAC sublayer formation. By contrast, solitary SACs largely failed to innervate the IPL (Fig. 3F,G). This was not caused by abnormal migration: Solitary SACs were properly positioned at the IPL border, but sent only rudimentary arbors into it (Fig. 3F; Fig. 3-Supplement 1). Solitary SACs were also more likely to project processes into the soma layers (Fig. 3G), and when they did so, the projections were typically more elaborate than those observed in wild-type retina (Fig. 3D,F; Fig. 3-Supplement 1). Thus, solitary SACs overgrew arbors directed towards neighboring somata instead of growing IPL dendrites. Both types of projection errors were also seen at P15, indicating that early errors persist to retinal maturity (Fig. 3-Supplement 1). Misprojecting SACs were still in contact with numerous other

amacrine cells and their arbors, strongly suggesting that generic amacrine contacts are not sufficient to ensure normal dendrite targeting (Fig. 3-Supplement 1). Instead, homotypic interactions are specifically required for IPL innervation and sublayer formation.

Requirement for MEGF10 in SAC IPL innervation and sublayer formation

To understand how SACs initiate IPL innervation upon homotypic contact, we next sought to identify the molecular cues that SACs use to recognize that contact has occurred. The cell-surface protein MEGF10 (Fig. 4A) is a strong candidate to mediate homotypic recognition in this context, for four reasons. First, it is selectively expressed by SACs during the perinatal period (Fig. 1B; Fig. 1-Supplement 1). Second, the onset of its expression coincides with onset of SAC homotypic contact at the conclusion of radial migration (Fig. 4B; Kay et al., 2012). Third, MEGF10 protein is present on soma-directed SAC arbors, making it available to transduce signals arising on these arbors (Fig. 4C). Finally, MEGF10 mediates SAC-SAC interactions in a separate context – during formation of the orderly "mosaic" among SAC cell bodies across the retina (Kay et al., 2012). Thus, we tested whether MEGF10 also mediates SAC-SAC recognition to initiate IPL innervation. If so, SACs from mice lacking *Megf10* gene function should have phenotypes similar to solitary *Ptf1a*^{cKO} SACs – i.e., reduced IPL innervation and increased arborization in cell body layers.

To test this prediction, we examined SAC anatomy in *Megf10* null mutants (Kay et al., 2012) and littermate controls at P0-1, when sublayers are first forming. We found a striking deficit in sublayer formation – both ON and OFF strata were absent or severely disrupted in mutants (Fig. 5A). This phenotype was not due to aberrant SAC migration, because mutant SACs reached the inner retina in normal numbers (wild-type, 2600 ± 287 SACs/mm^2; mutant, 3153 ± 145 SACs/mm^2; $p = 0.144$, 2-tailed t-test; $n = 3$ each group) and assumed a normal

location adjacent to the IPL at P0 (Fig. 5A). Rather, the absence of SAC sublayers was due to innervation of the soma layers instead of the IPL – a phenotype reminiscent of solitary *Ptf1a*^{cKO} SACs. This phenotype was specific to SACs: Other amacrine cell types showed normal dendritic morphology in *Megf10* mutants (Fig. 5-Supplement 1). The severe disruption to SAC IPL innervation was evident from pan-SAC labeling (Fig. 5A) as well as single cell analysis, which revealed that most *Megf10*$^{-/-}$ SACs made rudimentary, unstratified IPL projections at P0-1 (Fig. 5C,E; n = 1/15 OFF SACs were stratified). Mutant IPL dendrites appeared undifferentiated, with a lack of space-filling branches (Fig. 5C,E). As a result, not only did their arbors enclose a significantly smaller IPL territory, but they also failed to sample as much of their enclosed territory as control SACs (Fig. 5C; also compare to control cell in Fig. 2I). By P3 some ON SAC IPL innervation was evident, but OFF SAC arbors remained largely confined to the soma layer; those that did reach the IPL remained undifferentiated (Fig. 5B,E). These observations indicate that deletion of MEGF10 causes a profound impairment of IPL-directed SAC dendrite growth, preventing timely sublayer formation.

Instead of innervating the IPL, *Megf10* mutant SACs ramified exuberantly in the soma layers. Both ON and OFF SACs were affected (Fig. 5-Supplement 1), but the OFF SAC phenotype was particularly striking: Between P0 and P1, the mutant INL network grew to become much more elaborate than the control network of any age (Fig. 5A,B,E,F; Fig. 5-Supplement 1). Individual P1 SACs had larger INL arbors than control SACs (Fig. 5-Supplement 1), even though their IPL arbors were smaller (Fig. 5C), suggesting that they preferentially projected to the soma layer. Supporting this notion, P1 mutant SACs often projected primary dendrites towards each other, reminiscent of E16 newborn SACs (Fig. 5D). These findings suggest that mutant SACs continued to grow soma-directed arbors at an age when control SACs

238 exclusively targeted the IPL (Fig. 5D; Fig. 2-Supplement 1). In addition to being more elaborate,
239 mutant soma-directed arbors were also more persistent: Control SACs mostly eliminated these
240 arbors by P3 but mutants maintained them (Fig. 5B,F). Together, our data suggest that MEGF10
241 governs a developmental transition from soma-directed to IPL-directed arbor growth: Whereas
242 control SACs have only a brief period of soma-directed growth, switching to IPL ramification by
243 P0, *Megf10* mutant SACs do not make this transition and instead persist in soma-layer
244 innervation (Fig. 5G). This phenotype is consistent with a failure of homotypic recognition (Fig.
245 3). We conclude that, because MEGF10 regulates IPL innervation in this way, MEGF10 is
246 required for initial formation of SAC IPL sublayers at P0-1

247 **SAC dendrite targeting requires transcellular MEGF10 signaling**

248 Given the similar phenotypes of *Megf10* mutant and solitary *Ptf1a*^{cKO} SACs, we
249 hypothesized that MEGF10 is the molecular cue that triggers IPL innervation upon SAC-SAC
250 contact. A key prediction of this model is that SACs should require MEGF10 signals from their
251 neighbors to target their dendrites properly. To test this prediction, we generated a conditional
252 *Megf10*^{flox} allele and used it to create a situation where *Megf10*$^{+}$ SACs were surrounded by
253 *Megf10*$^{-}$ mutant cells. This was accomplished via the same *Six3:Cre* strategy that we employed
254 in our *Ptf1a*^{cKO} studies (Fig. 3A-C). In central retina of *Six3:Cre; Megf10*$^{flox/lacZ}$ (*Six3-Megf10*^{cKO})
255 animals, the vast majority of cells expressed a Cre-dependent GFP reporter, indicating that they
256 lacked *Megf10* function (Fig. 6A). Accordingly, SACs projected exuberantly to the INL and
257 sublayer formation was disrupted, as in null mutants (Fig. 6B; Fig. 6-Supplement 1).

258 In peripheral retina, some SACs escaped Cre activity, leading to absence of the GFP
259 reporter and continued MEGF10 protein expression (Fig. 6A,B; Fig. 6-Supplement 1). Our
260 model predicts that these cells should have mutant dendrite phenotypes despite retaining

MEGF10. To test this prediction, we imaged βgal-stained OFF SACs from *Six3-Megf10*^{cKO} and littermate control mice at P2. This age was chosen because wild-type and null mutant mice showed a large difference in SAC INL projection frequency (Fig. 5F). In littermate controls, we found that βgal^{+} SACs rarely projected to the INL (Fig. 6C,D); therefore, they behaved like control SACs from earlier experiments (Fig. 5F). By contrast, *Megf10*$^{+}$ SACs surrounded by mutant SACs in *Six3-Megf10*^{cKO} retina showed a high rate of INL projections, nearly identical to their *Megf10*$^{-}$ neighbors (Fig. 6B,D; Fig. 6-Supplement 1). Thus, when *Megf10*$^{+}$ SACs are deprived of MEGF10 signal from adjacent SACs, they make exuberant soma-directed projections. This finding implicates MEGF10 as a transcellular signal that controls SAC dendrite targeting.

Next we investigated how SACs receive this MEGF10 signal from their neighbors. Given that MEGF10 can function as a receptor in other contexts (Chung et al., 2013; Kay et al., 2012), we speculated that MEGF10 might act as its own receptor. In support of this idea, co-immunoprecipitation experiments using intracellularly truncated *Megf10* constructs showed that MEGF10 can interact with itself through its extracellular domain (Fig. 6I,J; Fig. 6-Supplement 2). Thus, MEGF10 appears biochemically capable of acting as both ligand and receptor.

If MEGF10 is indeed a receptor in this context, SACs should require it to detect contact with MEGF10-expressing homotypic neighbors. To test this prediction, we asked whether removal of *Megf10* from a single SAC, during the period of soma-directed homotypic contact, would impair its IPL innervation despite normal MEGF10 expression by surrounding cells. We used *Chat*^{Cre} to achieve sparse recombination in SACs of neonatal mice, as in the anatomy experiments described above (Fig. 2I-L; Fig. 5E). In *Chat-Megf10*^{cKO} animals, MEGF10 immunostaining was used to identify SACs that lost MEGF10 protein prior to P3 – i.e., during

the period when soma-directed arbors are present (Fig. 6F,G; Fig. 6-Supplement 1). MEGF10^{-} cells constituted a small minority of SACs at P3, meaning that they were generally surrounded by MEGF10^{+} neighbors (Fig. 6-Supplement 1). In this context, MEGF10^{-} SACs produced more exuberant soma-directed arbors than neighboring MEGF10^{+} cells, while sending only minimal arbors into the IPL (Fig. 6E-H). Thus, single MEGF10^{-} SACs had phenotypes similar to SACs from mice entirely lacking *Megf10* (Fig. 6G,H; compare to Fig. 5E). By contrast, adjacent MEGF10^{+} cells in the same *Chat-Megf10*^{cKO} retinas were indistinguishable from littermate control SACs (Fig. 6E,F,H). Therefore, when *Megf10* is lost during dendro-somatic contact (but not after; see below), SACs make projection errors typical of neurons deprived of homotypic interactions, and they do so even if their neighbors express MEGF10 and are developing normally. Together, these experiments support the conclusion that MEGF10 is a receptor through which SACs detect each other to terminate soma-directed growth and initiate IPL innervation.

SAC errors persist to adulthood in *Megf10* mutants

We next asked whether neonatal MEGF10-mediated interactions influence the anatomy of SAC IPL sublayers at maturity. We found that SAC sublayers eventually formed (by P5; Fig. 7I,J), and were present in the mature *Megf10*$^{-/-}$ retina, but they were marred by numerous errors. Sporadically, and at apparently arbitrary retinal locations, two kinds of local laminar disruptions were apparent. First, there were discontinuities in the ON and OFF strata, such that mutant SACs did not completely innervate their sublaminae (Fig. 7A-C). Innervation gaps were not observed for other amacrine cells, indicating that SACs were selectively affected (Fig. 7-Supplement 1). Examination of single SACs revealed that while dendritic patterning substantially recovered between P1 and adulthood, SAC arbor territories remained significantly smaller in mutants (Fig.

306 7D). These phenotypes suggest that mutant SACs never fully made up for their initial IPL
307 innervation deficit, thereby contributing to gaps in the dendritic plexus.

308 The second type of error we observed in mature *Megf10*$^{-/-}$ IPL was ectopic SAC
309 projections outside their typical IPL strata (Fig. 7A,B,E). We suspected that these adult ectopias
310 arose due to persistence of exuberant P1-P3 projections, because both the morphology of the
311 ectopic network at each age, and the number of SACs projecting into it, were quite similar (Fig.
312 7E-G). However, there were also two notable anatomical differences between P1-3 and adult.
313 First, neonatal ectopically-projecting SACs sent fine arbors in many directions, while adult
314 ectopic projections formed discrete aggregates (Fig. 7E,F). Second, these adult aggregates were
315 located in the IPL, whereas neonatal arbors targeted the soma layers (Fig.7A,B,E,F,H). These
316 differences led us to consider the possibility that the two SAC arbor phenotypes might be
317 unrelated.

318 To test the idea that diffuse neonatal exuberant arbors give rise to clumpy mature ones,
319 we assessed changes in mutant SAC arbor anatomy across development. If our hypothesis is
320 correct, we would expect this analysis to identify a time when ectopic SAC arbors transition
321 between the two phenotypic states. Indeed, we found that this transition occurs at P5: Both arbor
322 aggregation and IPL localization first arose at this time (Fig. 7F,H-J). These transitions occurred
323 without a significant change in the number of mutant SACs projecting into the ectopic network
324 (Fig. 7G; Fig. 7-Supplement 1), suggesting that the same cells continued to participate in the
325 network but simply altered their anatomy between P3 and P5. Supporting this notion, we
326 identified individual P5 *Chat*^{mG}-labeled SACs that projected both to ectopic IPL strata and to the
327 soma layers, suggesting they were in the process of remodeling their arbors (Fig. 7H,J). Such
328 anatomy was never observed at earlier or later stages (Fig. 7H). These observations support the

329 conclusion that early exuberant INL arbors are converted into IPL ectopias, starting between P3
330 and P5.

331 Together, these studies of adult SAC anatomy demonstrate that DS circuit sublayer
332 formation is delayed and imperfect in the absence of MEGF10. While other mechanisms appear
333 to partially compensate for MEGF10 in generating the sublayers, such mechanisms are not
334 sufficient to prevent persistence of innervation gaps and laminar targeting errors. Thus, MEGF10
335 is essential for normal formation of the mature SAC IPL projection.

336 Next we sought to directly test the idea that MEGF10 is required early – at the time of
337 initial SAC homotypic contact – to ensure normal SAC IPL lamination at maturity. To this end,
338 we used *Megf10*^{flox} mice to delete MEGF10 at different times. Deletion prior to the onset of
339 homotypic contact, using the *Six3:Cre* line, fully phenocopied *Megf10*$^{-/-}$ adult IPL errors (Fig.
340 8A), suggesting a requirement for MEGF10 at the time of contact. To remove MEGF10 from
341 SACs that had already established homotypic contact, we used the *Chat*^{Cre} line. In this line, the
342 number of SACs expressing *Chat*^{Cre} gradually increases over the first postnatal days to
343 encompass the full SAC population (Xu et al., 2016). Therefore, *Chat-Megf10*^{cKO} mice can be
344 used both for early, sparse MEGF10 deletion (Fig. 6F-H) and for later, broad MEGF10 deletion.
345 MEGF10 immunostaining revealed that this late, broad deletion occurs between P3 and P5 (Fig.
346 6-Supplement 1), such that MEGF10 expression is largely preserved during the period when
347 homotypic soma-layer contacts exist (Fig. 2M), but is eliminated shortly thereafter. In this
348 *Chat*^{Cre}-mediated deletion regime, SAC laminar targeting and gap errors were exceedingly rare
349 (Fig. 8A). These experiments therefore define a time window for MEGF10 function: Adult IPL
350 targeting phenotypes require absence of MEGF10 during the soma-directed projection phase of
351 SAC development – i.e. prior to P3. Any additional activity of MEGF10 after P3 is dispensable

for the adult IPL phenotype. These findings strongly support a model whereby the functions of MEGF10 during early homotypic contact – i.e. promoting IPL innervation and terminating soma-directed arbor growth – are necessary for development of normal SAC IPL innervation at maturity.

Mosaic spacing errors do not account for SAC IPL phenotype in *Megf10* mutants

In addition to these laminar targeting errors, *Megf10* mutants also show disruptions in the mosaic spacing of SAC cell bodies across the retina: Instead of a regular, uniform distribution, mutant SAC positioning is random (Kay et al., 2012). We sought to determine whether loss of homogeneous SAC soma positioning in mutants contributes to their loss of homogeneous IPL innervation (Fig. 7A-E). If so, local variations in SAC soma and arbor density should be strongly correlated. We tested for soma-arbor correlations in two ways. First, we examined global correlations by determining the spatial cross-correlation between images of SAC cell bodies and of their underlying IPL arbors. This analysis revealed that soma and arbor positions were in fact more weakly correlated in mutants than in controls (Fig. 8-Supplement 1). Thus, even though soma-arbor correlations exist in mutants, they are not sufficient to explain mutant IPL arbor arrangements (Fig. 8-Supplement 1). Additional contributing factors likely include changes in dendritic arbor size (Fig. 7D), or other deficits arising from the early delay in IPL innervation.

Next we addressed soma-IPL correlations on a single-cell level. To do this, we first developed a way to score the severity of the mosaic phenotype on a cell-by-cell basis. The spatial arrangement of a SAC relative to all of its nearest neighbors was quantified by measuring its unique territory (i.e. Voronoi domain; see Methods). Because the mutant SAC distribution is random, there are many mutant cells that, by chance, are positioned quite normally relative to their neighbors; there are also many cells whose neighbors are abnormally near or far (Fig. 8C-E).

If soma position causes IPL projection errors, then SACs located in "normal" regions of mutant retina should make targeting errors less often than SACs located in perturbed regions. However, this was not the case: Across all territory sizes, the rate of ectopic IPL projection was quite uniform, and indistinguishable from the overall error rate for mutants (Fig. 8F). The only exception was cells with the very largest territories – larger than nearly all values (n = 7/515) in the control distribution. These cells made fewer ectopic projections than the typical mutant cell, but still made errors about 50% of the time (Fig. 8F). These results demonstrate that ectopic IPL lamination errors are largely independent of soma position, supporting the conclusion that ectopias arise due to persistence of early mistargeted SAC arbors.

These correlational anatomical studies of adult *Megf10*$^{-/-}$ retina suggested that disturbed SAC mosaics make only minimal contributions to the IPL projection phenotype. To test this idea experimentally, we used our *Megf10*^{flox} conditional allele. We found that deletion of MEGF10 after P3 in *Chat-Megf10*^{cKO} mice dissociated the two phenotypes: Mosaic patterning was disturbed in these animals, but IPL projections were largely normal (Fig. 8A,B). This finding demonstrates that IPL laminar perturbations are not an inevitable consequence of altered soma positioning. Altogether, these experiments support the notion that delayed IPL innervation and exuberant soma-layer arborization are the major source of perturbed SAC projections at maturity.

SAC IPL errors induce laminar targeting errors by their DS circuit partners

We next tested the impact of SAC IPL stratification errors on laminar targeting by their circuit partners. First, we examined ooDSGC IPL projections using the *Hb9:GFP* (Fig. 9A-C) and *Drd4:GFP* (Fig. 9-Supplement 1) transgenic lines, which label ooDSGC subtypes with different preferred directions (Trenholm et al., 2011; Huberman et al., 2009). In littermate control mice (n = 9), ooDSGC dendrites were tightly and selectively associated with SAC arbors,

as shown previously (Vaney and Pow, 2000). This association was maintained in *Megf10* mutants: Both normal and ectopic SAC IPL arbors reliably recruited ectopic ooDSGC projections (Fig. 9A-B; Fig. 9-Supplement 1; n = 240 ectopias from 5 mutants, >97% contained ooDSGC arbors). Further, when SAC gaps were present in the mutant IPL, ooDSGC dendrites typically grew around the gap edges and failed to enter them (Fig. 9C; Fig. 9-Supplement 1; n = 325 gaps from 5 mutants, >95% devoid of ooDSGC arbors). Thus, SACs provide both permissive cues required for ooDSGC IPL innervation, and also attractive cues sufficient to recruit ooDSGCs to the wrong IPL sublayer.

Next we determined the impact of altered SAC lamination on the axons of bipolar cells that participate in the DS circuit – i.e., the four types (BC2, BC3a, BC5, and BC7) that make extensive monosynaptic connections with SACs and ooDSGCs (Duan et al., 2014; Ding et al., 2016; Greene et al., 2016; Kim et al., 2014; Chen et al., 2014). Bipolar cells were marked with type-specific antibodies and mouse lines reported previously (Wässle et al., 2009; Duan et al., 2014), as well as a novel transgenic marker of BC5 (*Gjd2:GFP*; Fig. 9-Supplement 1). In wild-type retina, DS-circuit bipolar cells arborized in close contact with SAC dendrites; however, unlike ooDSGCs, they remained adjacent to SACs rather than overlapping them (Fig. 9D,E,G; Fig. 9-Supplement 1). This arrangement was preserved in *Megf10* mutants: Axons of all four bipolar cell types were recruited to ectopic IPL locations by mistargeted SAC arbors, where they stratified adjacent to SACs (Fig. 9D-G; Fig. 9-Supplement 1). For example, BC5 and BC7 terminals always sandwiched SAC arbors, regardless of their IPL location – even when doing so required formation of a supernumerary BC axon field between the normal and ectopic SAC sublayers (Fig. 9D,E). To quantify the mistargeting effect we measured the position of BC5 and BC7 terminals adjacent to ON SAC ectopias. Their arbors were pushed farther apart by SAC

arbor clumps (Fig. 9E,F), which shifted BC7 terminals significantly towards the GCL by ~4 μm (69 ± 0.8% of IPL depth in control regions to 74 ± 1.9% in affected regions; mean ± S.E.M.; n = 21 control, 6 affected; 2-tailed t-test, $p = 0.0024$). No changes were seen in Syt2-labeled BC6 arbors, suggesting a specific effect on the bipolar cell types that make extensive contacts with SACs (data not shown). These observations indicate that DS-circuit bipolar cells, like ooDSGCs, respond to SAC attractive cues. However, in contrast to ooDSGCs, bipolar cell projections were minimally affected by SAC IPL gaps. While BC5 and BC7 terminals were slightly mispositioned in the absence of SAC arbors – they were closer together – innervation of gap regions was otherwise normal (Fig. 9D-F; Fig. 9-Supplement 1). Thus, DS-circuit bipolar axons either do not require SAC-derived signals for IPL innervation, or the relevant signals are capable of acting over larger distances than the typical SAC IPL gap size (35-45 μm maximum diameter). Altogether, these analyses of DS circuit anatomy in *Megf10* mutants support the notion that early-stratifying SACs form a scaffold that directs IPL laminar targeting of their circuit partners using multiple guidance cues.

Early SAC homotypic interactions impact DS circuit function

Finally, we investigated the extent to which developmental events controlled by MEGF10 affect DS circuit function. We sought to determine whether the anatomical perturbations caused by loss of MEGF10 – SAC laminar targeting and mosaic spacing errors – alter direction coding by ooDSGCs. To do this we recorded from wild-type and *Megf10*$^{-/-}$ retinas on a large-scale multielectrode array (Field et al., 2007; Yu et al., 2017). ooDSGCs were identified based on their responses to drifting gratings and moving bars (see Methods), which unambiguously distinguished them from other recorded RGCs (Fig. 10A). Because MEGF10 is not expressed in

the adult DS circuit (Kay et al., 2012), we could be confident that any mutant physiological phenotypes reflect anatomical changes that arose during development.

These experiments revealed that ooDSGCs with robust direction selectivity were present in both wild-type and *Megf10*$^{-/-}$ retinas (Fig. 10A,B), and constituted a similar fraction of the RGC population in both strains (wild-type: 80/609, 13.1%; mutant: 74/551, 13.4%). Furthermore, loss of *Megf10* did not alter the organization of ooDSGC preferred directions along cardinal axes (Oyster and Barlow, 1967), or the fraction of ooDSGCs preferring each direction (Fig. 10-Supplement 1). These results are consistent with the observation that mutant SACs remain paired with ooDSGC dendrites and bipolar cell axons even when normal lamination and arbor spacing are disrupted. They indicate that the qualitative functional properties of the circuit are still present.

However, a more careful examination of DS tuning properties in *Megf10*$^{-/-}$ retinas revealed clear quantitative differences in ooDSGC responses. Moving bars were used to measure the width and strength of direction tuning for each identified ooDSGC across the populations recorded on the electrode array (Fig. 10C). Tuning width was measured as the circular standard deviation of the tuning curve, while tuning strength was measured as the normalized response difference to motion in the preferred and null directions (see Methods). These experiments revealed systematic shifts toward broader (Fig. 10D) and weaker (Fig. 10E) direction tuning across the population of ooDSGCs in *Megf10* mutant retinas. This was mainly due to higher null direction spiking among ooDSGCs in mutants (Fig. 10B,C,E). Furthermore, these effects on tuning width and strength persisted across a broad range of stimulus contrasts (Fig. 10-Supplement 1). These results demonstrate that disruption of MEGF10-dependent developmental patterning degrades the precision and strength of ooDSGC direction tuning. They further suggest

that perturbations to the anatomical regularly of the circuit across space (e.g. laminar uniformity and SAC spacing) may effectively introduce noise in the DS circuit that broadens and weakens direction tuning (see Discussion).

This idea led us to consider additional functional properties of ooDSGCs that might depend on the spatial regularity of the DS circuit, and therefore might be perturbed in *Megf10* mutants. One such property is the generation of symmetric DS responses to stimuli that are darker or brighter than the background (Fig. 10F,G). This ON-OFF symmetry allows the DS response to be largely insensitive to contrast reversals (Amthor and Grzywacz, 1993); it arises because ooDSGCs receive highly symmetric SAC inputs in both ON and OFF sublayers (Fig. 1A). In *Megf10* mutants, ON-OFF anatomical symmetry is disturbed, because ON and OFF SAC errors are not spatially correlated (Fig. 7A-C). We hypothesized that this might lead to disparities in the direction tuning of individual cells' ON and OFF responses. Indeed, *Megf10*$^{-/-}$ ooDSGCs exhibited greater separation (i.e. less coherence) between their ON and OFF preferred directions than wild-type ooDSGCs, across a broad range of contrasts (Fig. 10H; Fig. 10-Supplement 1). These results support the idea that MEGF10 serves to establish a highly uniform and regular network of SAC dendrites (via controlling both the precise timing of INL lamination and through regularizing inter-SAC spacing), the net effect of which is to allow greater precision and coherence in the direction tuning of ooDSGCs.

DISCUSSION

Neural circuits typically consist of multiple cell types born at different places and times, raising the question of how circuit partners manage to converge at a common site for selective synapse formation. Here we describe a developmental strategy that the retinal DS circuit uses to solve this problem. We show that SACs coordinate amongst themselves to assemble a dendritic scaffold that subsequently recruits projections from their DS circuit partners. By identifying for the first time a genetic manipulation – loss of *Megf10* – that causes SACs to misproject outside their two typical IPL layers, we uncover mechanisms by which SACs assemble this dendritic scaffold. Further, we use *Megf10* mutants to examine the effects on DS circuit anatomy and function when SAC sublayer formation is disrupted. We find that MEGF10 establishes DS circuit spatial homogeneity across the retina, both by controlling IPL innervation patterns and by positioning SAC cell bodies. In *Megf10* mutants, disruptions in circuit homogeneity occur with minimal effects on radial SAC dendrite anatomy or synaptic partnering, making the phenotype unique among DS circuit developmental mutants. Finally, we find that this abnormal spatial pattern degrades DS circuit function by broadening the range of directions to which ooDSGCs will respond, and by weakening overall direction selectivity. These results provide new insight into general strategies for circuit development, as well as the specific mechanisms that ensure functional assembly of the DS circuit.

Homotypic recognition as a mechanism regulating dendrite differentiation

During radial migration, newborn central nervous system neurons have a multipolar morphology, but on arrival at their final position within the tissue they become highly polarized (Nadarajah et al., 2001; Tabata and Nakajima, 2003; Cooper, 2014; Chow et al., 2015; Krol et al., 2016; Hinds and Hinds, 1978). This morphological change enables elaboration of dendrites and

integration into local circuitry. If dendrite differentiation begins early, migration is impaired (Hoshiba et al., 2016), suggesting that the transition from migratory to mature morphology must be highly regulated to ensure that neurons only differentiate once they arrive at their final position. The extracellular cues that signal arrival are poorly understood in most nervous system regions.

Here we show that SACs use homotypic recognition, mediated by MEGF10, to initiate IPL-directed dendrite morphogenesis. When deprived of homotypic neighbors or MEGF10, SACs at the IPL retain a multipolar morphology (compare Fig. 2C to Figs. 3F, 5B) instead of polarizing arbors towards the IPL. This indicates that the transition from migratory to mature morphology is impaired in the absence of SAC homotypic recognition. We show that migrating SACs first establish homotypic contact upon arrival at the inner retina. At this stage they are still multipolar (Fig. 2D,E), but they orient primary dendrites towards each other, projecting within the INBL to contact their SAC neighbors. These contacts occur prior to IPL innervation, and are required for it to occur in a timely manner. SACs lacking neighbors or the molecular means to detect them (i.e., MEGF10) appear to persist in this multipolar soma-targeting phase, causing over-innervation of the soma layers and delaying IPL innervation (Fig. 5G). Thus, establishment of homotypic contact is a key checkpoint for the progression of SAC dendrite differentiation and IPL sublayer morphogenesis.

We propose that the function of this checkpoint is to ensure that SACs elaborate dendrites only when they have arrived adjacent to the IPL. The presence of other SACs that have already completed their migration is a reliable indicator of arrival in the proper location. Because soma-directed SAC contacts appear earliest, and because MEGF10 selectively influences IPL innervation during the period when they exist, we favor the notion that the key homotypic

530 interactions occur through these arbors. However, we cannot exclude that IPL-based interactions
531 also play a role. INL-directed arbors resembling those we describe can be discerned in many
532 developing zebrafish amacrine cells (Godinho et al., 2005; Chow et al., 2015), raising the
533 possibility that this mechanism applies across species and across other amacrine cell types.
534 Because most neurons require a way to control when and where they differentiate, we anticipate
535 that this homotypic contact strategy, or variations upon it, may have important roles in the
536 differentiation of other CNS neurons at the completion of their radial migration.

537 **MEGF10 as the signal mediating SAC homotypic recognition**

538 We conclude that MEGF10 is the molecule responsible for homotypic recognition during
539 SAC IPL innervation, for four reasons. First, MEGF10 is expressed at the right time and place to
540 assume this role: It is expressed selectively in SACs (Fig. 1), upon conclusion of their radial
541 migration, and in the soma-layer arbors that we propose mediate recognition (Fig. 4). Second,
542 *Megf10* null mutant SACs phenocopy the dendrite polarization errors seen in solitary *Ptf1a*^{cKO}
543 SACs, suggesting that homotypic recognition requires *Megf10*. Third, co-immunoprecipitation
544 experiments indicate that MEGF10 interacts with itself via its extracellular domain, suggesting it
545 could act as both ligand and receptor. While this biochemical interaction may take place in the
546 *cis* configuration, the fourth line of evidence indicates that MEGF10 interacts in *trans* as well:
547 Using a conditional-null *Megf10* allele in vivo, we show that MEGF10 is required on the cell that
548 sends homotypic signals as well as the cell receiving those signals. Loss of MEGF10 on either
549 side leads to dendritic phenotypes resembling solitary SACs and *Megf10* null mutants. Together,
550 these data are consistent with a model whereby SAC-SAC contact initiates a transcellular
551 MEGF10 homophilic interaction, in which MEGF10 serves as both receptor and ligand to trigger
552 the switch from migratory to mature morphology.

553 This homophilic model of MEGF10 function is consistent with its role during
554 establishment of mosaic cell body patterning (Kay et al. 2012). In that context, MEGF10 acts as
555 ligand and receptor to mediate cell-cell repulsion, thereby spacing SAC somata evenly across the
556 retina. Here we discover a second MEGF10 function in SAC IPL innervation. Because the two
557 SAC phenotypes have different underlying cell biology (soma movement vs. dendrite dynamics),
558 and different temporal requirements for MEGF10 function (Fig. 8A,B), it seems unlikely that
559 they reflect disruption of a single biological event. Instead, MEGF10 appears to act at distinct,
560 albeit partially overlapping times, to control different aspects of SAC development, each of
561 which are regulated by contact with homotypic neighbors.

562 **Formation of SAC IPL sublayers**

563 Our results shed light on the mechanisms controlling SAC dendrite lamination. While
564 repulsion mediated by Sema6a and PlexinA2 prevents OFF SACs from straying to the ON
565 sublayer (Sun et al., 2013), molecules required for formation of the SAC sublayers have not been
566 identified. We show that SACs deprived of homotypic neighbors or MEGF10 initially fail to
567 form IPL sublayers, and when they eventually do so, their strata are riddled with errors. Both the
568 lack of sublayers at early stages and the dendritic mistargeting to inappropriate sublayers at
569 maturity are novel SAC phenotypes; they implicate MEGF10 as a key player in forming SAC
570 IPL sublayer-specific projections.

571 It is generally assumed that sublayer formation has two basic molecular requirements: 1)
572 Attractive/adhesive molecules that mediate co-fasciculation of stratified arbors; and 2) repulsive
573 cues that prevent straying of arbors into other sublayers (Lefebvre et al., 2015; Sanes and
574 Yamagata, 2009). Our MEGF10 studies suggest an additional, earlier requirement for cell-cell
575 interactions that occur prior to neuropil innervation. The purpose of this surprisingly early SAC-

SAC interaction, we propose, is to ensure that SACs grow dendrites at the right time and place to co-fasciculate with their SAC neighbors. When IPL arborization is delayed by loss of *Megf10*, two SAC errors ensue. First, SACs generate mistargeted dendritic material that persists as ectopic IPL sublayers. Second, SACs never completely innervate their sublayers, resulting in fragmented IPL strata. This failure is caused by delays rather than an ongoing requirement for MEGF10 during later stages of arbor growth, as shown by conditional mutant experiments. Thus, our findings support the idea that timing is critical to the sequential lamination of the IPL: When SAC dendrites arrive in the IPL too late, they encounter a different cellular and molecular milieu that may not support the proper development of their arbors. In this view, the normal role of MEGF10 in DS circuit assembly is to instigate SAC dendrite outgrowth at the crucial time when laminar self-assembly can occur.

SACs may face an additional obstacle to overcoming their delayed IPL innervation in *Megf10* mutants – abnormal soma positioning. While mosaic spacing errors do not account for much of the *Megf10* mutant IPL phenotype, the placement of IPL arbor gaps might be at least partly explained by soma position. This effect was only seen in mutant conditions that also produced IPL innervation delay – mosaic disturbance alone was not sufficient to produce gaps. If SACs are struggling to make up for their delayed IPL innervation, it is plausible that increasing the distance between SACs (as happens sporadically due to random positioning) might further hinder the development of complete retinal coverage.

SACs as a scaffold for DS circuit assembly

Because of their early stratification, SAC dendrites have been proposed to act as a scaffold that guides assembly of the DS circuit (Stacy and Wong, 2003). A key prediction of this model is that laminar targeting of later-stratifying cell types should depend on the existence of

599 this scaffold. We show using a SAC-specific manipulation – removal of *Megf10* – that disruption
600 of SAC stratification causes their bipolar and ooDSGC circuit partners to make corresponding
601 projection errors. Based on the kinds of errors we observed, SACs appear to provide attractive,
602 permissive, and even repulsive arbor sorting cues to influence the laminar positioning of their
603 circuit partners. This work thus constitutes the first critical test of the scaffolding model, and
604 provides strong support for it. We find that SACs use homotypic interactions to initiate
605 formation of their circuit sublayers, and then heterotypic interactions to recruit circuit partners to
606 join them. The scaffolding functions may be mediated in part by Cadherins 8 and 9, which
607 regulate interactions between SAC dendrites and DS circuit bipolar cell axons (Duan et al., 2014).
608 Molecular mediators of ooDSGC-SAC dendrite interactions remain to be identified.

609 Evidence that the SAC scaffold can be repulsive came from our observations of BC axon
610 anatomy. In wild-type retina, we were surprised to note how completely the BC3a, BC5, and
611 BC7 axon terminals were excluded from the SAC territory – they contacted it but did not enter
612 (Fig. 9D-G; Fig. 9-Supplement 1). Moreover, in *Megf10* mutants, the laminar distance between
613 BC5 and BC7 terminals was reduced in the absence of SAC arbors, and increased in the presence
614 of SAC ectopias, further suggesting the existence of local SAC-BC repulsion. The finding that
615 SACs exclude bipolar circuit partners from their sublayers appears at first counterintuitive. But
616 given that no bipolar cell type is exclusively devoted to the DS circuit (Wässle et al., 2009;
617 Greene et al., 2016; Kim et al., 2014), a mechanism must exist to ensure that they can also
618 contact non-DS partners. We speculate that SACs initially recruit their bipolar partners using
619 long-range attractive cues, and then use contact-repulsion (or an equivalent arbor sorting
620 mechanism) to displace bipolar arbors such that they remain in contact with the SAC layers but

621 also innervate adjacent layers. This model is consistent with bipolar arbor phenotypes in *Megf10*
622 mutants, but will require further study.

623 **Role of MEGF10 in the functional assembly of DS circuitry**

624 We found that impairment of SAC interactions in the perinatal retina causes permanent
625 functional DS circuit deficits. In *Megf10* mutants, direction tuning of ooDSGCs becomes broader
626 and weaker, and their ON/OFF preferred directions are less aligned. Direction tuning is degraded
627 in large part because mutant ooDSGCs have aberrant spiking responses to null-direction stimuli.
628 This suggests that impaired null-direction inhibition – which arises from SACs – is a key
629 contributor to the phenotype. Broader ooDSGC tuning curves have been shown, in modeling
630 studies, to degrade population-level coding of directional information, and the ability of
631 downstream neurons to extract such information (Fiscella et al., 2015). Thus, the physiological
632 phenotypes we identified are likely sufficient to impair the ability of mutant retina to
633 appropriately relay visual information.

634 Dysfunctional DS circuit physiology in *Megf10* mutants is almost certainly a
635 consequence of its effects on development, because neurons do not express MEGF10 beyond the
636 second postnatal week (Kay et al., 2012). Further, even though MEGF10 is expressed by Müller
637 glia in adulthood, we have been unable to detect any changes in Müller glia anatomy or
638 interactions with DS circuit synapses upon loss of *Megf10* function (Wang et al., 2017; J.W. and
639 J.N.K., unpublished observations). We therefore conclude that anatomical changes to the DS
640 circuit arising during development are responsible for circuit dysfunction.

641 The fundamental change to DS circuit anatomy in *Megf10* mutants is altered distribution
642 of arbors and synapses, unlike other manipulations which simply serve to destroy SAC radial
643 morphology or disrupt synaptic partnering among DS circuit cells (Sun et al., 2013; Duan et al.,

2014; Kostadinov and Sanes, 2015; Peng et al., 2017). In *Megf10* mutants, the combined effect of mosaic spacing defects and IPL laminar targeting errors is to disturb the regularity of SAC IPL innervation. As a result, some parts of the visual map become over-innervated (e.g. Fig. 9A) while others are uninnervated (Fig. 9C). In turn, ooDSGCs are recruited to the over-innervated regions and excluded from uninnervated gaps, likely causing sporadic local inhomogeneity in synapse density across visual space. According to some models of DS, which posit that the total amount of SAC inhibition is the key factor underlying DS responsiveness, these relatively small-scale changes would be considered unlikely to change circuit function (Taylor and Vaney, 2002; Demb, 2007). A more recent alternate view is that the fine spatial arrangement of glutamatergic inputs to SACs, and the synaptic balance of SAC and bipolar input onto ooDSGC dendrites, are both important for DS responses (Ding et al., 2016; Vlasits et al., 2016; Poleg-Polsky and Diamond, 2016; Sethuramanujam et al., 2016, 2017). The finding that *Megf10* mutants have DS tuning phenotypes suggests that local synaptic arrangements are indeed important for the DS computation. More broadly, this finding shows that the developmental mechanisms we describe here are important for enabling circuit function, raising the possibility that other circuits throughout the retina and CNS may use similar developmental mechanisms to establish their functional connectivity.

ACKNOWLEDGEMENTS

For financial support we thank the National Eye Institute (EY024694 to JNK; EY026344 to TAR; EY024567 to GDF; EY5722 to Duke University); Pew Charitable Trusts, E. Matilda Ziegler Foundation, McKnight Endowment Fund for Neuroscience, Alfred P. Sloan foundation (JNK); the Whitehall Foundation (GDF); and Research to Prevent Blindness Unrestricted Grant (Duke University). We thank Sidney Kuo and Greg Schwartz for suggesting use of the *Gjd2:GFP* mouse line; members of the Kay lab and Cagla Eroglu for their comments on the manuscript; Megan Stogsdill and Ari Pereira for mouse colony support; and X. Duan and J. Sanes (Harvard) for $Kcng4^{Cre}$ mice.

COMPETING INTERESTS

The authors have no competing interests to disclose.

673 **REFERENCES**

674 Amthor, F.R., and N.M. Grzywacz. 1993. Inhibition in ON-OFF directionally selective ganglion
675 cells of the rabbit retina. *J. Neurophysiol.* 69:2174–87.

676 Baier, H. 2013. Synaptic laminae in the visual system: molecular mechanisms forming layers of
677 perception. *Annu. Rev. Cell Dev. Biol.* 29:385–416. doi:10.1146/annurev-cellbio-101011-
678 155748.

679 Cai, D., K.B. Cohen, T. Luo, J.W. Lichtman, and J.R. Sanes. 2013. Improved tools for the
680 Brainbow toolbox. *Nat. Methods*. 10:540–7. doi:10.1038/nmeth.2450.

681 Chen, M., S. Lee, S.J.H. Park, L.L. Looger, and Z.J. Zhou. 2014. Receptive field properties of
682 bipolar cell axon terminals in direction-selective sublaminas of the mouse retina. *J.*
683 *Neurophysiol.* 112:1950–62. doi:10.1152/jn.00283.2014.

684 Chow, R.W., A.D. Almeida, O. Randlett, C. Norden, and W. a. Harris. 2015. Inhibitory neuron
685 migration and IPL formation in the developing zebrafish retina. *Development*. 142:2665–77.
686 doi:10.1242/dev.122473.

687 Chung, W.-S., L.E. Clarke, G.X. Wang, B.K. Stafford, A. Sher, C. Chakraborty, J. Joung, L.C.
688 Foo, A. Thompson, C. Chen, S.J. Smith, and B.A. Barres. 2013. Astrocytes mediate synapse
689 elimination through MEGF10 and MERTK pathways. *Nature*. 504:394–400.
690 doi:10.1038/nature12776.

691 Cooper, J.A. 2014. Molecules and mechanisms that regulate multipolar migration in the
692 intermediate zone. *Front. Cell. Neurosci.* 8:386. doi:10.3389/fncel.2014.00386.

693 Deans, M.R., A. Krol, V.E. Abraira, C.O. Copley, A.F. Tucker, and L. V Goodrich. 2011.
694 Control of neuronal morphology by the atypical cadherin Fat3. *Neuron*. 71:820–32.
695 doi:10.1016/j.neuron.2011.06.026.

696 Demb, J.B. 2007. Cellular mechanisms for direction selectivity in the retina. *Neuron*. 55:179–86.
697 doi:10.1016/j.neuron.2007.07.001.

698 Ding, H., R.G. Smith, A. Poleg-Polsky, J.S. Diamond, and K.L. Briggman. 2016. Species-
699 specific wiring for direction selectivity in the mammalian retina. *Nature*. 535:105–110.
700 doi:10.1038/nature18609.

701 Duan, X., A. Krishnaswamy, I. De la Huerta, and J.R. Sanes. 2014. Type II cadherins guide
702 assembly of a direction-selective retinal circuit. *Cell*. 158:793–807.
703 doi:10.1016/j.cell.2014.06.047.

704 Field, G.D., J.L. Gauthier, A. Sher, M. Greschner, T.A. Machado, L.H. Jepson, J. Shlens, D.E.
705 Gunning, K. Mathieson, W. Dabrowski, L. Paninski, A.M. Litke, and E.J. Chichilnisky.
706 2010. Functional connectivity in the retina at the resolution of photoreceptors. *Nature*.
707 467:673–7. doi:10.1038/nature09424.

708 Field, G.D., A. Sher, J.L. Gauthier, M. Greschner, J. Shlens, A.M. Litke, and E.J. Chichilnisky.
709 2007. Spatial properties and functional organization of small bistratified ganglion cells in

primate retina. *J. Neurosci.* 27:13261–72. doi:10.1523/JNEUROSCI.3437-07.2007.

Fiscella, M., F. Franke, K. Farrow, J. Müller, B. Roska, R. Azeredo da Silveira, and A. Hierlemann. 2015. Visual coding with a population of direction-selective neurons. *J. Neurophysiol.* 114:2485–2499. doi:10.1152/jn.00919.2014.

Fujitani, Y., S. Fujitani, H. Luo, F. Qiu, J. Burlison, Q. Long, Y. Kawaguchi, H. Edlund, R.J. MacDonald, T. Furukawa, T. Fujikado, M.A. Magnuson, M. Xiang, and C.V.E. Wright. 2006. Ptf1a determines horizontal and amacrine cell fates during mouse retinal development. *Development*. 133:4439–50. doi:10.1242/dev.02598.

Furuta, Y., O. Lagutin, B.L. Hogan, and G.C. Oliver. 2000. Retina- and ventral forebrain-specific Cre recombinase activity in transgenic mice. *Genesis*. 26:130–2.

Galli-Resta, L., G. Resta, S.S. Tan, and B.E. Reese. 1997. Mosaics of islet-1-expressing amacrine cells assembled by short-range cellular interactions. *J. Neurosci.* 17:7831–8.

Godinho, L., J.S. Mumm, P.R. Williams, E.H. Schroeter, A. Koerber, S.W. Park, S.D. Leach, and R.O.L. Wong. 2005. Targeting of amacrine cell neurites to appropriate synaptic laminae in the developing zebrafish retina. *Development*. 132:5069–79. doi:10.1242/dev.02075.

Green, E.S., J.L. Stubbs, and E.M. Levine. 2003. Genetic rescue of cell number in a mouse model of microphthalmia: interactions between Chx10 and G1-phase cell cycle regulators. *Development*. 130:539–52.

Greene, M.J., J.S. Kim, H.S. Seung, and EyeWirers. 2016. Analogous Convergence of Sustained and Transient Inputs in Parallel On and Off Pathways for Retinal Motion Computation. *Cell Rep.* 14:1892–900. doi:10.1016/j.celrep.2016.02.001.

Hinds, J.W., and P.L. Hinds. 1978. Early development of amacrine cells in the mouse retina: an electron microscopic, serial section analysis. *J. Comp. Neurol.* 179:277–300. doi:10.1002/cne.901790204.

Hoshiba, Y., T. Toda, H. Ebisu, M. Wakimoto, S. Yanagi, and H. Kawasaki. 2016. Sox11 Balances Dendritic Morphogenesis with Neuronal Migration in the Developing Cerebral Cortex. *J. Neurosci.* 36:5775–84. doi:10.1523/JNEUROSCI.3250-15.2016.

Huberman, A.D., W. Wei, J. Elstrott, B.K. Stafford, M.B. Feller, and B.A. Barres. 2009. Genetic identification of an On-Off direction-selective retinal ganglion cell subtype reveals a layer-specific subcortical map of posterior motion. *Neuron*. 62:327–34. doi:10.1016/j.neuron.2009.04.014.

Kay, J.N., M.W. Chu, and J.R. Sanes. 2012. MEGF10 and MEGF11 mediate homotypic interactions required for mosaic spacing of retinal neurons. *Nature*. 483:465–9. doi:10.1038/nature10877.

Kay, J.N., I. De la Huerta, I.-J. Kim, Y. Zhang, M. Yamagata, M.W. Chu, M. Meister, and J.R. Sanes. 2011. Retinal ganglion cells with distinct directional preferences differ in molecular identity, structure, and central projections. *J. Neurosci.* 31:7753–62. doi:10.1523/JNEUROSCI.0907-11.2011.

748 Kay, J.N., and J.R. Sanes. 2013. Development of retinal arbors and synapses. *In* The New Visual
749 Neurosciences. J.S. Werner and L.M. Chalupa, editors. MIT Press, Cambridge.

750 Kim, J.S., M.J. Greene, A. Zlateski, K. Lee, M. Richardson, S.C. Turaga, M. Purcaro, M.
751 Balkam, A. Robinson, B.F. Behabadi, M. Campos, W. Denk, H.S. Seung, and EyeWirers.
752 2014. Space-time wiring specificity supports direction selectivity in the retina. *Nature*.
753 509:331–6. doi:10.1038/nature13240.

754 Knabe, W., S. Washausen, N. Happel, and H.J. Kuhn. 2007. Development of starburst
755 cholinergic amacrine cells in the retina of Tupaia belangeri. *J. Comp. Neurol.* 502:584–597.
756 doi:10.1002/cne.

757 Kostadinov, D., and J.R. Sanes. 2015. Protocadherin-dependent dendritic selfavoidance regulates
758 neural connectivity and circuit function. *Elife*. 4. doi:10.7554/eLife.08964.

759 Krah, N.M., J.-P. De La O, G.H. Swift, C.Q. Hoang, S.G. Willet, F. Chen Pan, G.M. Cash, M.P.
760 Bronner, C.V. Wright, R.J. MacDonald, and L.C. Murtaugh. 2015. The acinar
761 differentiation determinant PTF1A inhibits initiation of pancreatic ductal adenocarcinoma.
762 *Elife*. 4. doi:10.7554/eLife.07125.

763 Krol, A., S.J. Henle, and L. V Goodrich. 2016. Fat3 and Ena/VASP proteins influence the
764 emergence of asymmetric cell morphology in the developing retina. *Development*.
765 143:2172–82. doi:10.1242/dev.133678.

766 Lefebvre, J.L., J.R. Sanes, and J.N. Kay. 2015. Development of dendritic form and function.
767 *Annu. Rev. Cell Dev. Biol.* 31:741–77. doi:10.1146/annurev-cellbio-100913-013020.

768 Madisen, L., T.A. Zwingman, S.M. Sunkin, S.W. Oh, H.A. Zariwala, H. Gu, L.L. Ng, R.D.
769 Palmiter, M.J. Hawrylycz, A.R. Jones, E.S. Lein, and H. Zeng. 2010. A robust and high-
770 throughput Cre reporting and characterization system for the whole mouse brain. *Nat.*
771 *Neurosci.* 13:133–40. doi:10.1038/nn.2467.

772 Matsuoka, R.L., K.T. Nguyen-Ba-Charvet, A. Parray, T.C. Badea, A. Chédotal, and A.L.
773 Kolodkin. 2011. Transmembrane semaphorin signalling controls laminar stratification in the
774 mammalian retina. *Nature*. 470:259–63. doi:10.1038/nature09675.

775 Morgan, J.L., A. Dhingra, N. Vardi, and R.O.L. Wong. 2006. Axons and dendrites originate
776 from neuroepithelial-like processes of retinal bipolar cells. *Nat. Neurosci.* 9:85–92.
777 doi:10.1038/nn1615.

778 Moshiri, A., E. Gonzalez, K. Tagawa, H. Maeda, M. Wang, L.J. Frishman, and S.W. Wang. 2008.
779 Near complete loss of retinal ganglion cells in the math5/brn3b double knockout elicits
780 severe reductions of other cell types during retinal development. *Dev. Biol.* 316:214–27.
781 doi:10.1016/j.ydbio.2008.01.015.

782 Muzumdar, M.D., B. Tasic, K. Miyamichi, L. Li, and L. Luo. 2007. A global double-fluorescent
783 Cre reporter mouse. *genesis*. 45:593–605. doi:10.1002/dvg.20335.

784 Nadarajah, B., J.E. Brunstrom, J. Grutzendler, R.O. Wong, and A.L. Pearlman. 2001. Two
785 modes of radial migration in early development of the cerebral cortex. *Nat. Neurosci.*

4:143–50. doi:10.1038/83967.

Nakhai, H., S. Sel, J. Favor, L. Mendoza-Torres, F. Paulsen, G.I.W. Duncker, and R.M. Schmid. 2007. Ptf1a is essential for the differentiation of GABAergic and glycinergic amacrine cells and horizontal cells in the mouse retina. *Development*. 134:1151–60. doi:10.1242/dev.02781.

Oesch, N., T. Euler, and W.R. Taylor. 2005. Direction-selective dendritic action potentials in rabbit retina. *Neuron*. 47:739–50.

Oyster, C.W., and H.B. Barlow. 1967. Direction-selective units in rabbit retina: distribution of preferred directions. *Science*. 155:841–842. doi:10.1126/science.155.3764.841.

Peng, Y.R., N.M. Tran, A. Krishnaswamy, D. Kostadinov, E.M. Martersteck, and J.R. Sanes. 2017. Satb1 Regulates Contactin 5 to Pattern Dendrites of a Mammalian Retinal Ganglion Cell. *Neuron*. 95:869–883.e6. doi:10.1016/j.neuron.2017.07.019.

Poleg-Polsky, A., and J.S. Diamond. 2016. Retinal Circuitry Balances Contrast Tuning of Excitation and Inhibition to Enable Reliable Computation of Direction Selectivity. *J. Neurosci.* 36:5861–76. doi:10.1523/JNEUROSCI.4013-15.2016.

Rawlins, E.L., T. Okubo, Y. Xue, D.M. Brass, R.L. Auten, H. Hasegawa, F. Wang, and B.L.M. Hogan. 2009. The role of Scgb1a1+ Clara cells in the long-term maintenance and repair of lung airway, but not alveolar, epithelium. *Cell Stem Cell*. 4:525–34. doi:10.1016/j.stem.2009.04.002.

Rossi, J., N. Balthasar, D. Olson, M. Scott, E. Berglund, C.E. Lee, M.J. Choi, D. Lauzon, B.B. Lowell, and J.K. Elmquist. 2011. Melanocortin-4 receptors expressed by cholinergic neurons regulate energy balance and glucose homeostasis. *Cell Metab.* 13:195–204. doi:10.1016/j.cmet.2011.01.010.

Sanes, J.R., and M. Yamagata. 2009. Many paths to synaptic specificity. *Annu. Rev. Cell Dev. Biol.* 25:161–95. doi:10.1146/annurev.cellbio.24.110707.175402.

Sanes, J.R., and S.L. Zipursky. 2010. Design principles of insect and vertebrate visual systems. *Neuron*. 66:15–36. doi:10.1016/j.neuron.2010.01.018.

Schindelin, J., I. Arganda-Carreras, E. Frise, V. Kaynig, M. Longair, T. Pietzsch, S. Preibisch, C. Rueden, S. Saalfeld, B. Schmid, J.-Y. Tinevez, D.J. White, V. Hartenstein, K. Eliceiri, P. Tomancak, and A. Cardona. 2012. Fiji: an open-source platform for biological-image analysis. *Nat. Methods*. 9:676–82. doi:10.1038/nmeth.2019.

Sethuramanujam, S., A.J. McLaughlin, G. DeRosenroll, A. Hoggarth, D.J. Schwab, and G.B. Awatramani. 2016. A Central Role for Mixed Acetylcholine/GABA Transmission in Direction Coding in the Retina. *Neuron*. 90:1243–56. doi:10.1016/j.neuron.2016.04.041.

Sethuramanujam, S., X. Yao, G. DeRosenroll, K.L. Briggman, G.D. Field, and G.B. Awatramani. 2017. “Silent” NMDA Synapses Enhance Motion Sensitivity in a Mature Retinal Circuit. *Neuron*. 96:1099–1111.e3. doi:10.1016/j.neuron.2017.09.058.

823 Stacy, R.C., and R.O.L. Wong. 2003. Developmental relationship between cholinergic amacrine
824 cell processes and ganglion cell dendrites of the mouse retina. *J. Comp. Neurol.* 456:154–66.
825 doi:10.1002/cne.10509.

826 Sun, L.O., Z. Jiang, M. Rivlin-Etzion, R. Hand, C.M. Brady, R.L. Matsuoka, K.-W. Yau, M.B.
827 Feller, and A.L. Kolodkin. 2013. On and off retinal circuit assembly by divergent molecular
828 mechanisms. *Science*. 342. doi:10.1126/science.1241974.

829 Tabata, H., and K. Nakajima. 2003. Multipolar migration: the third mode of radial neuronal
830 migration in the developing cerebral cortex. *J. Neurosci.* 23:9996–10001. doi:23/31/9996
831 [pii].

832 Taylor, W.R., and D.I. Vaney. 2002. Diverse synaptic mechanisms generate direction selectivity
833 in the rabbit retina. *J. Neurosci.* 22:7712–20.

834 Trenholm, S., K. Johnson, X. Li, R.G. Smith, and G.B. Awatramani. 2011. Parallel mechanisms
835 encode direction in the retina. *Neuron*. 71:683–94. doi:10.1016/j.neuron.2011.06.020.

836 Vaney, D.I., and D. V Pow. 2000. The dendritic architecture of the cholinergic plexus in the
837 rabbit retina: selective labeling by glycine accumulation in the presence of sarcosine. *J.*
838 *Comp. Neurol.* 421:1–13.

839 Vaney, D.I., B. Sivyer, and W.R. Taylor. 2012. Direction selectivity in the retina: symmetry and
840 asymmetry in structure and function. *Nat. Rev. Neurosci.* 13:194–208. doi:10.1038/nrn3165.

841 Visser, J.J., Y. Cheng, S.C. Perry, A.B. Chastain, B. Parsa, S.S. Masri, T.A. Ray, J.N. Kay, and
842 W.M. Wojtowicz. 2015. An extracellular biochemical screen reveals that FLRTs and Unc5s
843 mediate neuronal subtype recognition in the retina. *Elife*. 4:e08149.
844 doi:10.7554/eLife.08149.

845 Vlasits, A.L., R.D. Morrie, A. Tran-Van-Minh, A. Bleckert, C.F. Gainer, D.A. DiGregorio, and
846 M.B. Feller. 2016. A Role for Synaptic Input Distribution in a Dendritic Computation of
847 Motion Direction in the Retina. *Neuron*. 89:1317–1330. doi:10.1016/j.neuron.2016.02.020.

848 Wang, J., M.L. O'Sullivan, D. Mukherjee, V.M. Puñal, S. Farsiu, and J.N. Kay. 2017. Anatomy
849 and spatial organization of Müller glia in mouse retina. *J. Comp. Neurol.* 525:1759–1777.
850 doi:10.1002/cne.24153.

851 Wässle, H., C. Puller, F. Müller, and S. Haverkamp. 2009. Cone contacts, mosaics, and
852 territories of bipolar cells in the mouse retina. *J. Neurosci.* 29:106–17.
853 doi:10.1523/JNEUROSCI.4442-08.2009.

854 Whitney, I.E., P.W. Keeley, A.J. St John, A.G. Kautzman, J.N. Kay, and B.E. Reese. 2014. Sox2
855 regulates cholinergic amacrine cell positioning and dendritic stratification in the retina. *J.*
856 *Neurosci.* 34:10109–21. doi:10.1523/JNEUROSCI.0415-14.2014.

857 Xu, H.-P., T.J. Burbridge, M. Ye, M. Chen, X. Ge, Z.J. Zhou, and M.C. Crair. 2016. Retinal
858 Wave Patterns Are Governed by Mutual Excitation among Starburst Amacrine Cells and
859 Drive the Refinement and Maintenance of Visual Circuits. *J. Neurosci.* 36:3871–3886.
860 doi:10.1523/JNEUROSCI.3549-15.2016.

861 Yamagata, M., and J.R. Sanes. 2008. Dscam and Sidekick proteins direct lamina-specific
862 synaptic connections in vertebrate retina. *Nature*. 451:465–9. doi:10.1038/nature06469.

863 Yang, L., C.-L. Cai, L. Lin, Y. Qyang, C. Chung, R.M. Monteiro, C.L. Mummery, G.I. Fishman,
864 A. Cogen, and S. Evans. 2006. Isl1Cre reveals a common Bmp pathway in heart and limb
865 development. *Development*. 133:1575–85. doi:10.1242/dev.02322.

866 Yu, W.-Q., N.M. Grzywacz, E.-J. Lee, and G.D. Field. 2017. Cell-type specific changes in
867 retinal ganglion cell function induced by rod death and cone reorganization in rats. *J.*
868 *Neurophysiol.* jn.00826.2016. doi:10.1152/jn.00826.2016.

869

870 **MATERIALS AND METHODS**

871 **KEY REAGENTS TABLE**

REAGENT or RESOURCE	SOURCE	IDENTIFIER
Antibodies		
Megf10: rabbit, 1:1000	Kay et al., 2012	
Sox2: rabbit, 1:500	Abcam	ab97959
Sox2: goat, 1:500	Santa Cruz	sc-17320
ChAT: goat, 1:400	EMD Millipore	AB144P
Beta Galactosidase: rabbit, 1:5000	J. Sanes, Harvard	
GFP: chicken, 1:1000	Life Technologies	A10262
GFP (Co-IP): rabbit, 1:1000	Thermo Fisher Scientific	A-6455
AP-2a: mouse, 1:200	Developmental Studies Hybridoma Bank	3B5
RBPMS: guinea pig, 1:2000	N. Brecha, UCLA	
Chx10: sheep, 1:300	Exalpha	X1180P
Chx10: goat, 1:500	Santa Cruz	sc-21690
GAD65: rabbit, 1:1000	Millipore	AB1511
FLAG: mouse, 1:500	Sigma Aldrich	F-1804
VGLUT3 guinea pig	synaptic systems	135 204
Synaptotagmin-2 (Syt2), mouse, 1:250	Zebrafish International Resource Center	ZDB-ATB-081002-25
Isl1: mouse, 1:25	Developmental Studies Hybridoma Bank	39.4D5
Internexin: rabbit, 1:1000	EMD Millipore	AB5354
Normal Rabbit IgG	Cell signaling Technology	2729S
Normal Mouse IgG	Cell Signaling Technology	5415S
Alexa Fluor 488 AffiniPure Donkey Anti-Chicken: 1:1000	Jackson ImmunoResearch	703-545-155
Alexa Fluor 488 AffiniPure Donkey	Jackson	711-545-152

Anti-rabbit: 1:1000	ImmunoResearch	
Alexa Fluor 488 AffiniPure Donkey Anti-goat: 1:1000	Jackson ImmunoResearch	705-545-147
Alexa Fluor 488 AffiniPure Donkey Anti-mouse: 1:1000	Jackson ImmunoResearch	706-605-148
Alexa Fluor 647 AffiniPure Donkey Anti-rabbit: 1:1000	Jackson ImmunoResearch	705-605-147
Cy3-AffiniPure Donkey Anti-rabbit: 1:1000	Jackson ImmunoResearch	715-165-151
Cy3-AffiniPure Donkey Anti-Guinea Pig: 1:1000	Jackson ImmunoResearch	706-165-148
Cy3-AffiniPure Donkey Anti-Goat: 1:1000	Jackson ImmunoResearch	705-165-147
IRDye® 680RD Donkey anti-Mouse IgG (H + L): 1:1000	Li-Cor Biosciences	925-68072
IRDye® 800CW Donkey anti-Rabbit IgG (H + L): 1:1000	Li-Cor Biosciences	925-32213

Bacterial and Virus Strains

AAV9.hEF1a.lox.TagBFP.lox.eYFP.lox.WPRE.hGH-InvBYF(Harvard)	Penn Vector Core	AV-9-PV2453
AAV9.hEF1a.lox.mCherry.lox.mTFP1.lox.WPRE.hGH-InvCheTF(Harvard)	Penn Vector Core	AV-9-PV2454

Biological Samples

Chemicals, Peptides, and Recombinant Proteins

Fetal Bovine Serum	Life Technologies	16250-078
0.5% Trypsin-EDTA phenol red	Life Technologies	25300-054
Dulbecco's Modified Eagle Medium (DMEM)	Thermo Fisher Scientific	11995065
Penicillin Streptomycin	Thermo Fisher Scientific	15070063
Opti-MEM® I Reduced Serum Medium	Thermo Fisher Scientific	31985070
Polyethylenimine (PEI), Linear (MW 25,000)	VWR/Polysiciences	23966-2
PBS	Fisher Scientific	BP3994

16% Paraformaldehyde	Electron Microscopy Sciences	15710
Normal Donkey Serum	Jackson ImmunoResearch	017-000-121
Immun-Blot Low Fluorescence PVDF membrane	Bio-Rad	1620264
Methanol	Sigma-Aldrich	322415
Sodium Dodecyl Sulfate	Thermo Scientific	28364
Fluoromount G	SouthernBiotech	0100-01
Hoechst 33258	Invitrogen	H21491
Isothesia: Isoflurane	Henry Schein	11695-6776
Tissue Freezing Medium	VWR	15148-031
2-methylbutane	VWR	JtQ223-8
Trizma(R) base	Sigma-Aldrich	T1503-250G
GLYCINE	Sigma-Aldrich	G8898-1KG
Ammonium Persulfate (APS)	Thermo Fisher Scientific	17874
TEMED	Bio-Rad	161-0800
Precision Plus Protrein Dual Color Standards	Bio-Rad	1610374
Acrylamide/Bis solution	Bio-Rad	161-0158
4x Laemmli Sample Buffer	Bio-Rad	1610747
Immun-Blot® Low Fluorescence PVDF membrane	Bio-Rad	1620264
0.05% Trypsin-EDTA	Thermo Fisher Scientific	25300054
Odyssey Blocking Buffer	Li-Cor Biosciences	927-40000
Dynabeads® Protein G for Immunoprecipitation	Thermo Fisher Scientific	10003D
Sodium chloride,SigmaUltra, >=99.5%	Sigma-Aldrich	S7653-1KG
10% NP-40 solution	Thermo Scientific	28324
cOmplete™, Mini, EDTA-free Protease Inhibitor Cocktail Tablets	Roche	04693159001
Whatman® gel blotting paper, Grade GB003	Thermo Fisher Scientific	10426890
Ames	Sigma-Aldrich	A1420
Sodium Bicarbonate	Sigma-Aldrich	S5761

Carbogen	Airgas	Z020x9512000000
Critical Commercial Assays		
Bio-Rad DC Protein Assay Kit	Bio-Rad	5000112
Deposited Data		
Experimental Models: Organisms/Strains		
Mouse: Megf10^{LacZ}	Kay et al., 2012	*Megf10$^{tm1b(KOMP)Jrs}$*
Mouse: Megf10^{flox}	this study	*Megf10^{tm1c}*
Mouse: Ptf1a^{cko}	Krah et al., 2015	*Ptf1a^{tm3Cvw}*
Mouse: Isl1^{Cre}	Jax 024242	*Isl1$^{tm1(cre)Sev/J}$*
Mouse: Hb9:GFP	Jax 005029	*B6.Cg-Tg(Hlxb9-GFP)1Tmj/J*
Mouse: ChAT^{Cre}	Jax 006410	*Chat$^{tm2(cre)Lowl}$*
Mouse: Six3:Cre	Jax 019755	*Tg(Six3-cre)69Frty*
Mouse: Kcng4^{Cre}	Jax 029414	*Kcng4$^{tm1.1(cre)Jrs}$*
Mouse: Drd4:GFP	Huberman et al., 2009	*Tg(Drd4-EGFP)W18Gsat*
Mouse: Gjd2:GFP	RRID:MMRRC_030611-UCD	*Tg(Gjd2-EGFP)JM16Gsat/Mmucd*
Mouse: Rosa26^{mTmG}	Jax 007676	*Gt(ROSA)26Sor$^{tm4(ACTB-tdTomato,-EGFP)Luo}$*
Mouse: Rosa26^{fGFP}	Rawlins et al., 2009	*Gt(ROSA)26Sor$^{tm1(CAG-EGFP)Blh}$*
Mouse: Ai14	Jax 007914	*B6.Cg-Gt(ROSA)26Sor$^{tm14(CAG-tdTomato)Hze/J}$*
Mouse: ACTB:FLPe B6;SJL	Jax 003800	B6;SJL-Tg(ACTFLPe)9205Dym/J
Mouse: C57Bl6/J	Jax 000664	C57BL/6J
Experimental Models: Cell Lines		
Human: Hek293T	ATCC	293T (ATCC® CRL-3216™)
Oligonucleotides		
M10flagNotI_Rev	ATAGCGGCCGCttaCTTGTCGTCATCGTCTTTGT	

	AGTCttcactgctgctgctgctg	
M10flag_Fwd	GGTACATGCCTGT GCGAAGCA	
Cyto9_flag_Rev1	5'ATAGCGGCCGCttaCTTGTCGTCATCGTCTTT GTAGTC TTCCTTCCTCTTCTGCTTGTGT	

Recombinant DNA

CMV-M10-FLAG	this paper	
CMV-M10-GFP	Kay et al., 2012	
pCMV-MEGF10-ΔICD-GFP	Kay et al., 2012	
MEGF10-ΔICD-Flag	this paper	
pAAV-EF1a-Brainbow-tagBFP-EYFP-WPRE	Addgene	45185
pAAV-EF1a-Brainbow-mTFP1-Cherry-WPRE	Addgene	45816

Software and Algorithms

Fiji/ImageJ	Schindelin et al., 2012	
SnapGene	SnapGene	
NIS Elements	Nikon Instruments	
Custom JAVA scripts for spike sorting	Oracle	
Matlab	Mathworks, Natick, MA	
Image Studio™	LI-COR Biosciences	
Photoshop	Adobe	

Other

Olympus FV 300 Confocal Microscope	Olympus	
Nikon A1 Confocal Microscope	Nikon	
Micro HM550 Cryostat Microtom	Thermo Fisher Scientific	
LI-COR Odyssey	LI-COR Biosciences	
Nikon Digital Sight Qi1Me	Nikon Corporation	
Automatic Temperature Controller	Warner Instruments Corporation	TC-324B
MEA 519 electrode	Field et al., 2010	

Nikon Eclipse Ti inverted microscope	Nikon Instruments
OLED SVGA microdisplay	Emagin Inc.

872

873 **METHOD DETAILS**

874 **Animals**

875 All animal experiments were reviewed and approved by the Institutional Animal Care
876 and Use Committee of Duke University. The animals were maintained under a 12-hour light-
877 dark cycle with *ad lib* access to food and water. Retinas from adult (4-8 weeks old) *Megf10*$^{-/-}$
878 mutant mice and wild-type control mice with same genetic background were used for
879 experiments performed on the multielectrode array (MEA). Animals were dark-adapted
880 overnight prior to the experiment.

881 For this study the following transgenic and mutant mouse lines were used: 1)
882 *Megf10*$^{tm1b(KOMP)Jrs}$ (Kay et al., 2012), referred to as *Megf10*$^{-}$ or *Megf10*^{lacZ}; 2) *Ptf1a*^{tm3Cvw} (Krah
883 et al., 2015), referred to as *Ptf1a*^{flox} or (when crossed to Cre mice) *Ptf1a*^{cKO}; 3) *Isl1*$^{tm(cre)Sev}$ (Yang
884 et al., 2006), referred to as *Isl1*^{Cre}; 4) *Hb9:GFP* (Trenholm et al., 2011); 5) *Chat*$^{tm2(cre)Lowl}$ (Rossi
885 et al., 2011), referred to as *Chat*^{Cre}; 6) *Tg(Six3-cre)69Frty* (Furuta et al., 2000) referred to as
886 *Six3:Cre*; 7) *Kcng4*$^{tm1.1(cre)Jrs}$ (Duan et al., 2014) referred to as *Kcng4*^{Cre}; 8) *Tg(Drd4-*
887 *EGFP)W18Gsat* (Huberman et al., 2009), referred to as *Drd4:GFP*; 9) *Tg(Gjd2-*
888 *EGFP)JM16Gsat*, referred to as *Gjd2:GFP*. Two Cre reporter strains were used that express
889 membrane-targeted green fluorescent protein (mGFP) upon Cre recombination: 1)
890 *Gt(ROSA)26Sor*$^{tm4(ACTB-tdTomato,-EGFP)Luo}$, also known as *mT/mG* (Muzumdar et al., 2007); 2)
891 *Rosa26*^{fGFP} (Rawlins et al., 2009). An additional Cre reporter strain was used that expresses

892 tdTomato fluorescent protein upon Cre recombination: *Gt(ROSA)26Sor*$^{tm14(CAG-tdTomato)Hze}$
893 (Madisen et al., 2010). See Key Reagents table for repository stock numbers where applicable.

894 To produce *Megf10*^{flox} mice, *Megf10*$^{tm1a(KOMP)Jrs}$ mice (Kay et al., 2012) were crossed to
895 germline Cre strain *B6;SJL-Tg(ACTFLPe)9205Dym/J*, thereby generating a functional allele
896 (also known as *Megf10*^{tm1c}) in which exon 4 was flanked by loxP sites.

897 **Cell Culture**

898 HEK293T cells were obtained from ATCC. The cells were cultured in Dulbecco's
899 Modified Eagle's Medium (DMEM) with 10% bovine growth serum, 4.5 g/L D-glucose, 2.0 mM
900 L-glutamine, 1% Penicillin/Streptomycin in 10 cm cell culture dishes. Cells were passaged every
901 2-3 days to reach confluence. Before splitting, culture media were removed and Dulbecco's
902 phosphate-buffered saline (D-PBS) was used to rinse cell layers as well as removing residual
903 serum. Cells were detached from dish with 4 ml of 0.05% Trypsin and incubated at 37ºC until
904 cell layer is dispersed (about 5 minutes). Equal volume of complete culture media was added to
905 the dish to inhibit protease activity. The suspension was centrifuged at 200 x g for 5 minutes.
906 Supernatant was aspirated and the cells were suspended with appropriate amount of media and
907 plated (1:4-1:8). Cells used for experiments were passaged no more than 10 times. Cell stocks
908 were stored as 2 million cells per vial in complete culture media with 10% DMSO in liquid
909 nitrogen.

910 **Identification of DS circuit cell types using antibody and transgenic markers**

911 *SAC markers in mature retina*

912 Antibodies to choline acetyltransferase (ChAT) were used as a SAC marker in mice older
913 than P5. This antibody stains SAC somata and their dendrites in the IPL (e.g. Fig. 7A).

SAC markers in embryonic and neonatal retina

Antibodies to ChAT and vesicular acetylcholine transporter, typically used as SAC markers in the mature retina, do not stain reliably in the embryonic and neonatal (P0-P3) mouse retina, precluding their use as markers during one of the key time periods of this study. We therefore characterized several other SAC markers that we found to be suitable for definitive SAC identification and their anatomical characterization in the E16-P3 period:

The *Megf10*^{lacZ} allele (Kay et al., 2012) drives strong, selective β-galactosidase (βgal) expression in all SACs starting at embryonic day (E)17 (Fig. 1B; Fig. 1-Supplement 1; data not shown). Horizontal cells are also labeled. Expression is strong enough to allow characterization of SAC dendrite anatomy at these early stages. Antibodies to *Megf10* yield a similar staining pattern (Fig. 1-Supplement 1; Fig. 4B,C), but staining of fine dendritic arbors was brighter with anti-βgal staining of *Megf10*^{lacZ} mice, so this approach was used for most of our anatomical experiments analyzing the full SAC population at or before P3. In some such experiments a *Megf11*^{lacZ} allele (Kay et al., 2012) was also present; this allele drives βgal expression in essentially the same pattern as *Megf10*^{lacZ} and therefore contributed to signal brightness. The presence of this allele had no apparent effect on SAC anatomy, in either wild-type or *Megf10* mutant background.

Antibodies to Sox2 (Whitney et al., 2014) strongly label all SAC nuclei in the INL and GCL, starting at embryonic stages (Fig. 1-Supplement 1; Fig. 2D,E). Progenitor cells in the ONBL are also labeled. This marker was typically used in conjunction with *Megf10*^{lacZ} to provide definitive identification of SACs as βgal^{+}Sox2^{+} cells.

Antibodies to internexin label SAC intermediate filaments, which localize in a polarized manner to the primary dendrite(s) and the side of the cell body from which they emerge (Fig. 2-

Supplement 1). Primary dendrites were defined as any first-order dendrite branch, i.e. those arising directly from the cell body. Internexin is a selective marker of SAC in perinatal mouse retina, as previously shown in tree shrew (Knabe et al., 2007). RGC axons are also labeled (Fig. 2-Supplement 1).

Antibodies to Isl1 (Fig. 2A) label all SAC nuclei, starting at cell cycle exit (Galli-Resta et al., 1997). A large subset of RGCs are also labeled. The *Isl1*^{Cre} knock-in mouse (Yang et al., 2006) faithfully recapitulated this expression pattern (Fig. 2A,B) and was used to study SAC anatomy at embryonic stages (see below for further details).

SAC single-cell labeling

To assess the single-cell morphology of individual SACs during early postnatal development, the *Chat*^{Cre} line was used. In contrast to mature retina (e.g. Fig. 7B), in which all SACs were labeled, *Chat*^{Cre} expression was rare and sporadic in early postnatal retina (Fig. 1C; Fig. 1-Supplement 1), as reported previously (Xu et al., 2016). Therefore, when crossed with Cre reporter mice to make *Chat*^{mG} animals, the full anatomy of individual SACs was clearly delineated (e.g. Fig. 2I-L). We did not typically observe Cre recombination in non-SAC cell types; nevertheless, we always co-stained with another SAC marker, either Sox2 or *Megf10:*βgal, to confirm the SAC identity of the cells that were analyzed.

ooDSGC markers

Two mouse lines were used, each of which labels distinct types of ooDSGCs. *Hb9:GFP* labels the superior subtype of ooDSGC, while *Drd4:GFP* labels the posterior subtype of ooDSGC (Trenholm et al., 2011; Huberman et al., 2009).

DS-circuit bipolar cell markers

Four types of bipolar cells have been shown to make monosynaptic connections with SACs and/or ooDSGCs: Types BC2, BC3a, BC5, and BC7 (Duan et al., 2014; Ding et al., 2016; Greene et al., 2016; Kim et al., 2014; Chen et al., 2014). OFF bipolar cells BC2 and BC3a were labeled, respectively, by antibodies to Syt2 and HCN4 (Wässle et al., 2009). Syt2 also labeled the axon terminals of BC6 bipolar cells (Wässle et al., 2009).

ON bipolar cells BC5 and BC7 were marked with *Kcng4*^{Cre} (Duan et al., 2014) crossed to mGFP Cre reporter mice (denoted *Kcng4*^{mG}). Labeling of BC7 was more prominent with the Rosa26 locus mGFP Cre reporter line that we used, compared to the cytosolic GFP reporter driven by Thy1 that was used by Duan et al. (2014).

Gjd2-GFP was also used to label BC5 bipolar cells (Fig. 9-Supplement 1). In adult retina, GFP was strongly expressed by a bipolar cell type that ramified in a laminar location typical of BC5 (Sidney Kuo, University of Washington, personal communication). We confirmed this expression pattern; weak expression in amacrine cells was also noted (Fig. 9-Supplement 1). At earlier developmental stages the amacrine cell staining was much stronger and filled many amacrine processes throughout the IPL, precluding use of this line for developmental studies of bipolar axons (M. Stogsdill and J.N.K, unpublished observations).

Immunohistochemistry

Retinal cross sections:

Mice were anesthetized by isoflurane or cryoanesthesia (neonates only) followed by decapitation. Eyes were enucleated, washed in PBS, and fixed in PBS containing 4% formaldehyde (pH 7.5) for 1.5 hours at 4° C. After fixation, eyes were washed 3X with PBS and

stored in PBS containing 0.02% sodium azide at 4° C until further processing. Retinas were dissected from the eyecup, cryoprotected by equilibration in PBS containing 30% sucrose, then embedded in Tissue Freezing Medium and frozen by submersion in 2-methylbutane chilled by dry ice. Tissue sections were cut on a cryostat to 20 µm and mounted on Superfrost Plus slides. Slides were dried on a slide warmer for 1 h then stored at -80° C or used immediately.

For antibody labeling, slides were washed for 5 min with gentle agitation in PBS to remove embedding medium and blocked for 1 h in PBS + 0.3% Triton X-100 (PBS-Tx) containing 3-5% normal donkey serum. Primary antibodies were diluted in blocking buffer, added to slides, then incubated overnight at 4° C. Slides were washed with PBS 3X for 10 minutes followed by incubation with secondary antibody diluted in PBS-Tx for 1-2 h at RT. Slides were washed again with PBS 3X for 10 minutes then coverslipped using Fluoromount G.

Retinal whole-mounts:

Tissue was processed as above up to the point of dissection from the eyecup. After dissection from eyecup, retinas were washed in PBS then blocked for 3 hours with agitation at 4° C in blocking buffer (constituted as described above). Primary antibodies were diluted in blocking buffer, added to retinas, and incubated for 5-7 days with gentle agitation at 4°C. Retinas were washed 3X with PBS over the course of 2 hours with gentle agitation. Secondary antibody was diluted in PBS containing 0.3% Triton X-100 and was added to retinas followed by incubation overnight at 4° C with gentle agitation. Retinas were washed again 3X in PBS over the course of 2 hours with gentle agitation. For mounting on slides, 4 radial incisions separated by 90° were made centripetally, approximately 1/3 the radius of the retina. Retinas were flattened on nitrocellulose paper photoreceptor side down and coverslipped with Fluoromount G.

Image acquisition and processing

Sections and whole-mounts were imaged on a Nikon A1 or an Olympus FV300 confocal microscope. Image z-stacks were imported to Fiji (Schindelin et al., 2012), de-noised by median-filtering (0.5 - 2.0 pixel radius), and projected to a single plane. Color channels were assembled, and minor adjustments to brightness and contrast were made, in Adobe Photoshop. When images were to be compared, equivalent adjustments were performed on all images in the experiment.

Analysis of SAC anatomy in embryonic retina

To study SAC anatomy during embryonic stages, *Isl1*^{Cre} was crossed to *lox-stop-lox-mGFP* Cre reporter mice (*mT/mG* or *Rosa26*^{GFPf}; see Key Reagents) to generate *Isl1*^{mG} animals. Timed-pregnant dams were sacrificed at E16 and eyes collected from embryos (n = 11 mice from 3 litters). Tissue was processed as described for postnatal eyes, except fixation time was 60 min. Cross-sections were stained with anti-GFP to reveal the morphology of *Isl1*^{mG}-expressing neurons, as well as Sox2 to distinguish *Isl1*^{mG}-positive SACs from RGCs. (All cells shown in Fig. 2B-G were confirmed to be SACs by Sox2 co-labeling.) In combination with these markers, anti-internexin staining was used to assess orientation of primary dendrites. Location and/or presence of the IPL was determined using Hoechst nuclear staining, which revealed cell body-free neuropil regions, and/or by *Isl1*^{mG} labeling of neuronal processes, which filled these neuropil regions (Fig. 2-Supplement 2). We assessed anatomy of mGFP^{+} migrating SACs in the ONBL, as well as SACs in the INBL that were concluding their migration. Morphology of ON SACs in the GCL could not be discerned due to *Isl1* expression by RGCs (Fig. 2A,B), but because displaced amacrine cells pause at the INL-IPL border before crossing to the GCL (Chow et al., 2015), the population of cells available to analyze might have included both ON and OFF SACs.

Characterization of SAC homotypic arbor network in soma layers

The homotypic nature of SAC soma-layer contacts was investigated by imaging single *Chat*^{mG}-labeled OFF SACs in mice also carrying a single copy of the *Megf10*^{lacZ} allele (Fig. 2I,J). Anti-βgal staining was used to reveal the full SAC population, including arbors. *En-face* images were captured in z-stacks spanning the INL and IPL; slices corresponding to each layer were separately z-projected. For the INL arbor of each *Chat*^{mG}-labeled cell, we examined the termination site of each dendritic tip. The fraction of dendrites terminating on the βgal-positive soma or arbor of a neighboring SAC was quantified. Sample sizes are given in main text.

Generation and analysis of "solitary" SACs

Reduction of SAC density using Ptf1a^{flox} *mice*

Ptf1a^{flox} mutant mice (Krah et al., 2015) were crossed into the *Six3:Cre* background to generate *Ptf1a*^{cKO} mice. *Six3:Cre* is expressed by retinal progenitors starting at E9.5 in a high-central-to-low-peripheral gradient (Furuta et al., 2000; Fig. 3A). In central retina, where Cre is expressed in all progenitors, amacrine cells were completely absent but bipolar cells, RGCs, Müller glia, and photoreceptors remained (Fig. 3B; Fig. 3-Supplement 1; data not shown). In peripheral retina, where Cre recombination was incomplete, amacrine cells derived only from Cre-negative progenitors (Fig. 3C). Because the number of Cre-expressing progenitors in peripheral retina still vastly exceeded the number that escaped Cre, amacrine cell density in *Ptf1a*^{cKO} peripheral retina was markedly reduced compared to littermate controls (Fig. 3A,B; Fig. 3-Supplement 1).

Quantification of dendrite phenotypes in solitary and touching SACs

To visualize SACs and quantify their arbor targeting frequencies in *Ptf1a*^{cKO} mice, we bred *Megf10*^{lacZ} into the *Ptf1a*^{flox} background. All *Ptf1a*^{cKO} and littermate control mice in these experiments carried one copy of the *Megf10*^{lacZ} allele. SAC morphology was revealed with anti-βgal. Sox2 was used to confirm the SAC identity of all cells included in the experiment. SACs were scored as "solitary" or "touching" based on whether their dendrites contacted neighboring SACs in the same or adjacent sections. If this could not be determined (e.g. because the adjacent section was missing or damaged), the cell was excluded from further analysis. Because SACs were only present in *Ptf1a*^{cKO} peripheral retina, analysis of littermate control SACs was also limited to peripheral retina. In *Ptf1a*^{cKO} mice, SACs were more frequently found in the INL than the GCL and it is possible that the INL SACs were a mixed population of ONs and OFFs. Therefore, we did not distinguish between SAC subtypes for the analyses.

IPL projections of βgal-stained cells were examined, and cells were assigned to one of three categories: 1) no arbors projecting to the IPL; 2) Arbors enter the IPL but fail to stratify; 3) Arbors enter the IPL and ramify in a laminar pattern. Examples of the first category of solitary SACs are shown in Fig. 3F, left, and Fig. 3-Supplement 1. Examples of the second category are shown in Fig. 3F, right, and Fig. 3-Supplement 1. The third category is exemplified by all touching SACs shown (Fig. 3E; Fig. 3-Supplement 1). Each cell in the dataset was also scored on an independent criterion: whether it projected to the soma layer (e.g. Fig. 3D,F, white arrows).

For each animal in the experiment, the following was calculated and plotted in Fig. 3G: 1) Percentage of SACs with projections to the soma layers; 2) percentage of SACs projecting to the IPL (i.e., the cells assigned to categories 2 and 3 above); 3) percentage of SACs with stratified IPL dendrites (i.e. the cells in category 3). Sample sizes: $n = 3$ wild-type littermates

(28, 62, 32 cells analyzed in each animal); *n = 4 Ptf1a*^{cKO} animals (11, 35, 13, 12 solitary and 27, 44, 22, 23 touching SACs analyzed in each animal). Statistics: one-way ANOVA with Tukey's post-hoc test.

Quantification of SAC projection phenotypes in *Chat*^{mG} mice

Single SACs labeled in *Chat*^{mG} and *Chat*^{mG}*;Megf10*$^{-/-}$ mice were morphologically assessed in cross-sections. GFP signal was amplified with anti-GFP antibody staining. All GFP^{+} SACs on any given slide were imaged and analyzed, to avoid cell selection bias, with the exceptions of: 1) cells severed by the sectioning process; 2) cells with arbors that could not clearly be distinguished from those of their neighbors; 3) cells in the far retinal periphery, where sections were oblique to retinal layers, obscuring IPL strata. In experiments analyzing *Megf10* mutants, littermates were always used as controls to avoid complications arising from the fact that the precise state of retinal development at the time of birth might vary from litter to litter.

A cell was scored as innervating the IPL if it ramified branched dendrites within the neuropil. Dendrites that entered the neuropil but did not branch or stratify (e.g. Fig. 5E) were not sufficient. A cell was scored as projecting to the soma layer if arbors emanating from the cell soma or primary dendrite terminated or arborized in the INL (for OFF SACs) or GCL (for ON SACs). The arbor was required to be $\sim \geq 1$ cell diameter in length (i.e. small fine arbors were not counted). One other important exception that was not counted: We observed that many SACs at young ages had single unbranched arbors extending ~180˚ away from the IPL (e.g. Fig. 2K,L – all four cells have such arbors, even the ones that do not project towards neighboring SAC somata). These processes were not counted for two reasons. First, their trajectory was such that they were unlikely to join the soma-layer dendrite network or contact neighboring somata. Second, these 180˚ arbors were sometimes still present in P5 SACs (Fig. 2-Supplement 2) and

1090 therefore they did not appear to be subject to the same developmental regulation as soma-
1091 directed arbors (Fig. 2M). This observation suggests they are fundamentally different, and likely
1092 serve a different (as yet uncharacterized) purpose. No obvious difference in their frequency was
1093 observed between wild-type and *Megf10* mutants.

1094 To produce graphs in Figs. 2M, 5F, and 7G, the fraction of cells making ectopic
1095 projections – either to the soma layer or to inappropriate IPL sublayers – was calculated for each
1096 genotype and each time point. To determine whether a GFP+ IPL arbor was located in normal or
1097 abnormal IPL strata, *Megf10:*βgal was used as a counterstain. $Chat^{Cre}$ was rarely expressed in
1098 OFF SACs at P0, making it difficult to obtain large sample sizes at this age. For this reason, and
1099 because soma-layer projection frequency did not appear to differ much between P0 and P1, the
1100 data from each time point was pooled for analysis of *Megf10* litters.

1101 Sample sizes for Fig. 2M: P0, n =25 OFF, 63 ON; P1, n = 51 OFF, 79 ON; P2, n = 46
1102 OFF, 55 ON; P3, n = 33 OFF, 49 ON; P5, n = 15 OFF, 26 ON; P7, n = 23 OFF, 34 ON. Data
1103 were from four litters of mice, each of which was assessed at no less than two of these time
1104 points.

1105 Sample sizes for *Megf10;* $Chat^{mG}$ experiments (Figs. 5F, 7G): *Megf10* heterozygous
1106 littermate controls: P0/1, n = 11 OFF, 25 ON; P2, n = 25 OFF, 23 ON; P3, n = 17 OFF, 22, ON;
1107 P5, n = 16 OFF, 16 ON. *Megf10* mutants: P0/1, n = 6 OFF, 25 ON; P2, n = 14 OFF, 20 ON; P3,
1108 n = 34 OFF, 41 ON; P5, n = 48 OFF, 54 ON. Data were from two litters of mice.

1109 For the adult data reported in Fig. 7G, a different procedure was used; see "Quantification
1110 of Mosaic Spacing Phenotypes" section below.

Analysis of *Chat-Megf10^{cKO}* conditional mutants

Characterization of timing of MEGF10 deletion

For initial characterization of when MEGF10 protein is eliminated by the *Chat^{Cre}* driver line, the following experiment was performed: *Chat^{Cre}; Megf10^{flox}* mice were intercrossed with *Chat^{Cre}; Megf10^{lacZ}* carriers to generate *Chat^{Cre}; Megf10$^{flox/lacZ}$* (*Chat-Megf10^{cKO}*) experimental animals and littermate controls (*Chat^{Cre}; Megf10$^{flox/+}$*). These animals also carried a *Rosa26* mGFP Cre reporter allele. Animals were sacrificed at P1, P3, and P5; retinas were cross-sectioned and immunostained for anti-MEGF10 (Fig. 6-Supplement 1). Comparisons were made across animals from the same litter to assess how MEGF10 immunoreactivity changed over time. Two litters were analyzed in this way, each yielding the same conclusion: MEGF10 immunoreactivity was largely eliminated by P5 in *Chat-Megf10^{cKO}* mice (Fig. 6-Supplement 1). At P3, overall MEGF10 levels were reduced, but most SACs still expressed detectable protein (Fig. 6-Supplement 1). The cells that lost MEGF10 immunoreactivity by P3 were not necessarily the same cells that recombined the mGFP reporter at the *Rosa26* locus (Fig. 6F,G). At P1, only a very small number of cells (< 5 per retina) could be identified that lacked MEGF10 immunoreactivity; most of these were ON SACs although a few recombined OFF SACs were identified (Fig. 6G). We conclude that a small fraction of SACs loses MEGF10 protein prior to P3, while the majority lose MEGF10 between P3 and P5. Further, ON SACs are somewhat more likely to lose MEGF10 before P3 than OFF SACs.

Assessment of morphological and IPL projection phenotypes

To ask if loss of MEGF10 prior to P3 affects dendritic targeting, *Chat^{mG}*-labeled single SACs were identified in retinal cross-sections from *Chat-Megf10^{cKO}* and *Chat^{Cre}; Megf10$^{flox/+}$*

control mice, as described above. Analysis was performed at P1 and P3; data in Fig. 6H is from P3 only. All mGFP^{+} SACs were first scored as to whether they expressed MEGF10 protein (see Fig. 6F,G). Subsequently, each cell was scored for soma-layer projection as described above for wild-type and *Megf10*$^{-/-}$ animals. This scoring was done blind to the cell's MEGF10 expression status. The fraction of cells classified as either "soma-projecting" or "IPL-only" was calculated for MEGF10^{+} SACs, MEGF10^{-} SACs, and littermate control SACs (Fig. 6H). Sample sizes: n = 26 OFF, 18 ON cells from controls; 24 OFF, 19 ON MEGF10^{+} cells from *Chat-Megf10*^{cKO}; 9 OFF, 17 ON MEGF10^{-} cells from *Chat-Megf10*^{cKO}.

To assess SAC stratification at maturity, cross-sections from P17 *Chat-Megf10*^{cKO} and littermate controls were stained for anti-ChAT. Four mutants and three littermate controls, from two litters, were examined.

Analysis of *Six3-Megf10*^{cKO} conditional mutants

Characterization of Cre recombination patterns

Breeders carrying the relevant alleles were interbred to generate *Six3:Cre; Megf10*$^{flox/lacZ}$ (*Six3-Megf10*^{cKO}) mice and littermate controls (*Six3:Cre; Megf10*$^{+/lacZ}$ or *Cre*$^{-}$ *Megf10*$^{flox/lacZ}$). As noted above in *Ptf1a* section, Cre is expressed very early (~E9.5) in *Six3:Cre* retina, but expression is incomplete, with some parts of peripheral retina spared from Cre activity (Furuta et al., 2000). Therefore, all mice used for these experiments also carried the *Rosa26*^{GFPf} Cre reporter, to reveal retinal regions that either lacked MEGF10 (GFP^{+} cells) or were spared from MEGF10 deletion (GFP^{-} cells). Anti-MEGF10 staining confirmed that the GFP Cre reporter is a reliable marker of MEGF10 expression status (Fig. 6-Supplement 1).

Assessment of morphological phenotypes

For quantification of INL projection frequency at P2, *Six3-Megf10*^{cKO} and littermate control whole-mount retinas were stained for βgal, Sox2, and anti-GFP. This staining marked SACs (Sox2 and βgal), revealed their dendritic morphology (βgal), and defined their MEGF10 expression status (GFP). Confocal stacks were acquired through the INL, extending to the IPL (which was clearly discernable due to dense βgal and GFP expression). The INL was defined as the region above this in the image stack, containing Sox2^{+} neurons. Cells that projected soma-directed arbors into the INL were clearly discernable due to their multipolar morphology with numerous dendritic protrusions (e.g. Fig. 6B). Cells that did not project to the INL had a round morphology with only minor lateral branches less than one cell radius in length (Fig. 6C). Each βgal-labeled SAC was scored as to whether it expressed GFP, and whether it projected lateral arbors into the INL. If the cell had only INL branches directed towards the IPL through the stack Z-plane, it was not counted as INL-projecting. Scoring was done in separate sessions so that the scorer was blind to GFP expression status when determining INL projections. Sample sizes: n = 117 SACs from 2 control mice; n = 302 GFP^{+} SACs and 149 GFP– SACs from 2 *Six3-Megf10*^{cKO} mice.

To assess SAC stratification in cross-sections, P2, P4, or P17 *Six3-Megf10*^{cKO} and littermate control retinas were sectioned and stained for anti-βgal (P2) or anti-ChAT (P17). The number of animals examined was: P2, 4 mutants, 2 controls; P4, 2 mutants, 3 controls; P17, 2 mutants, 2 controls.

Quantification of area covered by SAC dendritic arbors

Embryonic SAC arbor territory

P0 *Chat*^{mG} retinas were imaged in whole-mount preparations stained with anti-Sox2 and anti-GFP antibodies to identify single GFP^{+} SACs. To avoid cell selection biases, all labeled SACs with arbors that were clearly distinguishable from their neighbors were imaged and analyzed, except for far-peripheral cells that may have been damaged during mounting. Z stacks were acquired through the GCL, IPL, and INL to encompass all arbors of a single cell. Images were imported into ImageJ, z-projected into a single plane, and polygons were drawn connecting the dendritic tips, nearest neighbor to nearest neighbor, until the dendritic field was captured. Area of this polygon was calculated using ImageJ. Sample sizes: OFF SACs, n = 16 wild-type and 16 *Megf10*$^{-/-}$; ON SACs, n = 31 wild-type and 34 *Megf10*$^{-/-}$. Statistics: two-tailed t-tests.

Adult SAC arbor territory

Individual SACs were labeled by injection of *Chat*^{Cre} mice with "Brainbow" Adeno-associated virus (AAV) driving fluorophore expression in a Cre-dependent manner (Cai et al., 2013). The two Brainbow AAV9 viruses, encoding farnesylated fluorescent proteins that are targeted to the plasma membrane (University of Pennsylvania Vector Core), were mixed to 1.5 x 10^{12} genome copies per mL. Adult mice (P40-50) were anesthetized with ketamine-xylazine by intraperitoneal injection. Propraracaine hydrochloride (0.5%) ophthalmic solution (Akorn, Lake Forest, IL) was applied to the eye to provide local anesthesia. A 30 1/2G needle was used to make a small opening near the ora serrata, and 1µl of virus was injected with a 33G blunt-ended Hamilton syringe intravitreally. Tissue was collected 3 weeks after the virus injection.

Retinas were stained in whole-mount with anti-GFP, anti-mCherry, and anti-mKate antibodies to reveal SACs. OFF SACs were not labeled in large numbers, so analysis was restricted to more abundantly labeled ON SACs. Imaging, image processing, and quantification were as for P0, except that only SACs in central and mid-peripheral retina were used to avoid confounding effects of eccentricity on arbor size. Sample sizes: n = 10 wild-type and 16 *Megf10* mutant SACs.

Hb9-GFP stratification

P1-P2 retinas carrying *Megf10*^{lacZ} and *Hb9-GFP* were co-stained for βgal and GFP. RGCs with dendrites that co-fasciculated with βgal-positive IPL strata were counted. See Results for sample sizes.

Quantitative assessment of IPL stratification level

Images of retinal cross sections were processed in ImageJ. A vertical ROI (12.5 μm wide) was drawn to perpendicularly bisect the IPL strata, from the edge of the INL to the edge of the GCL. IPL stratification levels were reported as percentage of IPL width. Intensity was calculated for each pixel along the length of the ROI as an average across its width. Then all pixel intensity values were normalized to the maximum value of that ROI. Location of fluorescent peaks was calculated as the pixel with maximum intensity; if multiple pixels had the same intensity the peak was defined as the center of the plateau.

For BC5-BC7 arbor distance measurements (Fig. 9F), distances as percentage of total IPL width were compared by one-way ANOVA/Tukey's post-hoc test. n = 14 measurements from 2 control mice; n = 7 normal IPLs, 11 SAC clumps, 11 SAC gaps from 3 *Megf10*$^{-/-}$ mice.

Generation of Megf10-ΔICD Constructs

The MEGF10-ΔICD-GFP construct was reported previously (Kay et al., 2012), which was originally made from pUbC-MEGF10-GFP (Addgene #40207). It encodes a version of MEGF10 in which the cytoplasmic domain is truncated after the 9th amino acid and replaced by GFP. Inclusion of those 9 amino acids was necessary to achieve plasma membrane localization. For this study it was subcloned into the pEGFPN3 plasmid, containing the CMV promoter, to make pCMV-MEGF10-ΔICD-GFP.

To make the MEGF10-ΔICD-Flag construct, Megf10 (truncated after the 9th intracellular domain amino acid as above) was PCR amplified from pUbC-MEGF10-GFP vector using M10flag_Fwd forward primer and Cyto9_flag_Rev1 reverse primer. Resulting PCR products were digested with NotI and AscI restriction enzymes and ligation cloned into pEGFPN3 vector linearized with corresponding restriction enzymes.

Assay for interaction of MEGF10-ΔICD constructs

Co-Immunoprecipitation

HEK293T cells were grown to 80% confluency. Cells were then transfected using a linear polyethylenimine (PEI) transfection reagent: DNA, PEI, and Opti-MEM were mixed in a 1:3:30 ratio and incubated for 10 minutes at room temperature then applied to confluent cells. Cells were harvested 48-hour post transfection. Cells were lysed with NP-40 lysis buffer (1% NP-40, 150mM NaCl, 50mM Tris-Cl, and 1X proteinase inhibitor) by pipetting. Lysate was centrifuged at 14000 x g at 4ºC for 15 min. to remove insoluble material. The soluble protein fraction was quantified with Bio-Rad DC assay. For immunoprecipitation, 500µl (1µg/ µl) protein in NP-40 buffer lysis buffer was incubated overnight at 4ºC with antibody (1µl of

chicken anti-GFP or 2µl of mouse anti-Flag). Protein G Dynabeads (10µl) were added to mixture for 1 hour at 4ºC while rotating. Beads were sequestered by magnet and flow-through was removed. Beads were washed with 500µl lysis buffer (3x) on ice then eluted with 30µl 2X Laemmli containing 5% β-mercaptoethanol.

Western Blot

Samples were prepared in 2X Laemmli sample buffer, heated at 95°C for 10 minutes, and loaded onto SDS-acrylamide gel (running gel: 8% acrylamide/bis Tris-HCl with 0.1% SDS pH 8.8; stacking gel: 5% acrylamide pH 6.8; cross linked with TEMED and APS). Precision Plus Protein Dual Color Standards (BioRad) were used as a molecular weight marker. The gel was run on a BioRad mini gel running apparatus with SDS-PAGE running buffer (25 mM Tris, 192 mM glycine, 0.1% SDS). Electrophoresis was carried out at 50 V through the stacking gel then adjusted to 120 V until the dye front reached the lower end of the gel. BioRad Immobilon-FL PVDF membrane and Whatman filter paper were used with the BioRad mini cassette for transfer. Samples were transferred in 25 mM Tris, 192 mM glycine, 20% methanol at 100 V for 90 minutes. Membranes were blocked with PBS/Odyssey blocking buffer and stained with chicken anti-GFP 1:20000, mouse anti FLAG 1:20000 overnight at 4°C with shaking. After washing with PBST for 4 times, membranes were stained with 1:20000 secondary antibodies for one hour at room temperature. The membranes were washed with PBST four times and then rinsed with PBS and water. Finally, the membranes were imaged with LI-COR Odyssey using the Image Studio software.

Quantification of mosaic spacing phenotypes and their effects on SAC IPL projections

Regularity index

Regularity of SAC cell body distribution in *Six3-Megf10*^{cKO}, *Chat-Megf10*^{cKO}, and littermate control mice was calculated as previously described (Kay et al., 2012). The Voronoi domain regularity index (VDRI) was used as a measure of regularity. It is calculated by first assigning a Voronoi domain to each cell in an array (Fig. 8C), and then calculating the mean and standard deviation of the domain areas. The VDRI is defined as the mean area divided by the standard deviation. Arrays that are less regularly distributed will have a lower VDRI because their domain sizes are more variable (and hence have a higher standard deviation).

P17 whole-mount retinas were stained with an antibody to ChAT and imaged *en face*. One eye was processed from each animal used in the experiment. For each eye, 3 confocal image stacks were obtained using a 20x objective (636.5 μm^2 field of view). Images of INL SACs were analyzed using Fiji software. The location of each SAC in the field of view was marked; this information was used to count the number of SACs (Fig. 8-Supplement 1) as well as define Voronoi domains belonging to each cell, using Fiji functions. The area of each Voronoi domain (excluding edges) was calculated in Fiji.

For statistical analysis of regularity effects across genotypes, we first calculated the per-animal average cell density and VDRI from the 3 acquired images. Differences between genotypes were then evaluated using one-way ANOVA and Fisher's PLSD. Previously published *Megf10* null and simulation data was also included for comparison (Kay et al., 2012). The simulations define the VDRI that would be expected for a randomly-arranged array of cells matched in size and density to real SACs. Data collection and analysis was virtually the same as in the previous study, allowing us to include these data in our statistical comparisons.

Effects of soma position upon IPL errors: Single-cell analysis

To ask if soma position correlates with IPL errors, we first defined the ectopic projection status of each OFF SAC in a set of z-stacks acquired from ChAT-immunostained retinal whole-mounts. Sample sizes: n = 515 cells from 2 control (*Megf10*$^{+/-}$) mice; n = 584 cells from 2 *Megf10* mutant mice. The z-stacks encompassed, at different levels of the stack, SAC somata in the INL and their ramified arbors in the IPL. In *Megf10* mutants, the OFF ectopic IPL arbor network and the typical OFF DS circuit sublayer were identified at different stack levels (Fig. 7C,E). ChAT^{+} arbors arising from individual OFF SAC somata were traced through the stack to identify those that joined into the ectopic network. The fraction of SACs that did so was then calculated and plotted in Fig. 7G. For Fig. 7H, we further examined these stacks to look for SACs that made ectopic projections at the INL level.

Next, we defined the severity of mosaic spacing perturbations in the local neighborhood of each SAC. Because SAC position is random in *Megf10* mutants, SACs might be more crowded or more isolated from their neighbors than in controls; or, by chance, they might be located at a fairly normal distance from their neighbors. The size of a cell's Voronoi domain is influenced by the distance of all nearest neighbors (Fig. 8C), and therefore serves as a convenient measure of local cell density. For simplicity we refer to Voronoi domains as "territory size" in Fig. 8. The effect of local cell density upon IPL projection errors was determined by plotting the ectopic error rate for each 100 μm^2 territory size bin (Fig. 8D,F). Sample size per bin, in order from smallest (<200 μm^2) to largest (>1100 μm^2): n = 32, 65, 89, 102, 91, 80, 30, 39, 24, 34.

Soma-arbor cross-correlation analysis

From the same z-stacks used for the above analysis, we made sub-stack z-projections capturing the OFF SAC soma array and the OFF SAC IPL sublayer. Prior to calculating the

correlations between these images, the following pre-processing steps were performed in Fiji: 1) Images were converted to 32-bit space. 2) To remove spurious correlations arising from vignetting, the images were flat-field corrected by low-pass filtering. 3) The pixel values in each image were normalized to an equivalent scale by subtracting the image mean value and dividing by the standard deviation. 4) Flipped images of the IPL arbors were generated by reflecting the image about both vertical and horizontal axes. On completion of these steps, cross-correlations between the soma image and the real or flipped arbor images were performed using the FD Math Fiji function. The Radial Profile Plot ImageJ plugin was used to quantify correlation intensities. To control for correlations unrelated to the specific locations of arbors and cell bodies, the intensity values at each radius were determined by subtracting the control (flipped image) value from the experimental (unflipped) value.

Multielectrode array recordings

Isolation of retina, recording, and spike sorting

Two wild-type and two *Megf10*$^{-/-}$ animals were used for multielectrode array (MEA) recordings. Immediately following euthanasia, retinas were isolated under infrared (IR, >900 nm) illumination with the assistance of IR-to-visual converters. This preserved the photosensitivity of the retina during the dissection. Dissections were performed in sodium bicarbonate-buffered Ames' solution (Sigma, St. Louis, MO) equilibrated with 5% CO_2 + 95% O_2 to pH 7.4 and maintained at 32-34° C. Hemisection of the eye was performed along the ora serrata by first making a small incision, following which the vitreous was removed and the retina was isolated from the pigment epithelium and eye cup. A piece of dorsal retina (1-2 mm^2) was dissected and placed RGC-side down on the planar MEA.

The MEA consisted of 519 electrodes with 30 μm inter-electrode spacing, covering a hexagonal region with 450 μm on a side (Field et al., 2010). The voltage on each electrode was digitized at 20 kHz and stored for post-hoc analysis. Details of recording methods and spike sorting have been described previously (Field et al., 2007). Spikes were identified using a threshold of four times the voltage standard deviation on each electrode. Principal component analysis applied to the ensemble of spike waveforms measured on each electrode provided a subspace for clustering spikes according to their shape. A Gaussian mixture model was used to cluster the spikes originating from individual RGCs. The clusters were manually inspected for each identified ooDSGC to ensure the spike waveforms were well isolated from other simultaneously recorded RGCs and all spikes were captured within each cluster. When a single cluster of spikes was captured by more than one Gaussian or when a single Gaussian included spikes from more than one cluster, the clustering was manually adjusted to generate a new set of initial conditions for re-fitting the mixture of Gaussians. Spike clusters with >10% estimated contamination based on refractory period violations, or spike rates <1 Hz, were excluded from further analysis.

Visual stimulation and RGC responses

Visual stimuli were focused on the photoreceptor outer segment, from an OLED display (Emagin, Inc.) with 60.35 Hz refresh rate. The mean intensity of the stimulus was 7000 photoisomerizations per rod per s, or 5000 photoisomerizations per cone per s for a cone containing all M-opsin. These estimates do not account for the effect of pigment self-screening. To measure the direction tuning of ooDSGCs as a function of contrast, a positive contrast bar (1200 μm wide) was presented on a gray background (Fig. 10B). On each presentation, the bar moved in one of twelve equally spaced directions at 400 μm/sec and was presented at one of the

following (Weber) contrasts: 5%, 10%, 20%, 40%, 80%, 150% and 300%. Responses to a total of 8 trials were collected for every condition; stimulus conditions were presented pseudo randomly. Spike times were binned at 1 ms resolution for all subsequent analyses.

To distinguish DSGCs from other RGCs recorded on the MEA, square-wave drifting gratings were used. These gratings drifted in one of twelve different and equally spaced directions and at two different speeds (225 μm/sec and 900 μm/sec; spatial period 400μm/cycle). DSGCs were identified based on their direction selectivity index (DSI) defined as:

$$DSI = \frac{|\sum \vec{v}_i|}{\sum n_i}$$

calculated from responses to drifting gratings and moving bars. Here, n_i is the number of spikes elicited to stimulus movement along the direction i defined by the vector $\vec{v}_i$.

The distribution of DSIs across all recorded RGCs was bimodal, with DSGCs forming the high mode (Fig. 10A). Based on these distributions, a DSI of 0.25 reliably identified DSGCs in wild-type and *Megf10*$^{-/-}$ retinas. ooDSGCs were isolated from ON DSGCs by their distinct ON and OFF responses to a bar entering and exiting the receptive field (Fig. 10B). The total ooDSGC sample size obtained by this procedure was $n = 80$ from the two wild-type and $n = 74$ from the two *Megf10*$^{-/-}$ retinas. The paired Kolmogorov-Smirnov (KS) test was used to compare cumulative probability distributions from these two populations.

Analysis of ooDSGC response

Measurement of direction tuning width

First, the direction tuning curve for each ooDSGC was obtained by calculating the number of spikes elicited across all trials for each direction of bar movement. Due to the circular

nature of the data, the direction tuning curve was treated as circular normal distribution, also called von Mises distribution (Oesch et al., 2005), and the tuning width was measured as the circular standard deviation (σ_{circ}), defined by

$$\sigma_{circ} = \sqrt{-2\ln(R)}$$

where R is the second moment of the von Mises distribution:

$$f(\theta, \mu) = \frac{1}{2\pi I_0(\kappa)} e^{\kappa \cos(\theta - \mu)}$$

This yielded a nonparametric estimate of the tuning curve width.

Measurement of direction tuning strength

To measure the strength of tuning, the difference between spike counts to motion in the preferred and null directions was normalized by the sum of these responses. The tuning curves were sampled at 30 degree intervals. To estimate the response in the preferred (null) direction, which could fall between sampled directions, a cosine-weighted average of the two strongest (weakest) responses was calculated. This yielded the following equation for measuring tuning strength:

$$\text{Tuning strength} = \frac{\sum_{i=1}^{2} r_i \cos(|\theta_{PD} - \theta_i|) - \sum_{j=1}^{2} r_j \cos(|\theta_{ND} - \theta_j|)}{\sum_{i=1}^{2} r_i \cos(|\theta_{PD} - \theta_i|) + \sum_{j=1}^{2} r_j \cos(|\theta_{ND} - \theta_j|)}$$

where the summation $\sum_{i=1}^{2}$ is performed over the responses r_i weighted by the cosine terms for the two nearest neighbor movement directions θ_i around the preferred direction θ_{PD} and the null direction θ_{ND}. This resulting index for tuning strength varied between zero and unity.

Measurement of direction tuning similarity between ON and OFF responses

To separately analyze the ON and OFF responses of ooDSGCs, we first defined temporal windows for each ooDSGC that distinctly separate the ON and OFF responses. This was done by passing high-contrast moving bars (150% and 300% contrast) through the receptive field. In the resulting spike rasters, ON and OFF response phases were clearly discernible (Fig. 10B,F). The boundary for separating the ON and OFF responses was set halfway between the peak ON and OFF spike rate locations (Fig. 10F,G). Once the temporal boundary was defined, the preferred direction was calculated independently for the ON and OFF responses for each ooDSGC. The same ON-OFF temporal boundaries were used for all contrasts shown in Fig. 10-Supplement 1. The difference between the preferred directions, $\Delta\phi$, quantified the angular difference between the ON and OFF preferred directions (Fig. 10F).

Analysis of ooDSGC subtypes

ooDSGC subtype classification was performed using the K-means clustering algorithm. This was done by first assigning a set of four initial seed values corresponding to the four cardinal directions of ooDSGCs (Oyster and Barlow, 1967). Next, the angular difference between the seed values (for first iteration) or the cluster means (for later iterations), and the preferred directions of each ooDSGCs was calculated. The cluster for which the angular difference was minimum was the cluster to which an ooDSGC was assigned. This yielded the four subpopulations of ooDSGCs described in Fig. 10-Supplement 1.

QUANTIFICATION AND STATISTICAL ANALYSIS

Statistical analysis was performed using GraphPad Prism software (anatomy/development studies) or using custom JAVA based software and MATLAB software (physiology studies). Statistical tests used for each experiment are given in the METHOD DETAILS section above, and/or in the figure legends. Sample sizes for each experiment are given in the METHOD DETAILS section above or else in the Results. *P*-values ($\alpha = 0.05$) are given in figure legends, or in the Results if no figure is shown. Error bars are defined in figure legends. Exact *p*-values are reported unless the value was less than 1.0×10^{-7}.

Figure 1

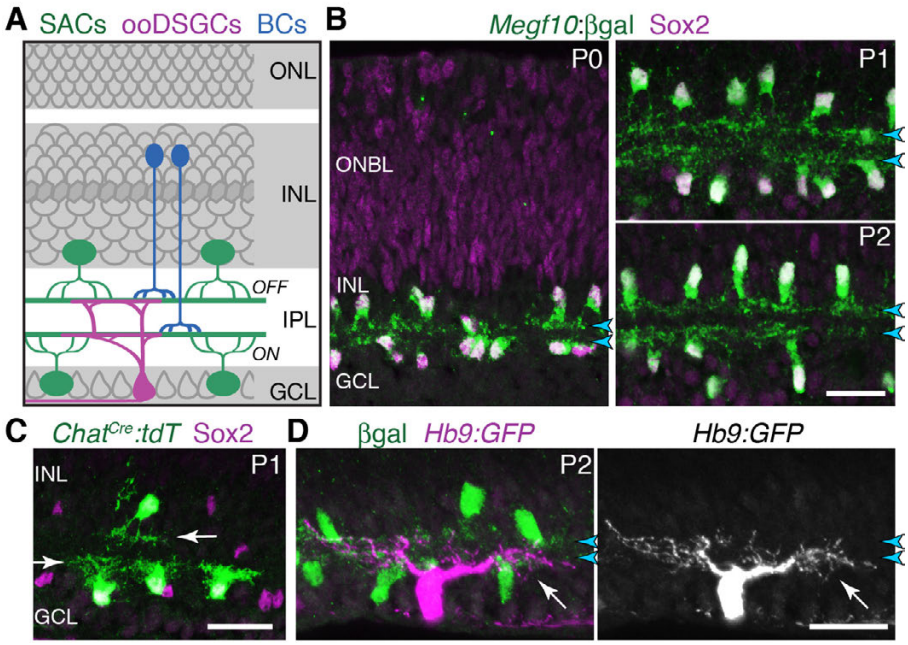

Figure 1: Initial formation of DS circuit IPL sublayers.

A: Schematic of mature direction-selective (DS) circuit and its cell types, depicted in cross-section. SACs (green) and bipolar cells (blue) project to one of two IPL sublayers (*OFF, ON*). OFF SACs reside in inner nuclear layer (INL); ON SACs reside in ganglion cell layer (GCL). ooDSGCs (purple) send dendrites to both DS circuit sublayers. ONL, outer nuclear layer.

B: SAC IPL sublayer formation assessed in *Megf10*^{lacZ} mice. All SACs are double-positive for anti-Sox2 (purple) and anti-βgal (green). Progenitors in outer neuroblast layer (ONBL) also express Sox2. SAC IPL sublayers (arrowheads) begin to appear by P0, and are fully apparent by P1.

C: Sparse labeling of neonatal SACs in *Chat*^{Cre} mice. Individual SACs have laminar-specific projections by P1 (arrows). tdT, tdTomato.

D. ooDSGCs (labeled by *Hb9:GFP*) project diffusely in the IPL at P2 (arrow), whereas SAC arbors are stratified (right panel, arrowheads). Also see Fig. 1-Supplement 1.

Scale bars: 25 µm.

Figure 2

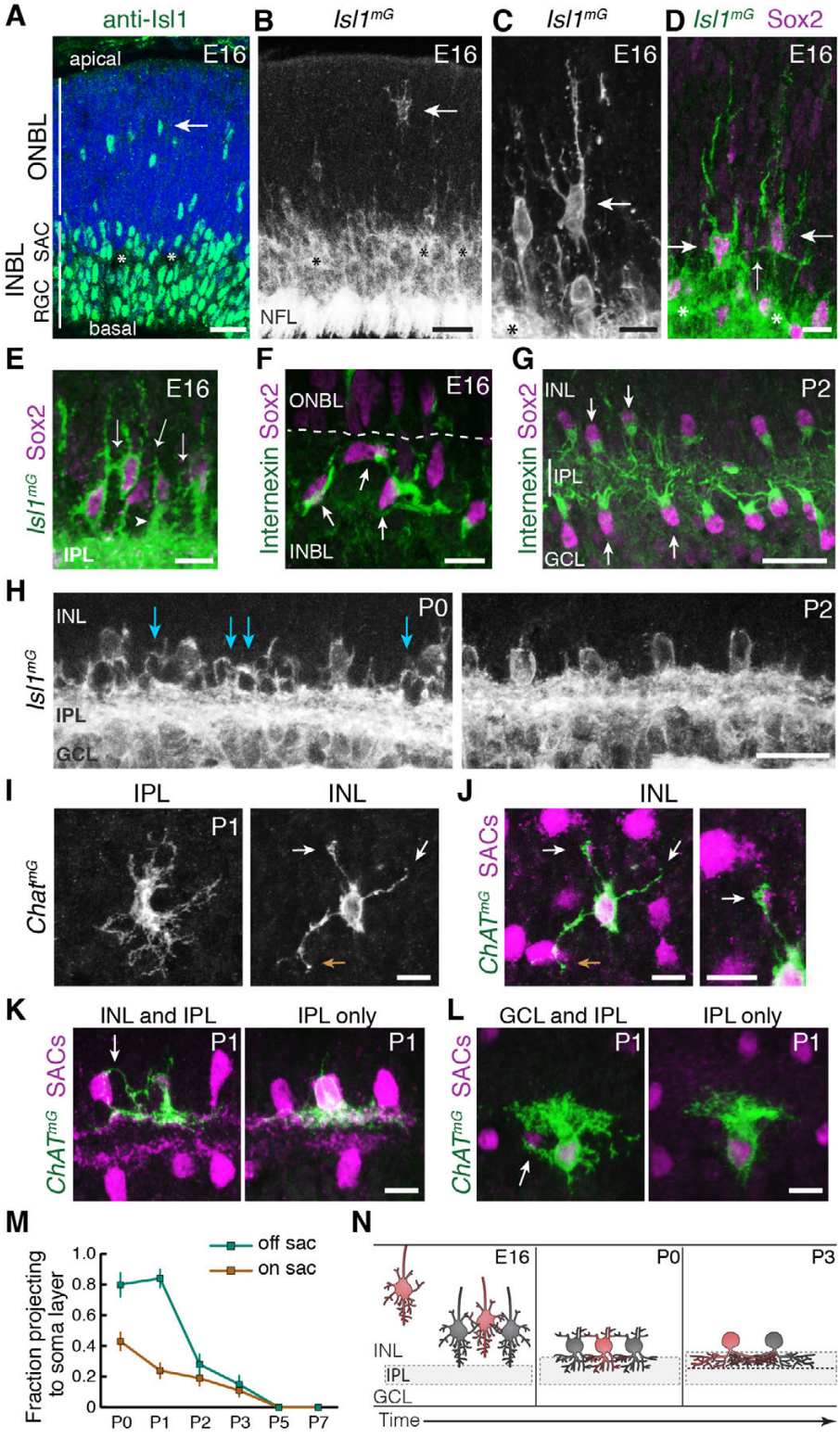

Figure 2: Newborn SACs contact each other via a network of soma-directed arbors.

A,B: Isl1 labels SACs and RGCs in embryonic retina. A, immunostaining; B, mGFP driven by *Isl1*^{Cre} (*Isl1*^{mG}). Arrows, newborn SACs migrating apico-basally through ONBL to inner retina. INBL SACs and RGCs predominantly reside in indicated regions. IPL neuropil (asterisks) exists in discontinuous patches at this age. NFL, nerve fiber layer containing RGC axons. Blue, nuclear counterstain.

B,C: Migrating SACs in ONBL (arrows) have multipolar morphology. They are far from other SACs and do not contact them.

D: Morphology of Sox2^{+}Isl1^{+} SACs (large arrows) upon arrival at INBL. SACs contact each other outside the IPL (small arrow, connecting arbor). Their migratory morphology and distance from IPL (asterisks) indicate they have not yet innervated IPL (also see Fig. 2-Supplement 2).

E: A network of arbors connects somata of INBL SACs (small arrows). Arrowhead, IPL-directed projection.

F,G: Internexin immunostaining reveals polarization of SAC primary dendrites at E16 (F) and P2 (G). P2 SACs project exclusively towards the IPL. E16 INBL SACs often project towards neighboring SAC somata (F) as well as towards the ONBL (Fig. 2-Supplement 2).

H: Soma-directed SAC arbor network remains prominent in INL at P0 (arrows) but mostly gone by P2.

I,J: An individual P1 OFF SAC labeled by *Chat*^{mG} (see Fig. 1-Supplement 1), imaged *en face* to show its arbor morphology at IPL and INL levels. J: INL arbors make selective contacts with SAC neighbors (purple; *Megf10*:βgal). GFP^{+} arbor tips terminate on SAC somata (orange arrow) or SAC arbors (white arrows). Right panel (J): Higher magnification view of touching arbors.

K,L: Individual P1 OFF (K) and ON (L) SACs labeled by *Chat*^{mG} (green) in cross-section. Purple, full SAC population (F, *Megf10*:βgal; G, Sox2). Some SACs are bi-laminar with arbors that contact neighboring somata (arrows, left panels); others project only to IPL (right panels).

M: Frequency of soma layer projections across development, determined from single *Chat*^{mG} cells as in K,L. Error bars, standard error. Sample sizes, see Methods.

N: Schematic of newborn SAC morphology based on B-L. Soma-directed homotypic contacts are established upon completion of migration, and are mostly eliminated by P3.

Scale bars: 25 μm (A,B,G,H); 10 μm (C-F, I-L)

Figure 3

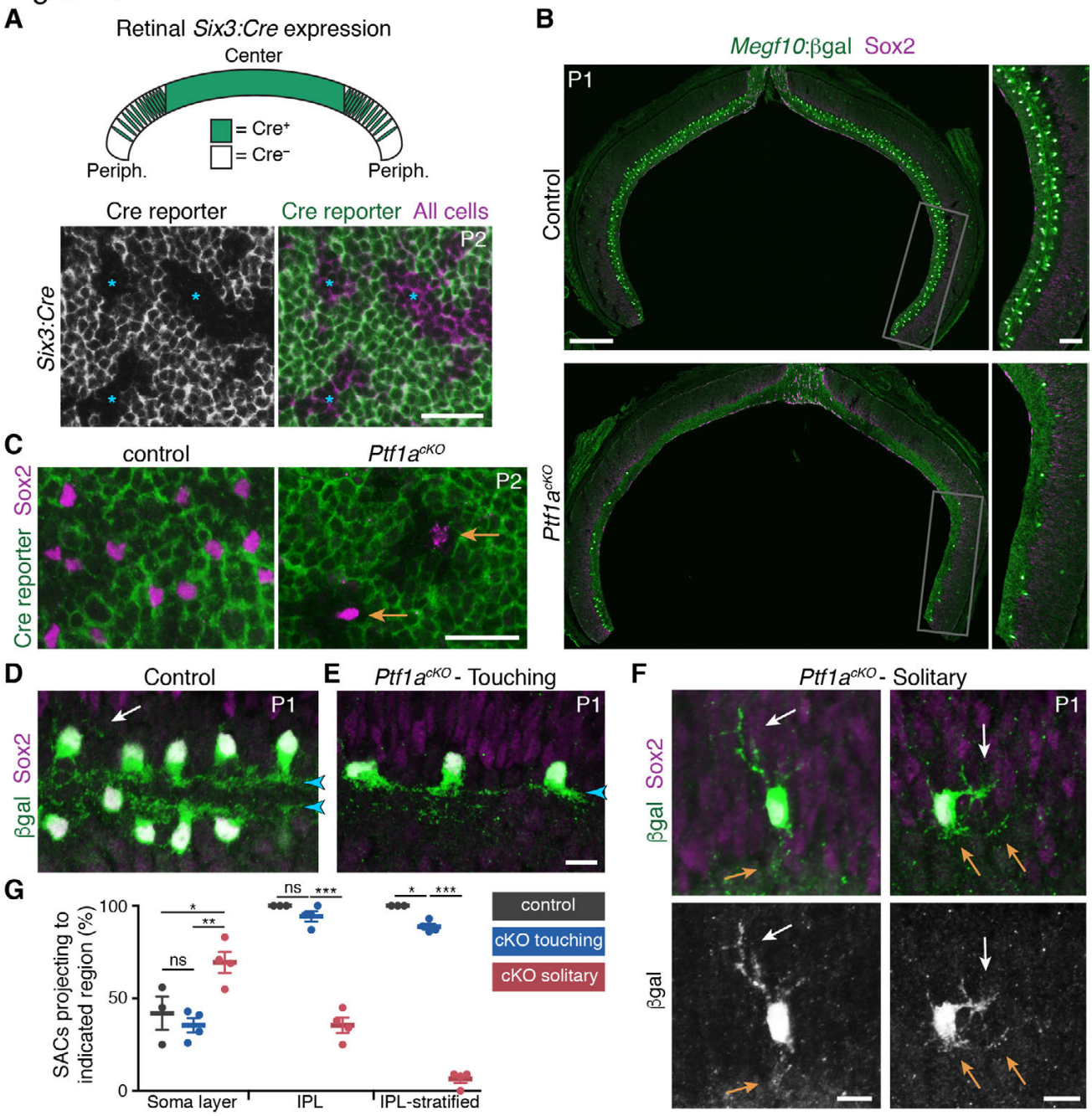

Figure 3: SAC homotypic contact is required for IPL sublayer formation.

A: Top: Schematic illustrating *Six3:Cre* expression pattern in retinal cross-section. Bottom: *En-face* view of *Six3:Cre* recombination in peripheral retina, revealed using GFP Cre reporter. Asterisks, Cre^{-} regions.

B. Reduced SAC density in $Ptf1a^{cKO}$ retina. SACs (labeled by Sox2 and $Megf10^{lacZ}$) are completely eliminated from $Ptf1a^{cKO}$ central retina; some remain in peripheral retina (boxed regions, right panels). Top, littermate control ($Ptf1a^{+/+}$).

C: *En-face* view of SACs in peripheral retina of $Ptf1a^{cKO}$ and littermate control. Green, GFP Cre reporter. Control SACs were either Cre^{+} or Cre^{-}. Mutant SACs were Cre^{-} (arrows), indicating that they derive only from cell lineages that maintain *Ptf1a* function.

D-F: SAC IPL laminar targeting in *Ptf1a*^{cKO} (E,F) and littermate control (D). *Ptf1a*^{cKO} SACs close enough to touch (E) form IPL strata (blue arrowheads), similar to control SACs (D). Solitary SACs (F) are not polarized towards IPL; they have extensive INL-directed arbors (white arrows) and rudimentary IPL-directed arbors (orange arrows). Some solitary SACs entirely fail to innervate IPL (F, left cell) and resemble migrating E16 SACs (Fig. 2C); others innervate IPL with minimally-branched, non-stratified arbors (F, right cell).

G: Quantification of SAC dendrite phenotypes at P1-2. Left, frequency of soma layer innervation. *$p = 0.0350$; **$p = 0.0081$; ns, $p = 0.7516$. Center, frequency of IPL innervation failure (e.g. F, left). ***$p = 4.0 \times 10^{-7}$; ns, $p = 0.3723$. Right, frequency of cells that send arbors into IPL but fail to stratify (e.g. F, right). * $p = 0.0110$; ***$p < 1.0 \times 10^{-7}$. Dots, individual animals. Error bars, S.E.M. P-values, Tukey's post-hoc test. Sample sizes, see Methods.

Scale bars: 25 µm (A,C); 200 µm (B, left), 50 µm (B, right), 10 µm (D-F). Also see Fig. 3-Supplement 1.

Figure 4

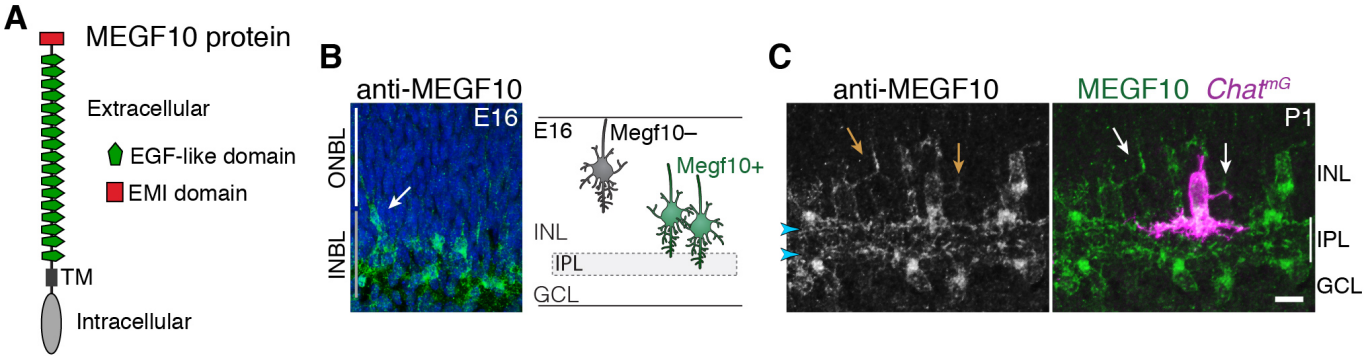

Figure 4: MEGF10 is expressed by SACs during early homotypic contact

A: Schematic of MEGF10 protein. TM, transmembrane domain.

B: Left, MEGF10 immunostaining at E16 reveals onset of protein expression at conclusion of radial migration. INBL SACs express MEGF10, but SACs migrating through ONBL do not. Arrow, INBL SAC with migratory morphology suggesting it is newly-arrived. Right: Schematic illustrating timing of *Megf10* expression onset in SACs (also see Kay et al., 2012).

C: Soma-directed SAC arbors in the INL (arrows) express MEGF10 protein. IPL dendrites are also labeled (arrowheads).

Figure 5

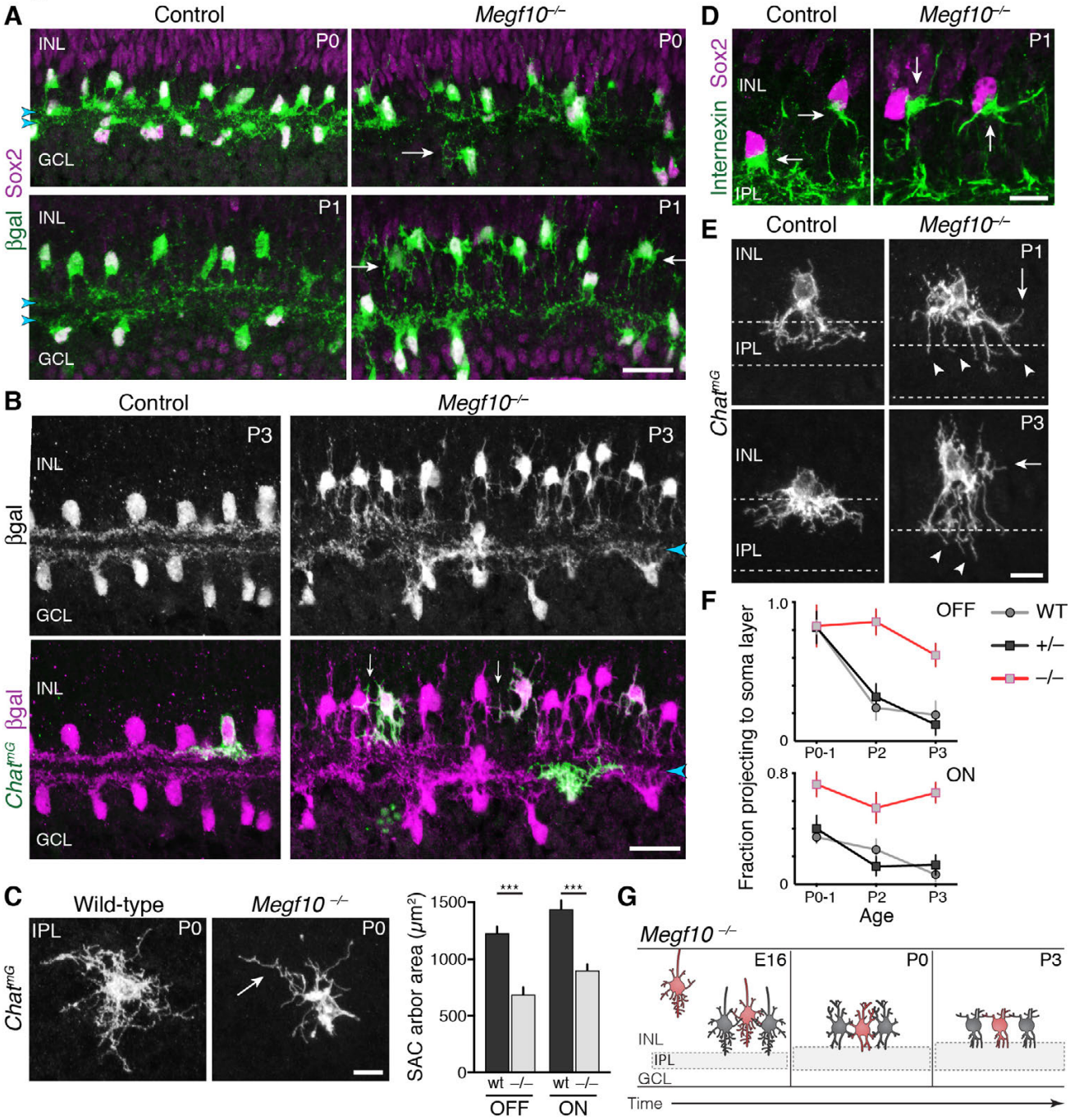

Figure 5: *Megf10* is required for initial formation of SAC IPL sublayers.

A: SAC sublayers are absent from P0-1 *Megf10* mutant IPL. Antibodies to Sox2 and βgal reveal SACs in retinal cross-sections. Littermate control, *Megf10*$^{lacZ/+}$. Arrowheads, SAC IPL strata. Arrows, exuberant arbor growth in mutant INL and GCL. Note that mutant somata abut the IPL at P0, indicating their radial migration was normal. By P1 OFF somata have moved apically.

B: At P3, SAC IPL sublayers remain disrupted in *Megf10* mutants. Single SACs (*Chat*^{mG}) and full population (*Megf10*:βgal) labeled in cross-sections. Mutant OFF SACs mostly project within INL (arrows). INL projections are absent from controls. Some ON SACs are stratified in mutants (arrowhead) but have not yet formed a continuous restricted sublayer as is seen in controls.

C: *En-face* view of single OFF SACs, imaged in whole-mount at IPL level. Mutant SAC dendrites appear undifferentiated, with less branching (arrow). Their arbors cover smaller arbor territories than SACs from wild-type (wt) littermate controls (quantified at right, mean ± s. e. m.). ***p(on) < 1.0×10^{-7}, p(off) = 9.38×10^{-5}; one-way ANOVA/Tukey's post-hoc test. Sample size, see Methods.

D: Internexin immunoreactivity reveals orientation of SAC primary dendrites (arrows) at P1. Right: Example of mutant SACs projecting primary dendrites directly towards each other. Control primary dendrites were exclusively oriented towards IPL (left).

E: Single OFF SACs labeled by $Chat^{mG}$ in cross sections (see Fig. 5-Supplement 1 for ON SACs). Arrows, arbors in INL. Mutant IPL projections (arrowheads) fail to arborize or stratify.

F: Frequency of soma layer projections across development in mutants (–/–) and littermate controls (+/–), determined from single $Chat^{mG}$ cells as in E. Wild-type (WT) data replotted from Fig. 2M to show that +/– controls resemble WT. Error bars, standard error. Sample size, see Methods.

G: Summary of $Megf10^{-/-}$ phenotype. After initial contact at E16, mutant SACs do not immediately innervate the IPL, instead overgrowing arbors in cell body layers (P0). This leads to delayed sublayer formation and persistent soma-layer projections at P3.

Scale bars: 25 µm (A,B); 10 µm (C-E). Also see Fig.5-Supplement 1.

Figure 6

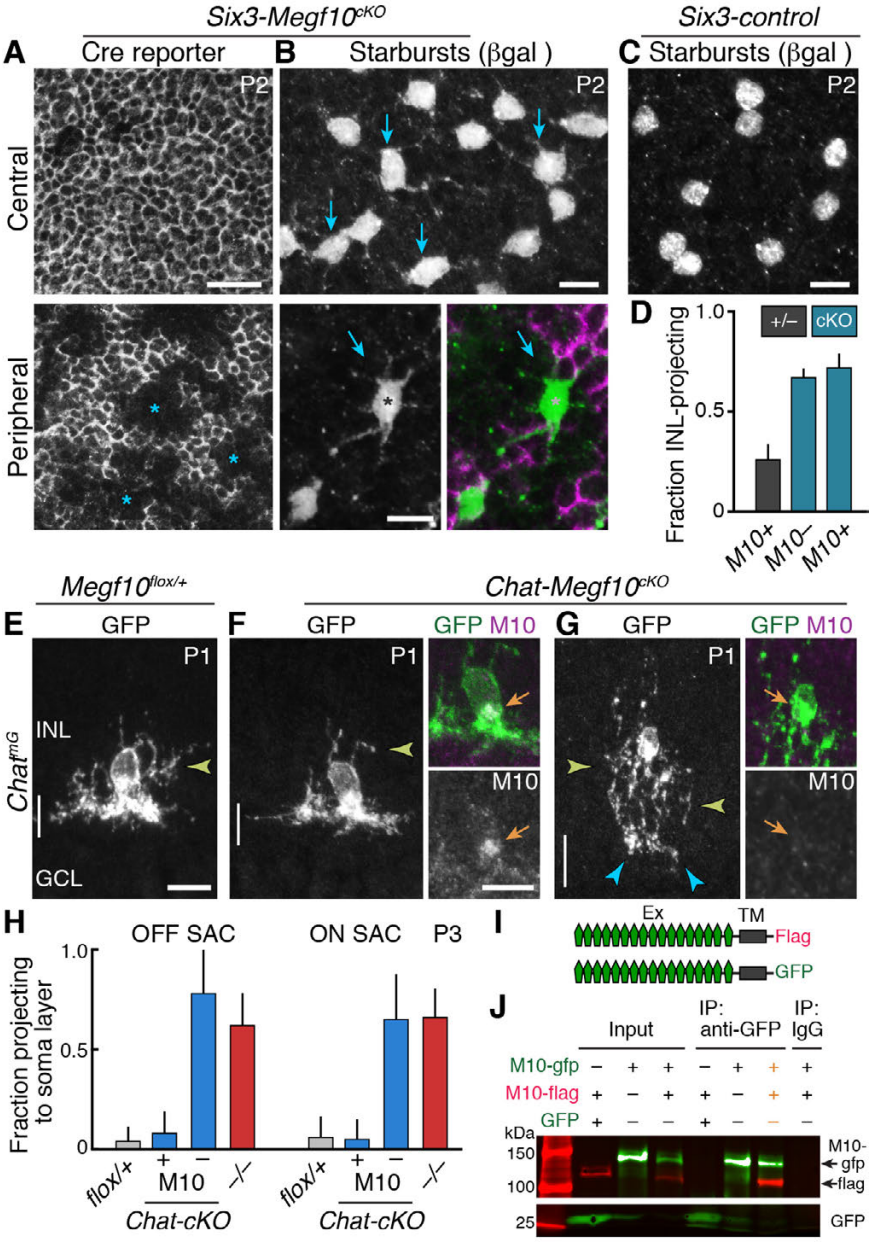

Figure 6: *Megf10* mediates transcellular SAC signals for dendrite development.

A,B: *En-face* images of INL in *Six3-Megf10*^{cKO} retinas stained for GFP Cre reporter (A) and βgal SAC marker (B). Reporter expression indicates loss of MEGF10 (see Fig. 6-Supplement 1). In central retina (top row), most SAC are mutant, and project extensive INL dendrites (B, arrows; compare to C). In peripheral retina (bottom row), some cells escape Cre (asterisks) and retain MEGF10 but still make ectopic INL projections. Purple, Cre reporter; green, βgal.

C: Littermate control retina imaged as in B; SACs rarely project INL dendrites.

D: Quantification of P2 INL projection phenotypes illustrated in A-C. *Six3-Megf10*^{cKO} (*cKO*) SACs that escape Cre (M10^{+}) make projection errors at similar rate as surrounding mutant cells from the same tissue (M10$^{–}$).

E-G: *Chat-Megf10*^{cKO} phenotype. Morphology of single SACs, revealed by *Chat*^{mG} in cross-sections. Anti-MEGF10 (M10) distinguished two classes of *cKO* SACs (orange arrows): Those that express MEGF10 (F) are anatomically similar to littermate control SACs (E). Those lacking MEGF10 (G) arborize extensively in INL (yellow arrowheads) but minimally in IPL (blue arrowheads). Vertical line, IPL.

H: Quantification of SAC soma-layer projection frequency at P3. Sparse M10 deletion (blue, –) phenocopied germline null (red). *Chat-Megf10*^{cKO} cells that retained M10 (blue, +) resembled controls (*flox/+*).

I: Schematic of MEGF10 proteins used for co-immunoprecipitation (IP). Intracellular domain was deleted (ΔICD) and replaced with epitope tags (Flag or GFP). Ex, extracellular; TM, transmembrane.

J: Co-IP from lysates of HEK 293T cells transfected with indicated constructs (I). Western blot with antibodies to GFP (green) and Flag (red). IP with anti-GFP, but not rabbit IgG control, pulled down both MEGF10-ΔICD constructs (2nd lane from right, orange text). IP with anti-Flag gave similar result (Fig. 6- Supplement 2). GFP alone did not co-IP with M10-Flag. Ladder molecular weights (kDa) at left. Full blots in Fig. 6-Supplement 2.

Error bars, 95% confidence interval. Sample sizes, see Methods. Scale bars: 25 μm (A), 10 μm (B-G).

Figure 7

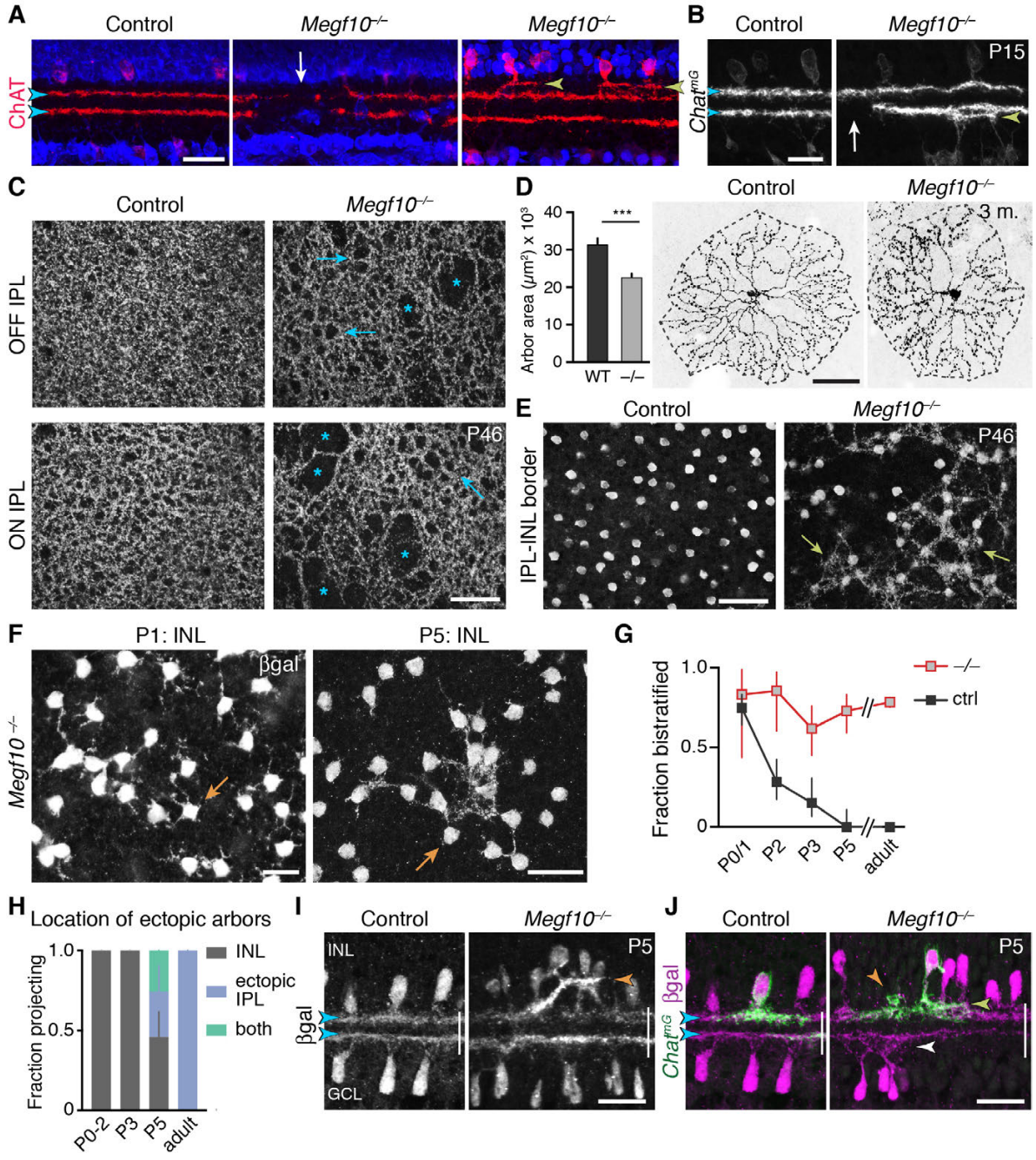

Figure 7: SAC IPL errors persist to maturity in *Megf10* mutants.

A,B: SAC IPL phenotype in mature (two-week-old) retina, cross-section view. Blue, soma counterstain. Control IPL has two continuous SAC dendrite bands (blue arrowheads). Mutant IPL has sporadic SAC laminar gaps (white arrows) or ectopic arbors (yellow arrowheads).

C: *En-face* views of SAC dendrites, stained with anti-ChAT, in adult retinal whole-mounts. The same fields of view are shown at two different z-stack planes, corresponding to OFF and ON SAC sublayers. SAC dendrite plexus is uniform in littermate controls, but has holes (arrows) and large gaps (asterisks) in mutants. Note that errors are not spatially correlated between OFF and ON sublayers.

D: Single SAC labeling in adult (3 month old) mice, via $Chat^{Cre}$-dependent viral fluorescent protein expression. $Megf10^{-/-}$ SACs have relatively normal morphology but are significantly smaller than wild-type (WT) control cells (***$p = 4.6 \times 10^{-6}$, two-tailed *t*-test). Sample size, see Methods.

E: *En-face* images at INL-IPL border from same control and mutant z-stacks shown in C. A network of ectopic SAC dendrites (yellow arrows) is evident mutants but not controls.

F: Ontogeny of ectopic SAC network in *Megf10* mutants, revealed by *en-face* images at INL level. *Megf10:*βgal labels SACs. At P1, INL-projecting cells send fine arbors in many directions. At P5, INL projections are

directed toward ectopic arbor aggregates, similar to adults (E). Arrows, cells making multipolar (left) or directed (right) INL projections. Littermate controls are shown in Fig. 7-Supplement 1.

G: Frequency of ectopic OFF SAC projections does not change over development, despite changes in arbor anatomy (F). P0-3 data replotted from Fig. 5F, with both control groups combined. Sample sizes, see Methods.

H: Classification of ectopic arbor location in *Megf10*$^{-/-}$ OFF SACs that made ectopic projections. Ectopic arbors localize to soma layer before P5, and to IPL in adults. P5 is a transitional stage when exuberant arbors can project to either or both ectopic targets. Sample sizes as in G (see Methods).

I,J: Transition of ectopic OFF SAC projections from INL to IPL at P5. Arbor fascicles (orange arrowhead) crossed the INL-IPL boundary at P5 (I), whereas they were confined to IPL in two-week-old mice (A). J: An individual P5 *Megf10*$^{-/-}$ SAC projects to three different locations: 1) correct IPL sublayer (blue arrowhead); 2) inappropriate IPL sublayer (yellow arrowhead); 3) ectopic INL arbor aggregate (orange arrowhead). ON SACs also make ectopic IPL projections (J, white arrowhead). Control cells are monostratified in IPL (left). Note that IPL sublayers have formed by P5 in mutants (I).

Error bars, 95% confidence intervals. Scale bars: 25 µm (A,B,F,I,J); 50 µm (C-E).

Figure 8

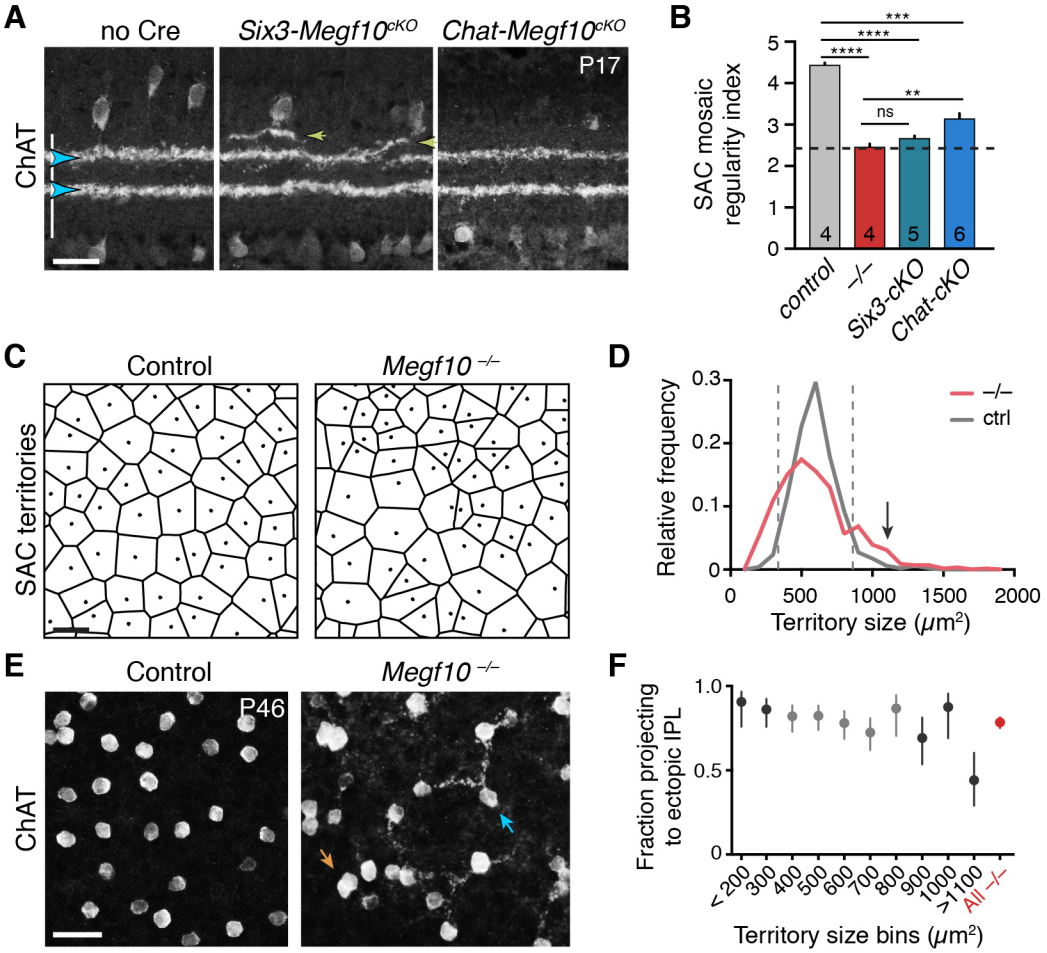

Figure 8: Minimal influence of soma positioning errors on *Megf10*$^{-/-}$ IPL phenotype

A: SAC IPL errors (yellow arrowheads) induced by early deletion of *Megf10* in *Six3-Megf10*^{cKO} mice, but not late deletion in *Chat-Megf10*^{cKO} mice.

B: Mosaic spacing phenotype measured at P17 using Voronoi domain regularity index. Dashed line, index for simulated random SAC arrays. In both *Six3* and *Chat* conditional mutants, SAC positioning is less regular than in controls (*Chat*^{Cre}; *Megf10*$^{flox/+}$). *Megf10*$^{-/-}$ and simulation data from Kay et al. (2012). ns, $p = 0.6438$; **$p = 0.0023$; ***$p = 2.1 \times 10^{-6}$; ****$p < 1.0 \times 10^{-6}$ (one-way ANOVA/Tukey's post-hoc test). Error bars, S.E.M.

C,D: Voronoi domain territory size as a single-cell measure of mosaic perturbation. Territory size images (C) and histograms (D, 100 μm^2 bins) for adult littermate controls and *Megf10* mutants. Because mutant SAC positions are random, their locations are less constrained, leading to a wider range of territory sizes than in controls. Dashed lines (D), upper and lower 95% tolerance intervals of the control distribution. Mutant cells outside these lines experience crowding or isolation rarely seen in controls. Arrow denotes largest bin in F. Sample sizes: $n = 515$ cells from 2 littermate control (*Megf10*$^{+/-}$) mice; $n = 584$ cells from 2 *Megf10*$^{-/-}$ mice.

E: No obvious correlation between a mutant cell's local neighborhood density and its projection to ectopic IPL sublayer. *En-face* view of SAC cell bodies and outer IPL, generated by z-projecting part of a confocal stack corresponding to these layers. Controls lack SAC dendrites at this IPL level. Arrows, examples of cells that are unusually far from their neighbors yet join the ectopic network (blue), or that are unusually crowded yet do not join (orange).

F: Frequency of ectopic IPL projections for mutant SACs in each 100 μm bin of histogram in D. Dark shading, bins outside dashed lines in D. Smallest and largest bins were pooled to ensure adequate sample size ($n \geq 24$ SACs per bin; see Methods for bin sizes). Across all bins except the largest one (denoted in D by arrow), error rate was similar to the overall mutant error rate (red). X values denote bin center (aside from pooled bins <200 μm^2 and >1100 μm^2). Error bars, 95% confidence intervals.

Scale bars (A,C,D), 25μm.

Figure 9

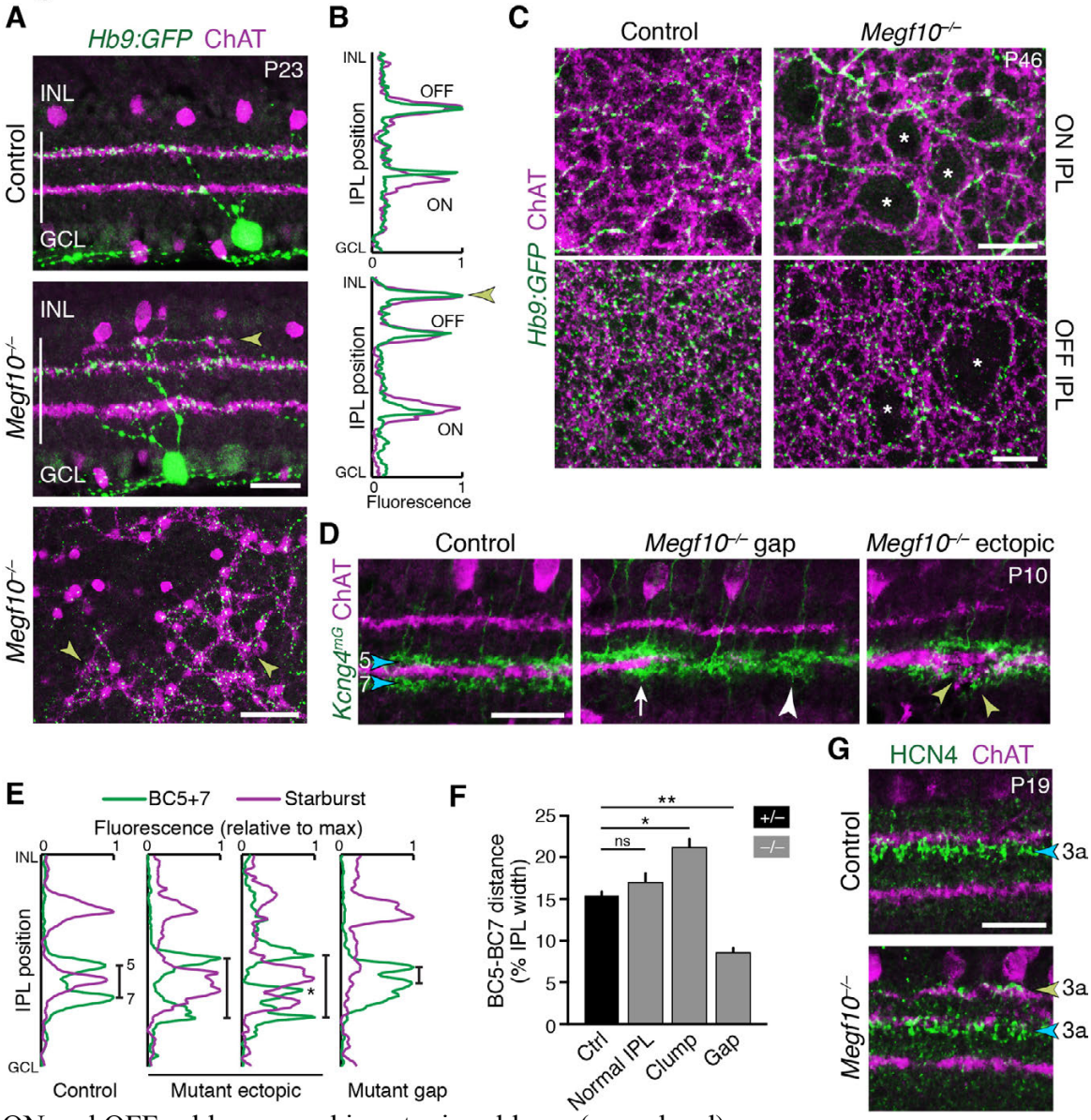

Figure 9: SACs guide IPL sublayer choice by their circuit partners.

A: SACs (ChAT, purple) and ooDSGCs (*Hb9:GFP*, green) labeled in cross-sections (top, middle) and *en-face* view (bottom). In *Megf10* mutants, ectopic SAC arbors (arrowheads) are extensively innervated by ooDSGC dendrites.

B: Quantification of fluorescence intensity across IPL in cross-section images from A. ooDSGC dendrites (green) strictly co-localize with SAC arbors (purple) in ON and OFF sublayers, and in ectopic sublayer (arrowhead).

C: *En-face* view of ON (top) and OFF (bottom) SAC IPL sublayers. In *Megf10* mutants, ooDSGC dendrites (green) fail to enter IPL regions (asterisks) that are not innervated by SACs (purple).

D,E: BC5 and BC7 IPL projections (blue arrowheads), labeled in $Kcng4^{mG}$ mice. D, images; E, representative fluorescence plots of $Kcng4^{mG}$ (green) and ChAT (purple) across IPL. In littermate controls, or normal regions of mutant IPL (D, arrow), BC5 and BC7 arborize in sublayers immediately adjacent to ON SAC layer, but do not enter it. In *Megf10* mutants, ectopic SAC arbors displace BC5+7 terminals to new IPL locations, where they remain adjacent to SACs but non-overlapping (D, yellow arrowheads; E, center plots). Asterisk (E): ectopic BC arbors between normal and ectopic SAC strata. BC5/7 arbors that innervate SAC gaps are abnormally close together (D, white arrowhead; E, right plot). Vertical bars in E: distance between BC5/7 terminals.

F: Quantification of BC5-BC7 distance. *$p = 0.0219$; **$p = 0.0012$; ns, $p = 0.3965$ (Tukey's post-hoc test). Sample sizes, see Methods. Error bars, S.E.M.

G: Mislocalized SAC arbors recruit BC3a bipolar axons (HCN4, green) to ectopic IPL locations.

All scale bars: 25 µm. Also see Fig. 9-Supplement 1.

Figure 10

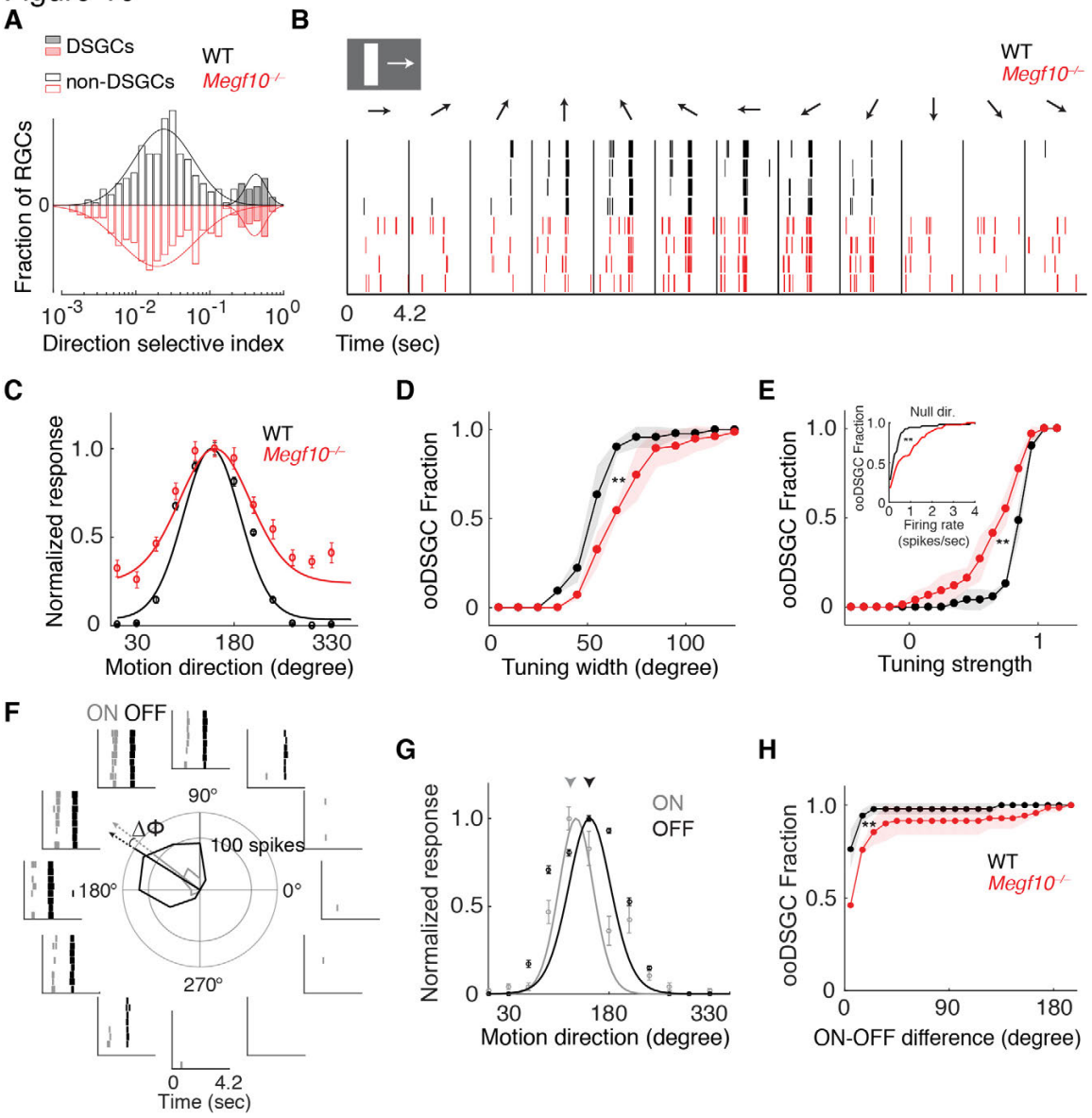

Figure 10: Broader and weaker direction tuning of ooDSGCs in *Megf10* mutants.

A: Histograms of RGC direction selectivity indices, measured on a multielectrode array, for wild-type (WT, black) and *Megf10*$^{-/-}$ (red) retinas. Bimodal histograms fit with two-Gaussian mixture model distinguished DSGCs (filled bars) from non-DSGCs (open bars).

B: Spike rasters from representative WT and *Megf10*$^{-/-}$ posterior-preferring ooDSGCs in response to a bright bar moving along 12 directions (arrows).

C: Direction tuning curves from cells in B normalized to the maximum response (line: von Mises fit). Non-zero values at tails of mutant curve reflect increase in null-direction spikes (B, left- and right-most bins).

D,E: Cumulative distribution of tuning widths (D) and tuning strengths (E) for all ooDSGCs recorded from two retinas of each genotype (WT $n = 80$ cells; *Megf10*$^{-/-}$ $n = 74$ cells). Mutant ooDSGC population is tuned more broadly (D, right shift of red curve) and more weakly (E, left shift of red curve) than WT. Mutant ooDSGCs also exhibit higher firing rate to null direction motion (E, inset). $^{**}p = 0.005$ (D), $p = 0.003$ (E), paired KS-test.

F: Rasters and polar plot of a representative WT ooDSGC, highlighting preferred directions of ON (gray) and OFF (black) responses (arrows). $\Delta\phi$, angular difference between preferred directions of ON and OFF responses.

G: ON and OFF direction tuning curves for cell in F (line, von Mises fit). ON and OFF preferred directions (arrowheads) are well aligned in WT retina.

H: Cumulative distribution across all ooDSGCs of ON-OFF preferred direction difference ($\Delta\phi$). Same cells as in D,E. Rightward shift of mutant curve indicates larger ON-OFF misalignment. $^{**}p = 0.004$, paired KS test.

For all panels, background light level was photopic (10^4 P*/M-cone/sec; contrast of moving bar was 60%). Error bars/bands, S.E.M. Also see Fig. 10-Supplement 1.

Formation of retinal direction-selective circuitry initiated by starburst amacrine cell homotypic contact

Thomas A. Ray, Suva Roy, Christopher Kozlowski, Jingjing Wang, Jon Cafaro, Samuel W. Hulbert, Christopher V. Wright, Greg D. Field, and Jeremy N. Kay

SUPPLEMENTAL FIGURES & LEGENDS

Figure 1 - Supplement 1

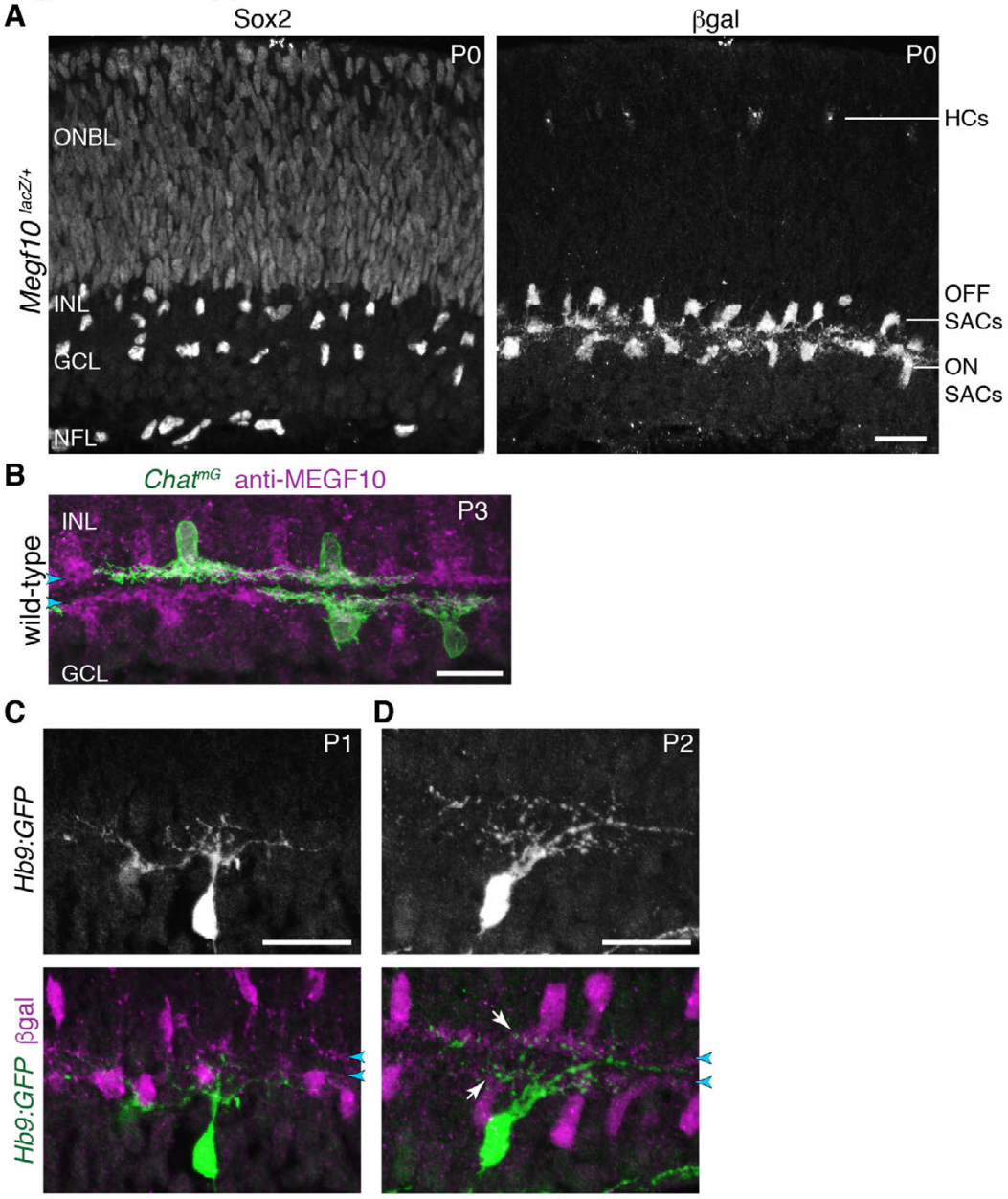

Figure 1-Supplement 1: Markers for SACs and ooDSGCs in neonatal retina.

A.B: Characterization of Sox2, MEGF10, and *Chat*^{Cre} as markers that label SACs in the neonatal mouse. All images depict retinal cross-sections. **A**: Individual color channels of P0 image shown in Fig. 1B. Sox2 (A, left panel) is a pan-SAC nuclear marker. Antibodies to Sox2 strongly label all SACs in the inner nuclear layer (INL) and ganglion cell layer (GCL), as well as astrocytes in the nerve fiber layer (NFL). Progenitor cells in the outer neuroblast layer (ONBL) are weakly labeled. Antibodies to βgal (A, right panel) label the complete SAC population in *Megf10*^{lacZ} mice. Horizontal cells (HCs) in outer retina are also labeled.

B: Antibodies to MEGF10 (purple) are selective for SACs and label the complete SAC population. *Chat*^{mG} mice (i.e. *Chat*^{Cre} crossed to membrane-targeted GFP Cre reporter) label a subset of SACs in the neonatal retina (green). Whereas *Chat*^{Cre} is a marker of the full SAC population at later stages, its expression in neonatal retina is more sporadic (Xu et al., 2016). We took advantage of this feature for two purposes: 1) Single-cell anatomy studies of SAC dendrite morphology, as shown here; 2) Sporadic early knock-out of genes in a sparse subset of SACs (See Fig. 6).

C,D: Anatomy of neonatal ooDSGCs labeled with *Hb9:GFP*. At P1 (C), ooDSGC dendrites are rudimentary with few branches. No IPL stratification is evident. At P2 most ooDSGCs remain unstratified as depicted in Fig 1D. However, a minority of P2 ooDSGCs have dendrites that co-stratify with SAC dendrites (*Megf10:*βgal; blue arrowheads); an example is shown in (D). See main text for quantification of stratification frequency.

Scale bars: 25 μm.

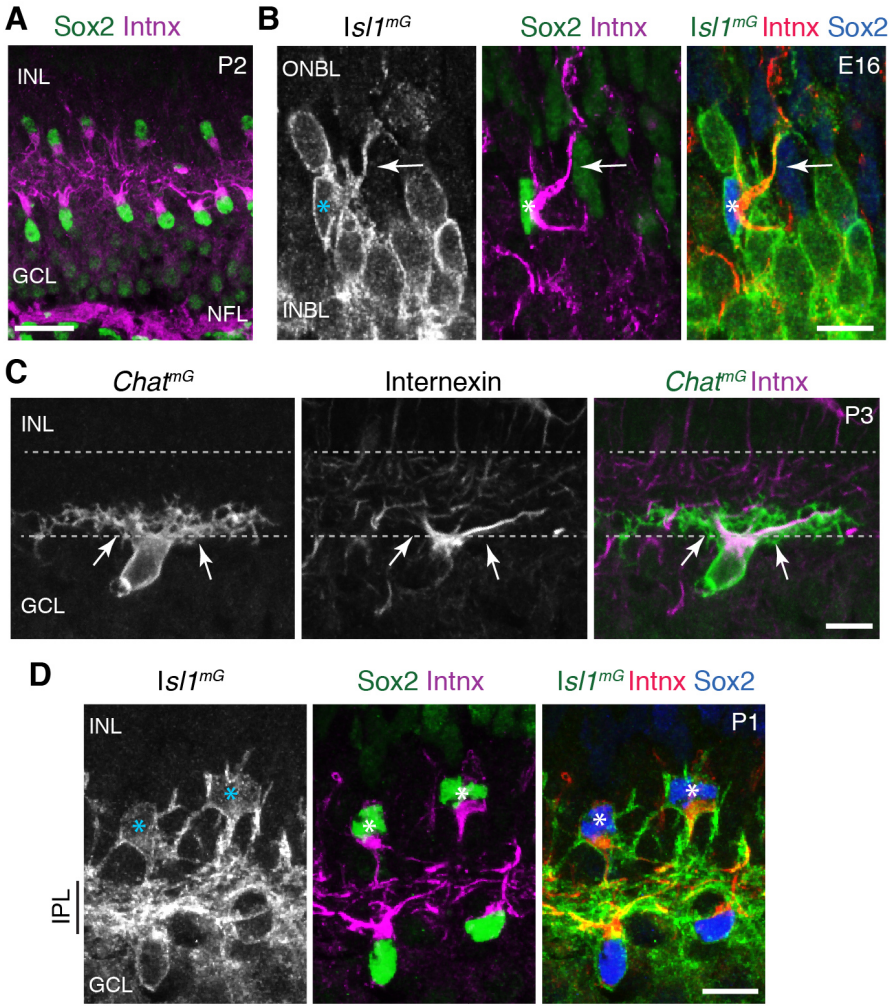

Figure 2-Supplement 1: Characterization of internexin as a primary dendrite marker of developing SACs.

A: Expression pattern of internexin in P2 mouse retina. Internexin (Intnx) immunoreactivity is detected in Sox2^{+} SACs, and in RGC axons within the nerve fiber layer (NFL). This pattern is typical of the entire first postnatal week. In RGCs, axons are selectively labeled; their cell bodies in the GCL are internexin-negative. In SACs, internexin selectively labels primary dendrites, as well as the portion of the soma from which the primary dendrites arise. Therefore, internexin^{+} intermediate filaments are trafficked to specific subcellular compartments of both SACs and RGCs. P2 SACs are strongly polarized towards the IPL (also at P1; see D). Note that this image is the same one depicted in Fig. 2G, but cropped differently to show NFL staining; also, colors have been reversed to match other panels of this figure.

B: An individual E16 INBL SAC (asterisk), surrounded by *Isl1*^{mG}-positive RGCs (identified as RGCs because they lack Sox2 or internexin staining). At E16, internexin has the same subcellular localization within SACs as at P1-2 (A,D): It localizes to the primary dendrites (arrow) and the side of the cell body from which it emerges. However at E16, SAC primary dendrite orientation is more variable than at P2 (A). This SAC sends a primary dendrite towards the outer retina (ONBL) where it could potentially contact migrating SACs as they arrive at the INBL. Other SACs project within the INBL towards neighboring SAC cell bodies (Fig. 2F), or towards inner retina (not shown).

C: Antibodies to internexin strongly label SAC primary dendrites originating from the cell body (arrows), but fine dendritic branches within IPL are unlabeled. Occasionally, higher-order branches arising from the primary dendrites are weakly labeled. *Chat*^{mG} was used to reveal the full dendritic arbor.

D: Internexin distinguishes IPL-directed primary dendrites from soma-directed arbors in neonatal SACs. *Isl1*^{mG} labels full morphology of bi-laminar P1 OFF SACs (asterisks) that project to both INL and IPL. Only IPL-directed primary dendrites of these cells are internexin-positive (middle, right panels).

Scale bars: 25 µm (A), 10µm (B-D).

Figure 2-Supplement 2

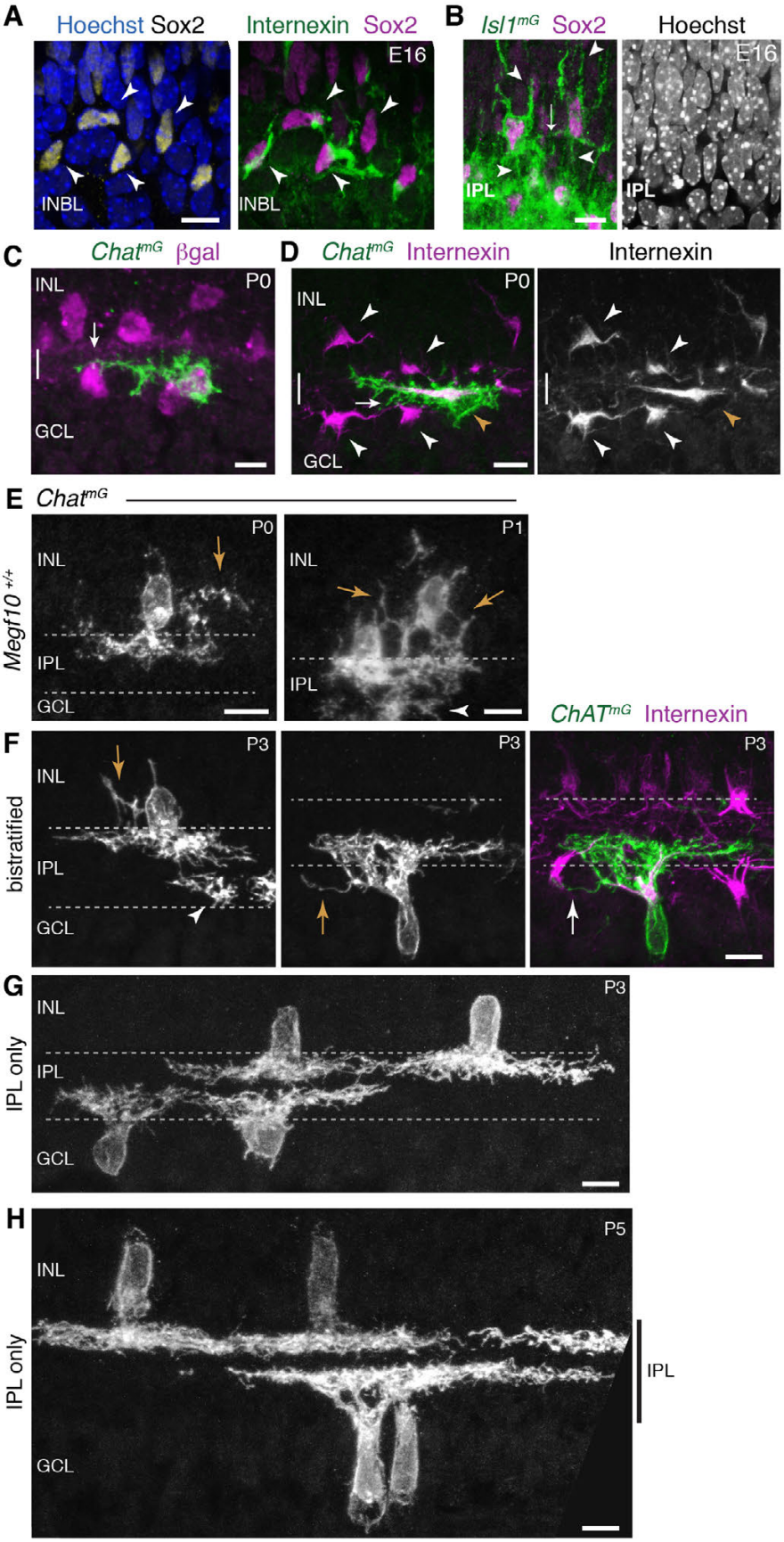

Figure 2-Supplement 2: Homotypic soma-directed SAC arbors across development.

A: E16 homotypic soma-directed contacts can be established prior to IPL formation. Right panel, same cells as Fig. 2F, showing INBL SACs projecting towards each other. Left panel, same field of view showing Sox2 SAC nuclear marker and Hoechst nuclear stain (blue). These SACs are surrounded by other INBL cell bodies, with no IPL neuropil evident in this retinal region.

B: E16 homotypic SAC soma contacts occur outside the IPL. Left panel, same cells as Fig. 2D. These cells have migratory morphology, as shown by their prominent apical and basal processes (arrowheads). They do not make obvious projections into the IPL, delineated by dense *Isl1*^{mG} staining. The contact between the two SACs (arrow) occurs outside of the IPL Right panel, Hoeschst nuclear stain confirms location of nascent IPL inferred from *Isl1*^{mG} labeling. The IPL is a narrow cell-free gap between cell bodies that corresponds to location of dense GFP^{+} arbors (left panel).

C,D: At P0, ON SACs can contact neighboring SAC somata (arrows) without being bi-laminar. Cross-sections of P0 retina, co-stained for individual SACs (*Chat*^{mG}) and for markers of the complete SAC population (C, *Megf10:*βgal; D, internexin). The existence of such cells may help explain why the frequency of soma layer-projecting ON SACs is lower than for OFF SACs (Fig. 2M). D: Internexin staining shows that these ON SACs (orange arrowhead) are polarized along the INL-GCL border towards their neighbors, adopting a horizontal

morphology distinct from surrounding OFF and ON SACs (white arrowheads). This morphology is typical of a displaced amacrine cell in the process of crossing from the INL to the GCL (Chow et al., 2015).

E: Examples of soma layer-projecting *Chat*^{mG}-labeled SACs in mice that are wild-type at the *Megf10* locus (*Megf10*$^{+/+}$), demonstrating that the soma-contacting arbors shown in Fig. 2K,L are not a consequence of *Megf10* heterozygosity. Arrows, arbors in INL. Arrowhead, arbors arising from a neighboring ON SAC with cell body located in adjacent section.

F-H: Examples of P3 (F,G) and P5 (H) cells used to generate graph in Fig. 2M. SAC single-cell morphology was revealed using *Chat*^{mG} labeling. At P3, most SACs project only to the IPL (G), but some SACs still make soma-directed projections (F). Representative INL-projecting OFF cell (F, left) and GCL-projecting ON cell (F, center, right) are depicted. The ON cell makes contact with the neighboring internexin-positive SAC soma (arrow in right panel of F). Arrows, soma-layer projecting arbors. Arrowhead, arbor of a neighboring ON SAC only partially present in the section. At P5 (H), all SACs project exclusively to IPL (vertical bar).

All scale bars: 10 μm.

Figure 3 - Supplement 1

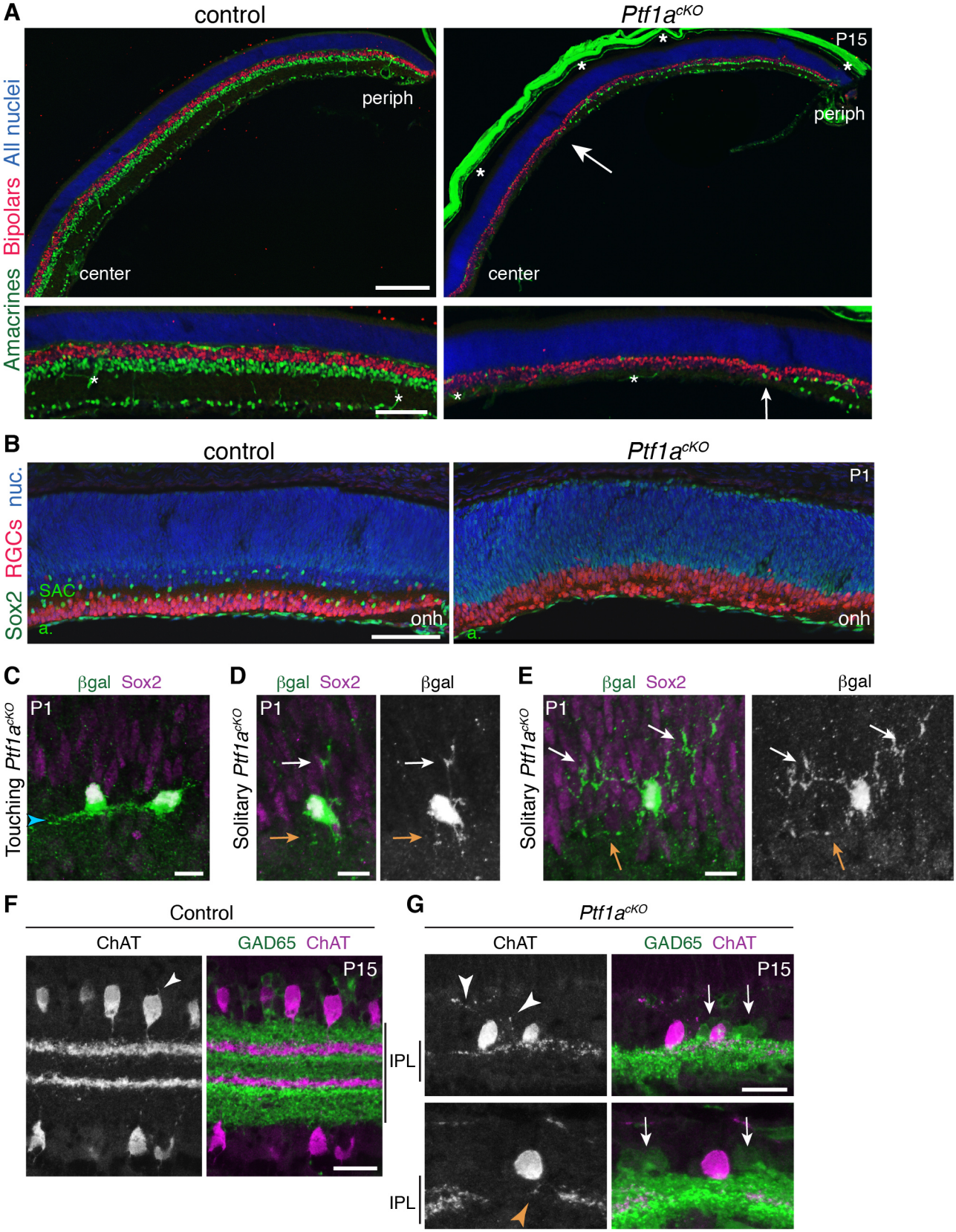

Figure 3-Supplement 1: Retinal phenotype of *Ptf1a*^{cKO} mutants.

A: Immunostaining with pan-amacrine marker AP2α (green) and pan-bipolar marker Chx10 (red), in littermate control and *Ptf1a*^{cKO} retinal cross sections. Blue, Hoechst nuclear counterstain. Top panels: low-power view illustrating center-peripheral differences in amacrine number that arise due to Cre expression pattern (see Fig.

3A-C). Bottom panels: Higher magnification views of mid-peripheral retina. AP2α^{+} cells are completely eliminated from *Ptf1a*^{cKO} central retina. Some amacrines that have escaped Cre recombination (see Fig. 3C) are produced in the periphery, albeit at lower density than controls. Arrow marks central-most amacrine cells. Bipolar cell number is not obviously different between genotypes. Asterisks, non-specific staining, due to anti-mouse secondary antibody, in blood vessels and sclera. Note that sclera became detached from control section prior to imaging.

B: Cross-sections through central retina of littermate control and *Ptf1a*^{cKO} mutant, stained for pan-RGC marker RBPMS (red) and Sox2 (green) to mark SACs. Blue, Hoechst nuclear counterstain (nuc). Optic nerve head (onh) marks center of retina. In *Ptf1a*^{cKO} mice, SACs are entirely absent from central retina, but Sox2+ astrocytes (*a*) in nerve fiber layer are present in normal numbers. RGC cell number appears to be increased, consistent with previous observations in embryonic retina of *Ptf1a* null mice (Fujitani et al., 2006; Nakhai et al., 2007).

C-E: Additional examples of SACs in *Ptf1a*^{cKO} retinal cross-sections, from dataset used to compile graph in Fig. 3G. Neurons were validated as SACs by co-expression of *Megf10:*βgal and Sox2. Touching SACs (C) stratify their arbors normally (arrowhead). Note that the right-hand cell appears to be polarized towards the left-hand cell, suggesting asymmetric growth towards the side with homotypic contact and away from the side lacking it. Representative solitary SACs are shown in D,E. One cell (D) is an example of the class that failed to project to the IPL. The other cell (E) exemplifies the class that sends only abnormal unstratified arbors into the IPL. In this case (E) the cell innervated the IPL with a single minimally-branched dendrite that fails to ramify in a laminar fashion (compare to C). This cell also has particularly exuberant arbors in the INL that were much larger than those seen in any cells that touched their neighbors (e.g. C; also see Fig. 3D,E). White arrows, soma-directed arbors. Orange arrows, IPL-directed arbors.

F-G: SAC errors in *Ptf1a*^{cKO} mutants persist to maturity. P15 littermate control (F) and mutant (G) retinal cross-sections stained for anti-ChAT to label SACs (red) and anti-GAD65 to label a broad non-SAC amacrine population (green). Control SACs no longer have soma-directed arbors at this age; the only processes not directed toward the IPL were very short and minimal (F, arrowhead). In mutant retina, SACs from low-density regions often innervated the INL (G, white arrowheads), or failed to innervate gaps in the SAC IPL network (G, orange arrowhead). SACs that made errors had extensive interactions with GAD65^{+} amacrine cells (G, arrows) and their arbors (green) suggesting that generic amacrine contacts are not sufficient to prevent SAC errors. Instead, because these SACs had few homotypic neighbors, the errors were likely due to paucity of SAC-SAC interactions.

Scale bars: 200 µm (A top); 100 µm (A bottom, B); 10 µm (C-E); 25 µm (F,G).

Figure 5 - Supplement 1

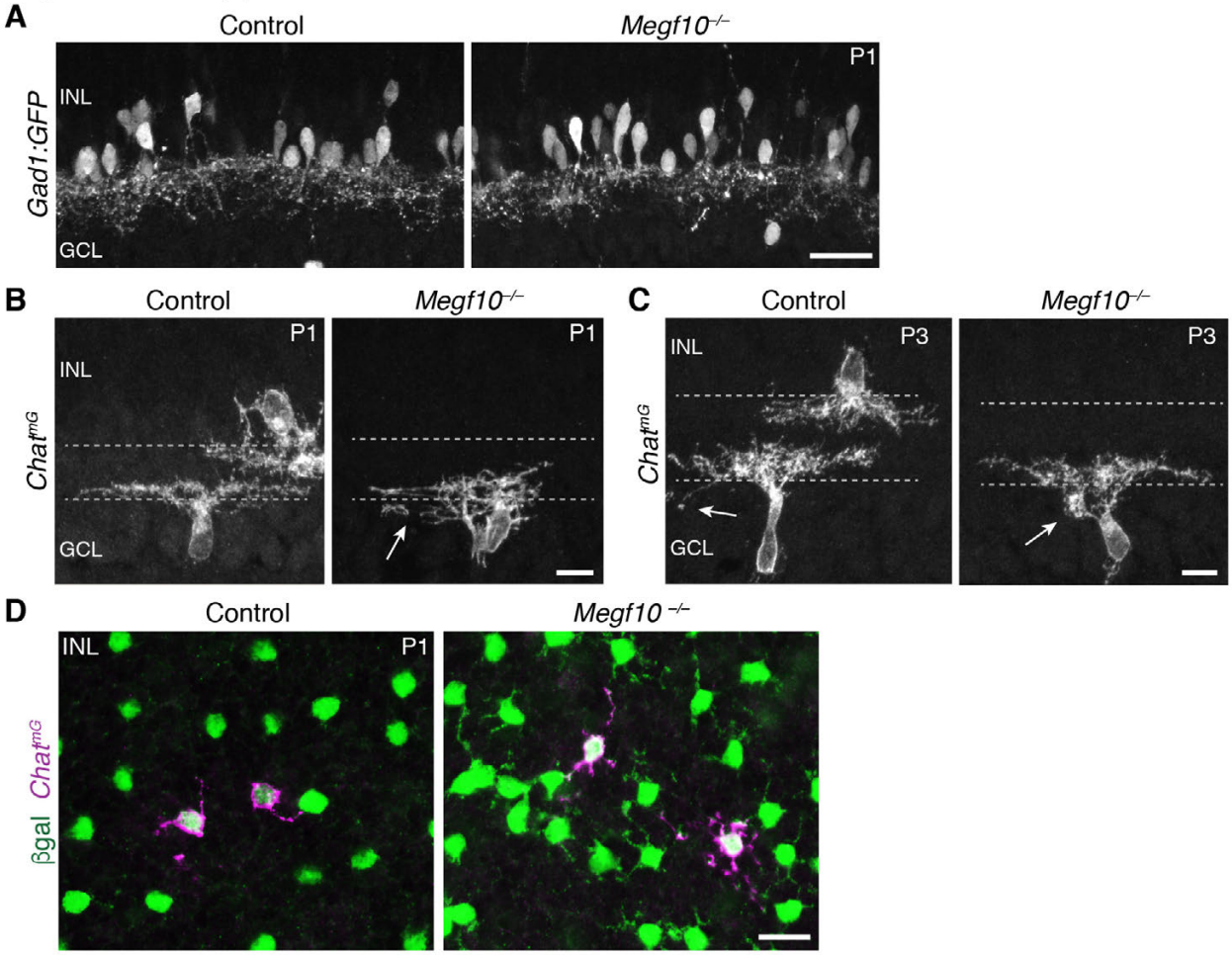

Figure 5-Supplement 1: IPL innervation and sublayer formation phenotypes in *Megf10* mutants.

A: Retinal cross-sections from P1 *Megf10* mutants and littermate (*Megf10*$^{+/-}$) controls carrying the *Gad1:GFP* transgene. A broad subset of non-SAC amacrine cells is labeled by GFP in these mice. Unlike SACs (Fig. 5A), *Gad1:GFP*$^{+}$ amacrine cells innervated the INL normally in *Megf10* mutants, and did not make exuberant projections within the INL.

B-C: Examples of P1 (B) and P3 (C) *Chat*^{mG}-labeled ON SACs that were part of the dataset used to generate graphs in Fig. 5F. At P1 (B) many mutant ON cells are bi-laminar, with projections in both IPL and GCL (arrow, GCL arbor). IPL projections were underdeveloped relative to controls, and not sufficient to generate a clear sublayer (Fig. 5A). C: P3 control and mutant ON SACs, both of which project to the GCL. The control cell sends a single arbor to the GCL (left, arrow), typical of those few SACs that still project to the soma layers at this age. The mutant cell (right) makes a dense dendritic arborization in the GCL (right, arrow), which was never seen in P3 controls.

D: *En-face* view of OFF SACs at INL level shows extensive soma-layer arbor network in P1 mutants. Single SACs (*Chat*^{mG}, purple) have larger and more elaborate INL-directed arbors in mutants than in littermate controls. A single-color version of the left panel, showing only the βgal channel, appears in Fig. 7F.

Scale bars: 25 μm (A,D); 10 μm (B,C).

Figure 6 - Supplement 1

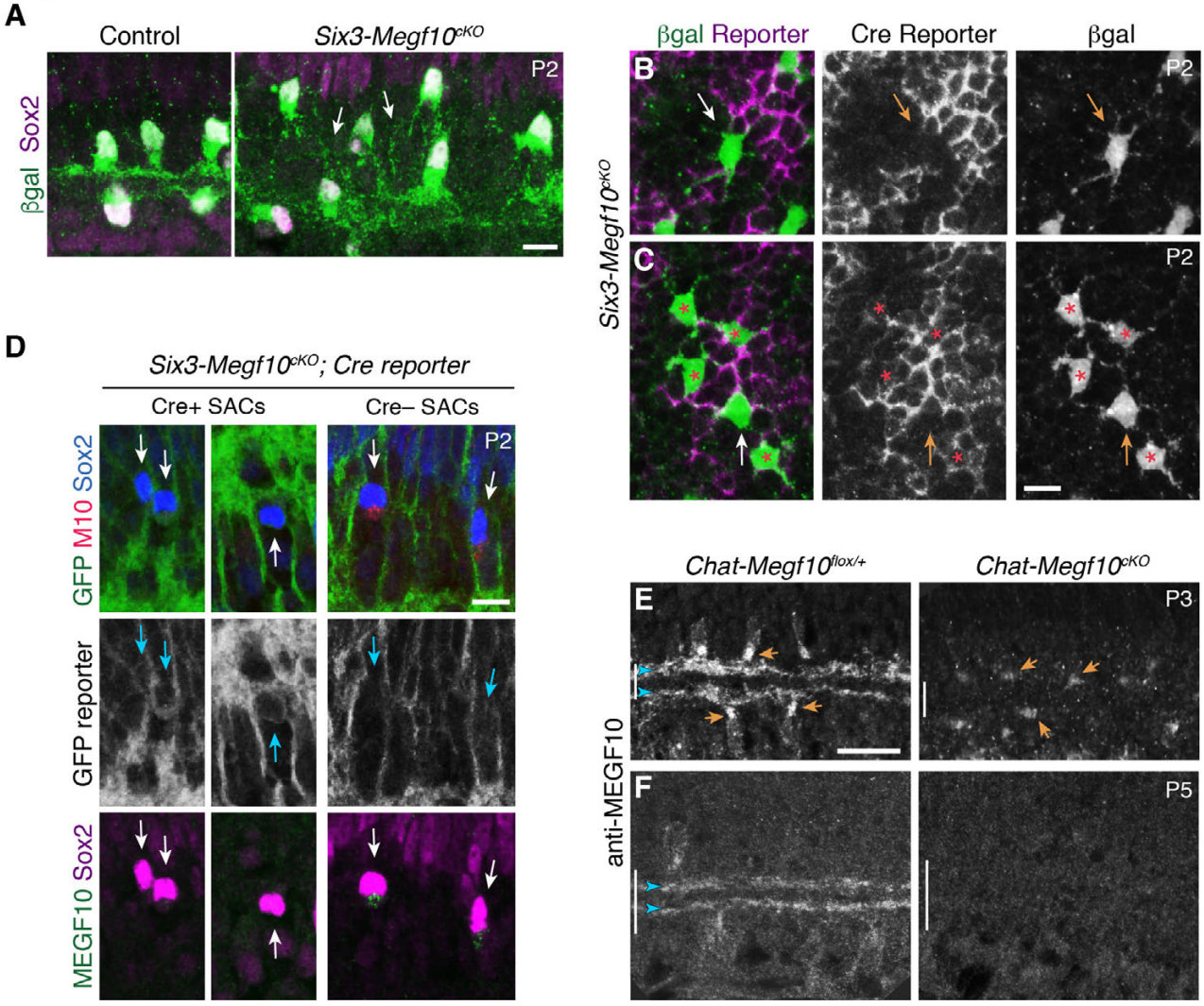

Figure 6-Supplement 1: *Megf10* cell autonomy: Characterization of conditional mutant mice

A: *Six3-Megf10*^{cKO} mice phenocopy SAC sublayer formation errors seen in null mutants. Cross-sections through central retina of P2 *Six3-Megf10*^{cKO} and littermate control mice. Immunostaining for *Megf10*: βgal and Sox2 revealed SAC morphology. Control SACs (left) have formed IPL sublayers by P2 and they rarely project to soma layers. In *Six3-Megf10*^{cKO} mice (right), sublayers are absent and SACs project exuberantly to soma layers (arrows).

B: The same *Six3-Megf10*^{cKO} Cre-negative SAC from Fig. 6B (arrow). βgal and GFP (Cre reporter) channels are shown separately (middle, bottom) to demonstrate lack of GFP expression in this cell.

C: Another example of a Cre reporter-negative *Six3-Megf10*^{cKO} SAC (arrow) surrounded by mutant Cre-positive cells (asterisks). All 5 cells, including the unrecombined one, participate in an aberrant INL dendritic network (bottom).

D: GFP Cre reporter is a reliable proxy for MEGF10 protein expression status in *Six3-Megf10*^{cKO} mice. Cre^{+} SACs (left, center panels) express the GFP reporter and lack MEGF10 immunoreactivity. Cre^{-} SACs lack GFP reporter expression and retain MEGF10 immunoreactivity. Arrows denote position of Sox2^{+} SACs in each panel.

E,F: Timing of MEGF10 protein loss in *Chat-Megf10*^{cKO} mice. At P3 (E), MEGF10 immunoreactivity is much lower in mutants (right) than in littermate controls (left), but most SACs still express some protein (arrows indicate examples of MEGF10-positive cells). At P5 (F), MEGF10 immunoreactivity is virtually absent in mutants but readily detectable in controls. Arrowheads, SAC IPL strata. Vertical bar, IPL.

Scale bars: 10 µm (A-D); 25 µm (E,F). Scale bar in C applies to B, and bar in E applies to F.

Figure 6 - Supplement 2

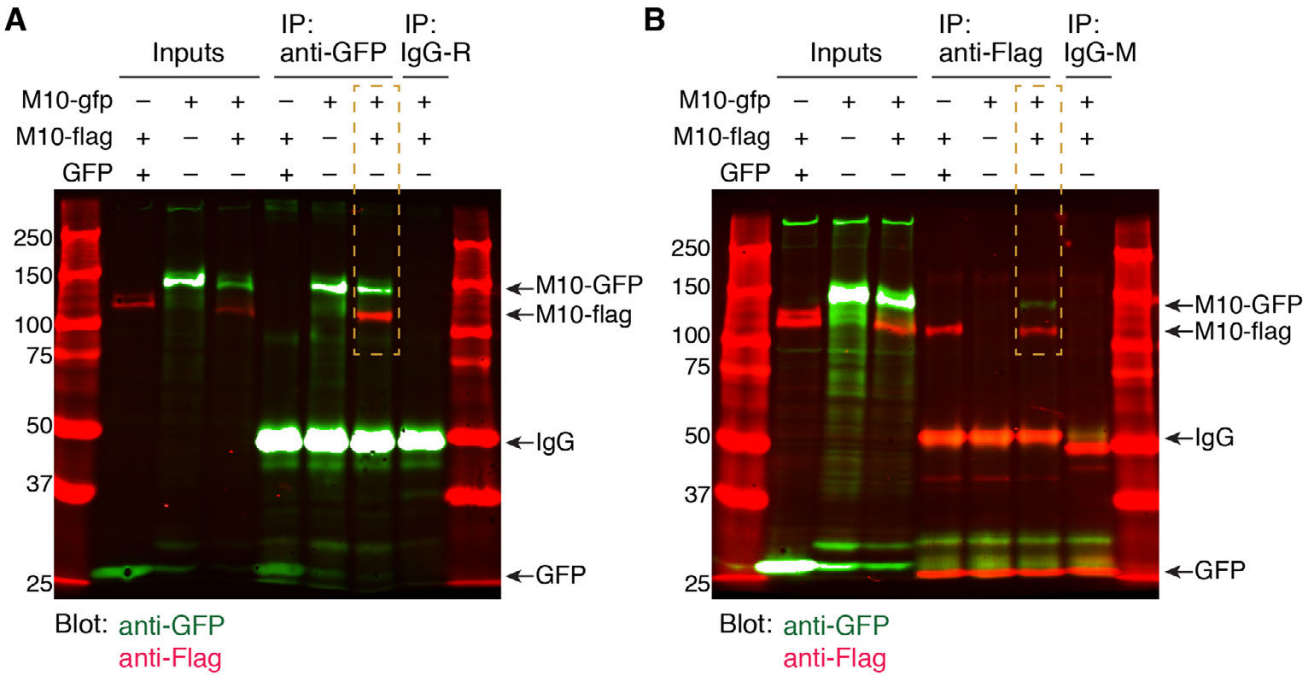

Figure 6-Supplement 2: MEGF10 co-immunoprecipitation experiments

A: Uncropped blot image for co-IP experiment depicted in Fig. 6J. Anti-GFP was used for pull-down. Blot was stained for anti-GFP (green) and anti-Flag (red). Orange box indicates the condition in which cells were transfected with both MEGF10-ΔICD constructs. In this condition, pull-down with anti-GFP precipitated both MEGF10-ΔICD-GFP and MEGF10-ΔICD-Flag constructs, demonstrating that they interact. Ladder markings in kDa. Expected sizes for MEGF10-ΔICD constructs, GFP, and IgG are indicated (arrows). R, rabbit IgG control. See Fig. 6I for illustration of in MEGF10-ΔICD construct design.

B: Independent replicate of MEGF10-ΔICD co-IP experiment, using anti-Flag for pull-down. Labels as in F. IP with anti-Flag co-precipitated both GFP and Flag-tagged MEGF10-ΔICD constructs (orange box). Mouse (M) IgG control did not precipitate MEGF10 constructs, and MEGF10-ΔICD-Flag did not co-precipitate with GFP alone.

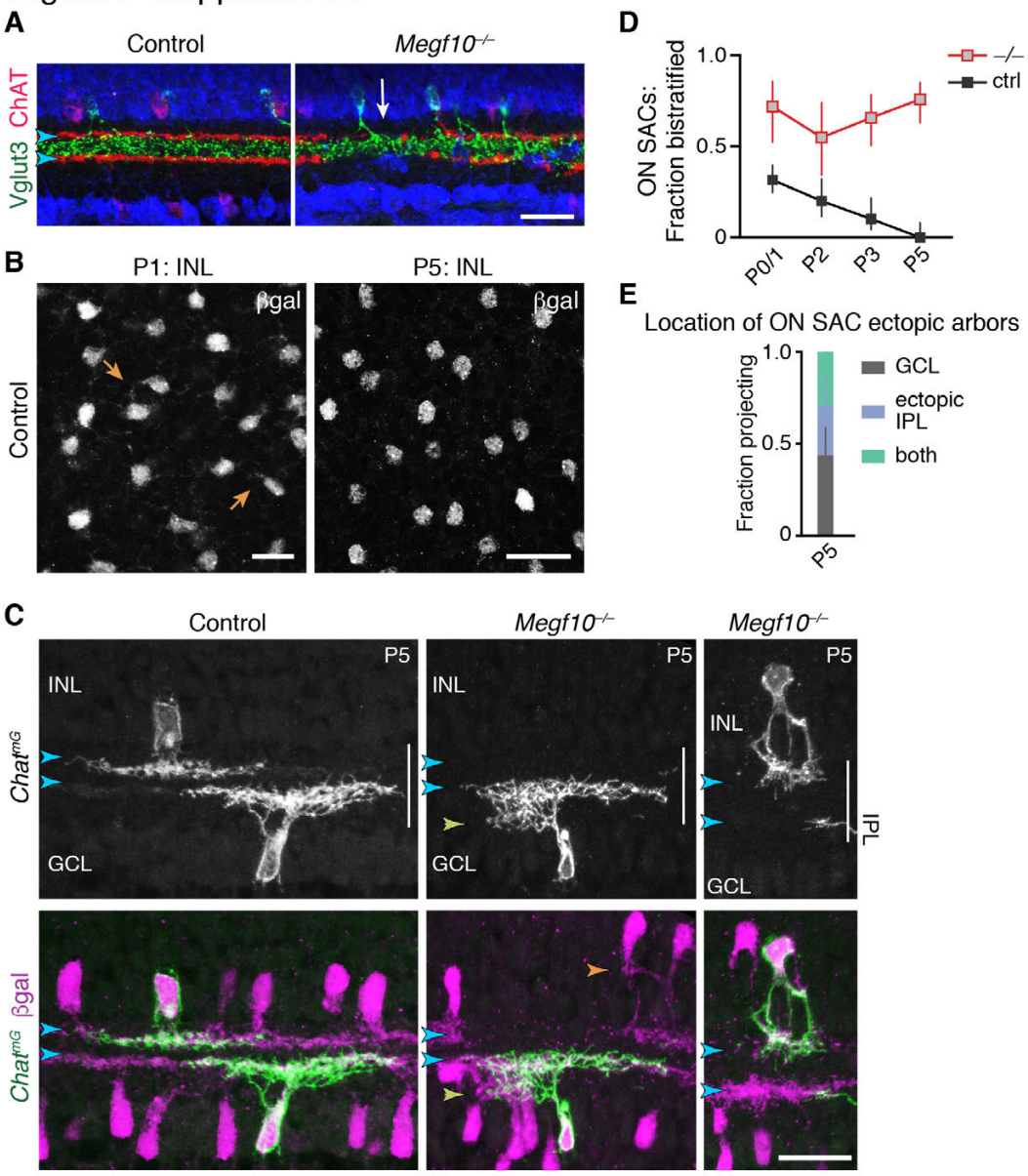

Figure 7-Supplement 1: SAC phenotypes in *Megf10* mutants at P5 and at maturity.

A: Specificity of *Megf10*$^{-/-}$ SAC IPL innervation phenotype. The same cross-sections from Fig. 7A are shown here, overlaid with anti-Vglut3 staining (green) to label amacrine cells that project to an IPL sublayer between the SAC strata (arrowheads). Regions of mutant IPL not innervated by SACs (arrow) are still innervated by Vglut3^{+} amacrine cells, demonstrating that absence of ChAT^{+} arbors is not due to tissue damage and that failure to innervate the IPL is a SAC-specific phenotype.

B: Littermate control images matching the P1 and P5 *en-face* mutant images shown in Fig. 7F. Images were acquired at the INL level, at a z-stack position comparable to the Fig. 7F mutant images. SACs are labeled by *Megf10:*βgal. At P1 (left), control SACs still project arbors within INL (arrows), but their network is not as extensive as in mutants (compare to Fig. 7F, left). At P5 (right), control SACs do not project to INL. By contrast, mutant SAC arbor aggregates are observed in INL (Fig. 7F, right).

C: Additional characterization of *Meg10* mutant phenotype at P5, using *Chat*^{mG} to label single cells and *Megf10:*βgal to label the full SAC population. Control OFF and ON SACs (left panels) are monostratified within the DS circuit IPL sublayers (blue arrowheads). Center: Example of a mutant ON SAC that makes an ectopic projection to inappropriate IPL sublayer (yellow arrowhead) while also projecting to the expected DS circuit sublayer (blue arrowheads). OFF SACs in this same field of view make ectopic projections within the INL (orange arrowhead), illustrating the simultaneous soma-layer and IPL ectopias observed only at P5. Right: Many mutant SACs still show perturbed IPL innervation at P5. Even though this SAC has innervated the IPL, and begun to ramify arbors that stratify in the appropriate sublayer, its arbors are far less extensive than controls

(left), and it covers a smaller IPL territory. Thus, even though SAC sublayers have formed, individual SACs still demonstrate severe errors in IPL innervation that likely lead to persistence of IPL gaps.

D,E: ON SAC ectopic projections transition to the IPL at P5 in *Megf10* mutants, similar to OFF SAC projections (Fig. 7G,H). Frequency of mutant ectopic ON SAC projections does not change over development (D), even though arbor anatomy changes by P5 (C). P0-3 data in D replotted from Fig. 5F, with both control groups combined. E: As with mutant OFF SACs, ON SACs can make ectopic projection errors either within the GCL or the IPL at P5.

Scale bars: 25 µm.

Figure 8 - Supplement 1

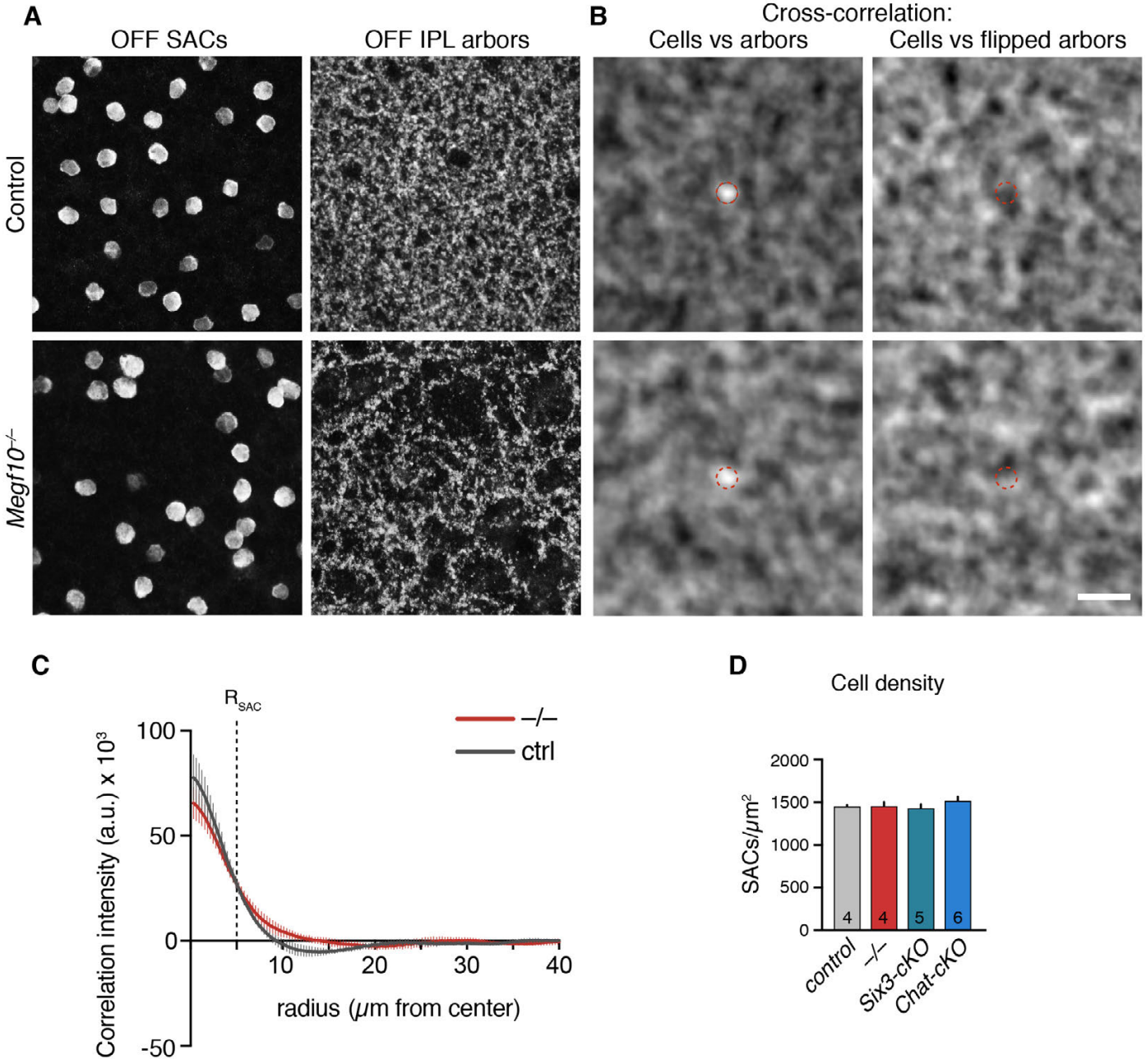

Figure 8-Supplement 1: Correlations between SAC soma and arbor position.

A: E*n-face* views at different levels of individual confocal z-stacks, depicting OFF SAC cell bodies (left) and their underlying arbors in the IPL (right). Images are from adult (P46) ChAT-stained whole-mount retinal preparations. *Megf10* mutants have less orderly soma positions, and less uniform arbor distributions, than controls. Qualitatively, it is possible that gaps in the mutant arbor plexus line up, at least in some cases, with gaps in the soma array.

B: Spatial cross-correlation map generated by correlating soma and arbor images like those in A. Left, soma vs. underlying arbors. Right, soma vs. flipped image of underlying arbors, which controls for correlations in the image data unrelated to soma and arbor position. Bright pixels indicate positive correlations; dark pixels indicate negative correlations. Dashed red line indicates size of average SAC cell body. The bright region at the center of the "cells vs. arbors" map shows that when the two images are perfectly aligned, or offset by about 1

cell radius, correlations are high. Such correlations are absent from the control "flipped arbors" map, indicating that they arise due to the specific locations of somata and arbors.

C: Quantification of soma-arbor cross-correlations, from maps like those shown in B. Correlation intensities were measured radially out from the center. Values obtained from correlating real data were normalized by subtracting the equivalent-radius values from the flipped-arbor images. In control animals (gray), there is a strong positive correlation on a spatial scale approximating the size of a SAC cell body (dashed vertical line). There is also a weaker negative correlation at the 10 - 20 µm spatial scale. Beyond ~25 µm, soma and arbor positions are uncorrelated. In mutants (–/–, red), both correlations are attenuated. This finding suggests that soma-arbor correlations still exist in mutants to some extent; however, there are also additional factors influencing arbor position in mutants that reduce the influence of soma position. Sample size: $n = 9$ sets of soma & arbor images from 2 animals of each genotype (P46 adults). Error bars, S.E.M.

D: SAC cell density did not differ among *Megf10* germline-nulls, conditional-nulls, or littermate controls ($Chat^{Cre}$; $Megf10^{flox/+}$). Therefore cell density differences cannot explain arbor patterning or mosaic spacing phenotypes (e.g. Fig. 8B). $Megf10^{-/-}$ data from Kay et al. (2012). One-way ANOVA, $F(3, 15) = 0.6063$; $p = 0.6210$. Error bars, S.E.M.

Scale bar = 25 µm. Bar applies to both A and B.

Figure 9 - Supplement 1

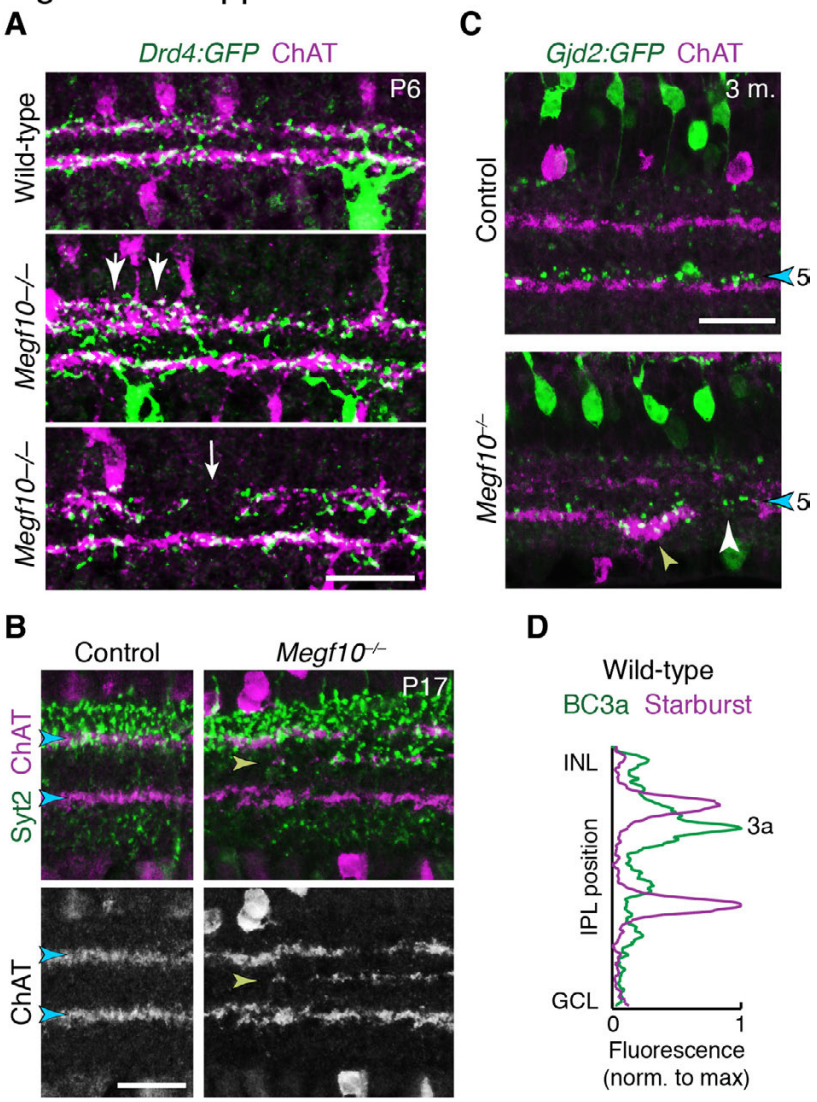

Figure 9-Supplement 1: IPL innervation by DS circuit neurons in *Megf10* mutants.

A: *Drd4:GFP* mouse line was used to label a subset of ooDSGCs that is mutually exclusive with *Hb9:GFP*. IPL laminar targeting by *Drd4:GFP*$^{+}$ ooDSGCs was assessed in cross-sections of *Megf10*$^{-/-}$ and littermate control retinas, co-stained for ChAT to reveal SAC dendrites. In mutants, *Drd4:GFP*$^{+}$ cells made the same laminar targeting errors observed in the *Hb9:GFP* line (Fig. 9A-C): When SACs projected to inappropriate laminar locations, ooDSGC dendrites were recruited to join them (center panel, large arrows). GFP^{+} dendrites also failed to enter IPL regions not innervated by SACs (bottom panel, white arrow).

B: Laminar targeting errors by BC2 bipolar cells in *Megf10* mutants. In control retina, BC2 axon terminals (stained with anti-Syt2, green) fill the entire IPL region between the INL border and the OFF SAC layer. In mutants, OFF SAC misprojection errors typically occur in the region that is normally innervated by BC2 (e.g. Fig. 9A,G), precluding a quantitative analysis of BC2 error rate. However, we did find a small number of cases, such as the one shown here, in which OFF SACs project inappropriately to central IPL regions where BC2 terminals are not normally found (yellow arrowhead). In these cases BC2 arbors are recruited to join SAC arbors in their abnormal laminar location. Thus, BC2 IPL projections are likely guided by similar SAC-derived cues as the other DS circuit-projecting bipolar cell types.

C: *Gjd2:GFP* mouse line was used as an independent marker of BC5 bipolar cells. In cross-sections of adult retinas stained for anti-GFP (green) and anti-ChAT (red), GFP was found to label BC5 neurons arborizing in their characteristic position adjacent to the ON SAC sublayer (blue arrowhead). Thus, unlike the *Kcng4*^{mG} line in which both BC5 and BC7 were labeled, this line could be used to specifically assess BC5 phenotypes. In *Megf10* mutants, an ectopic SAC projection near the GCL border (yellow arrowhead) recruited BC5 terminals to an inappropriate IPL location. BC5 terminals are also seen innervating a gap in the SAC sublayer (white arrowhead). BC5 neurons therefore appear to respond similarly to SAC-derived cues as the other DS-circuit bipolar cell types.

D: Fluorescence intensity plot across IPL obtained from a wild-type image similar to Fig. 9G – i.e. tissue stained with anti-ChAT (purple) and the BC3a marker HCN4 (green). BC3a arbors are excluded from the OFF SAC sublayer and arborize adjacent to it, similar to the behavior of BC5 and BC7 (Fig. 9E).

Scale bars: 25 µm (A,C,D); 50 µm (B).

Figure 10-Supplement 1

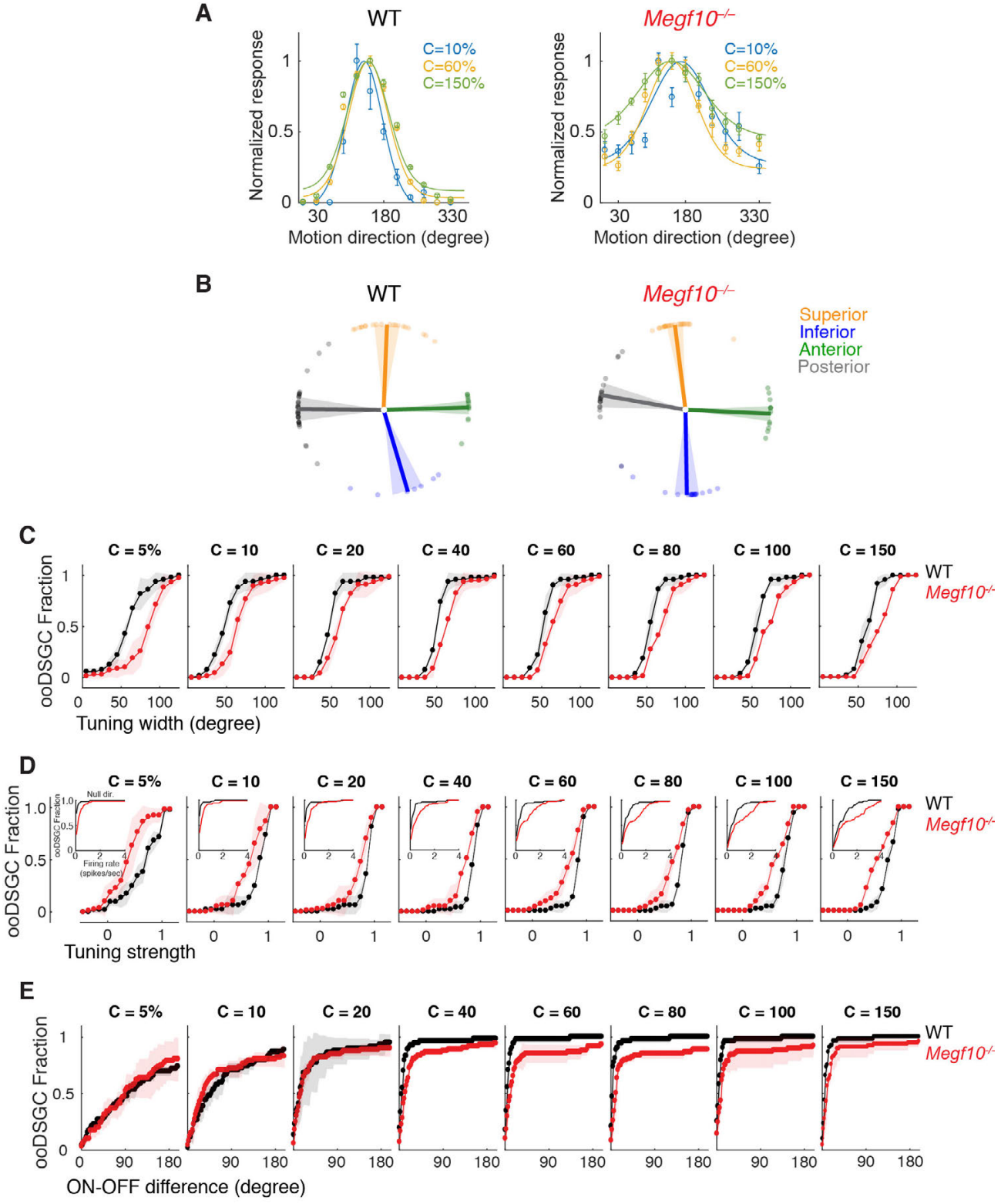

Figure 10-Supplement 1: Contrast-dependence of direction-tuning phenotypes in *Megf10*$^{-/-}$ ooDSGCs.

A: Tuning curves from representative wild-type (WT) and *Megf10* mutant ooDSGCs measured at 3 contrasts (10, 60 & 150% Weber contrast). Circles show responses, solid lines show von Mises fits. Mutant tuning curves are broader than controls at all three contrasts.

B: Preferred directions of WT ooDSGCs (left) align to the four cardinal ocular axes: superior, inferior, anterior and posterior (Oyster and Barlow, 1967). K-means clustering was used to separate the recorded ooDSGC population into these four subtypes (see Methods). Population mean (solid line) and standard deviation (shaded region) of preferred directions for each subtype is plotted; circles denote preferred direction of individual ooDSGCs. Preferred directions of *Megf10*$^{-/-}$ ooDSGCs (right) were also aligned to the cardinal axes, and there was no appreciable change in the fraction of ooDSGCs populating each subtype.

C-E: Cumulative distributions of tuning width (quantified by circular standard deviation; C), tuning strength (D), and ON-OFF preferred direction difference (E), measured at different bar contrasts (identified at the top of each plot) for WT and *Megf10*$^{-/-}$ ooDSGC populations. Insets (D) show responses to null direction stimuli. The analyzed RGC populations were the same as for data shown in Fig. 10 (n = 80 WT and 74 mutant ooDSGCs, two retinas each genotype). The width and speed of the moving bar was 1200 μm and 550 μm/sec, respectively. Error bars/bands, S.E.M.